OPTIMIZATION OF ALD GROWN TITANIA THIN FILMS FOR THE INFILTRATION OF SILICA PHOTONIC CRYSTALS

A Dissertation
Presented to
The Academic Faculty

By

Dawn L. Heineman

In Partial Fulfillment
Of the Requirements for the Degree
Master of Science in Materials Science and Engineering

Georgia Institute of Technology
April 2004

OPTIMIZATION OF ALD GROWN TITANIA THIN FILMS FOR THE INFILTRATION OF SILICA PHOTONIC CRYSTALS

Approved by:

Dr. Christopher Summers, Advisor

Dr. Robert Snyder

Dr. Zhong Lin Wang

April 22, 2004

ACKNOWLEDGEMENTS

I would like to express my thanks to my advisor, Dr. Christopher Summers, for his support throughout my thesis project. I would also like to thank my committee members, Dr. Robert Snyder and Dr. Z. L. Wong, for their participation in my thesis committee. Thanks to the members of the Summers' Photonic Crystals research group, especially Dr. Elton Graugnard and Jeff King. To Elton Graugnard, I greatly appreciated your guidance, patience, and willingness to discuss the direction of my research. Thanks to Jeff King for both the groundwork he has laid in photonic crystal research as well as the time he took to train me in various fabrication and analysis techniques.

I would also like to thank the many people who helped in the acquisition of data presented in this thesis: Ashwini Sinha, of the Chemical Engineering department, for ellipsometer measurements and development of the ellipsometer dispersion model; Kip Findley, Xudong Wang, and Jeff King for SEM images; Evan Law for acquisition of spectral reflectance and XPS data; and Elton Graugnard for AFM images and measurements.

Finally, I would like to thank those family, friends, and teachers who have supported me throughout my academic career. You always believed in me, even when I didn't.

TABLE OF CONTENTS

LIST OF TABLES

LIST OF FIGURES

SUMMARY

The atomic layer deposition (ALD) growth of titania thin films was studied for the infiltration of silica photonic crystals. Titania thin films were grown in a custom-built ALD reactor by the alternating pulsing and purging of $TiCl_4$ and water vapor. The conformal nature of ALD growth makes it an ideal candidate for the infiltration of the complex opal structure.

Titania is a high refractive index material, which makes it a popular material for use in photonic crystal (PC) applications. Photonic crystals are periodic dielectric structures that forbid the propagation of light in a certain wavelength range. This forbidden range is known as the photonic band gap (PBG). A refractive index contrast of at least 2.8 is required for a complete PBG in an inverted opal structure. Therefore, the rutile structure of titania is more desirable for use in PCs due to its higher index of refraction than the anatase or brookite structure.

The growth mechanisms and film properties of the TiO_2 thin films were studied. Investigation of the growth mechanisms revealed saturated growth rate conditions for multiple temperature regions. Film characterization techniques included XRD, SEM/EDS, XPS, AFM, reflectivity, and index of refraction measurements. Post growth heat treatment was performed to study the conversion from the as-deposited crystal structure to the rutile structure.

After optimization of the deposition process, the infiltration of silica opals for PC applications was attempted. The filling fraction was optimized by increasing the pulse and purge lengths at a deposition temperature of 100^{o}C. Although the silica opals were

successfully infiltrated using ALD of TiO_2, the long range order of the PC was destroyed after the heat treatment step required to achieve the high index rutile structure.

CHAPTER 1

INTRODUCTION

Photonic crystals (PCs) have emerged as an area of intense research in the past decade due to their exciting applications in optics. Photonic crystals are periodic dielectric structures that result in a photonic band gap (PBG), which is the optical analogue to the electronic band gap in semiconductors. It is a range of wavelengths that are prohibited from propagating in the crystal as a consequence of the dielectric contrast. The existence and width of the photonic band gap is dependent on the crystal structure, refractive index contrast, and filling fraction of the high index material. The high index material must also be non-absorbing in the wavelength region of interest.

Using numerical methods to solve Maxwell's equations for electromagnetic waves inside a photonic crystal, the allowed photonic energy levels (or frequencies) can be determined as a function of wavenumber (or wavelength). These allowed levels can then be used to construct a band diagram, similar to the electronic band diagram for a semiconductor. These calculations predict that photonic band gaps can exist for a variety of 1-, 2- and 3-dimensional structures. In 3-D, a full (omni-directional) photonic band gap can exist in FCC and diamond based structures. Since the diamond structure has proven difficult to fabricate, most work has focused on the FCC based structures. The inverse FCC structure, which consists of a close packed arrangement of air spheres in a high dielectric material, is predicted to have a full PBG between the 8th and 9th photonic bands for a refractive index contrast greater than 2.8. The main challenge in photonic crystals is to find ways to manufacture the nanosized 3-D crystal structures. For photonic

crystals designed to operate in the visible, the periodicity of the crystal structure must be on the order of that of visible light, which has a wavelength range of 400 to 750 nm. Therefore, photonic crystals need to be made with a repeat distance on the order of 200 to 400 nm, which is at the limit of current microlithography techniques. Three-dimensional PCs with feature sizes applicable in the optical regime have been fabricated using focused ion beam, traditional microlithography, and colloidal self-assembly techniques. These fabrication techniques often result in a structure that does not have sufficient refractive index contrast for the existence of a full PBG; hence they are used as PC templates for the infiltration of a high index material. The template material is then removed, resulting in an inverse PC.

Titania (TiO_2) is one of the few high index materials that has low absorption in the visible regime. The high temperature rutile polymorph of TiO_2 has a refractive index of 3.4-2.81 at wavelengths from 400 to 750 nm. These properties have made titania a popular material for use as the high index material in photonic crystals. Titania is typically infiltrated into PC templates using sol-gel techniques. However, sol-gel infiltration usually results in porous materials with a low filling fraction. The sol-gel reactions result in the deposition of amorphous titania, which requires heat treatment at temperatures of greater than 700^{o}C to transform into the high index rutile structure.

Atomic layer deposition (ALD) is a self-limiting growth technique that can deposit highly conformal films one monolayer at a time. The technique involves the sequential pulsing and purging of reactant gases. The precursors typically used for the deposition of titania are $TiCl_4$ and H_2O. ALD is an attractive option for the infiltration of PC templates because it offers monolayer control of the deposition of conformal films.

The direct deposition of rutile films at temperatures as low as 400°C is another benefit of the ALD TiO_2 process, thus eliminating the need for high temperature heat treatment.

In this thesis we studied the conditions needed for direct ALD deposition of rutile TiO_2 films as well as the transformation of amorphous and anatase phase films to the rutile phase through heat treatment. Planar thin films grown using a custom built ALD system were characterized in order to understand the growth mechanisms of the ALD system at various deposition temperatures. The crystal structure, composition, roughness, and optical properties of the ALD films were characterized. Once the deposition conditions had been optimized, the ALD system was used to infiltrate titania into SiO_2 opal films.

Chapter 2 reviews the literature on topics of; requirements for the existence of a full photonic band gap, photonic crystal fabrication, properties of titania, and atomic layer deposition. The control of titania properties through thermal treatment is also reviewed.

Chapter 3 discusses the details of the inverse opal synthesis procedure. The chapter starts with a description of the confinement cell method for fabricating SiO_2 opals. Then, the details of the ALD system used to infiltrate the opals are described. Finally, the parameters used to grow the ALD films and the characterization methods used to analyze the films and opals are described.

Chapter 4 discusses the results from the three topics investigated in this thesis. First, the characterization of the ALD deposition of titania thin films is discussed. Data on the growth rate, optical properties, crystal structure, and material composition of the ALD films are presented and analyzed. Second, the effect of thermal treatment on ALD

TiO_2 films is discussed. Changes in crystal structure, optical properties, and material composition are reviewed. Finally, the infiltration of SiO_2 opals with rutile ALD TiO_2 films is investigated. The conditions necessary for full infiltration and conformal growth are presented and discussed. Data is also presented on the change in reflectivity in the opal before and after infiltration.

Chapters 5 and 6 conclude the thesis with recommendations for future work that can be done with photonic crystals.

CHAPTER 2

BACKGROUND AND LITERATURE REVIEW

2.1 Photonic Crystals

2.1.1 Introduction to Photonic Crystals

As discussed briefly in the introduction, photonic crystals (PCs) are periodic dielectric structures that may have a photonic band gap (PBG) that forbids propagation of certain frequencies of electromagnetic (EM) waves. Although the name “photonic crystal” is used to describe any periodic structure resulting in a band gap where the EM energy cannot propagate, the nomenclature arises from the original proposal of PC structures for applications in the control of visible light waves.[1] The term "photonic band gap” arises from the analogy between photonic crystals and semiconductors, whereby the PBG is the optical analogue of the electron energy band gap in semiconductors. Just as the arrangement of atoms in a semiconductor acts as a periodic potential to electrons, the periodic dielectric in PCs acts as a periodic potential for incident electromagnetic waves. The PBG arises as a consequence of the refractive index contrast between the two dielectric materials. Light incident on the material will refract and/or reflect off of the dielectric surfaces resulting in the combination or cancellation of certain wavelengths of light. Perfect cancellation of the light waves results in the PBG. However, whereas the periodic arrangement of electrons is determined by nature, the periodic structure in PCs is up to the imagination and fabrication ability of researchers. In a semiconductor the

motion of electrons is described by Schrödinger's equation, and analogously the interaction of light is described by Maxwell's equations.[2]

PCs can be periodic in one, two, or three dimensions. In other words, the periodic modulation of the electromagnetic waves can be in one, two, or three dimensions. An example of a 1-D PC is the Bragg stack, which consists of alternating layers of high and low dielectric material in one direction as shown in Figure 2.1a. Two-dimensional photonic crystals, such as the structure shown in Figure 2.1b, consist of an ordered arrangement of dielectric rods. The inverse structure, where holes are drilled in a dielectric slab, is also considered a 2-D photonic crystal. Figure 2.1c shows an example of a 3-D PC. This is a structure composed of close-packed dielectric spheres. The dielectric contrast arises between the spheres and the air that fills the interstices of the close-packed structure. The inverse structure of air spheres in a high dielectric material is the focus in this thesis.

The photonic band gap is described as a "full" or "complete" band gap when the propagation of light is inhibited in all directions. A PBG that prohibits the propagation of light in only some directions is referred to as an "incomplete" or "-pseudo" photonic band gap. The naturally occurring gemstone opal, which consists of a close-packed arrangement of sub-micron sized silica spheres, as shown in Figure 2.1c, has a pseudo PBG. While the band gap is not complete, it does produce iridescent colors.

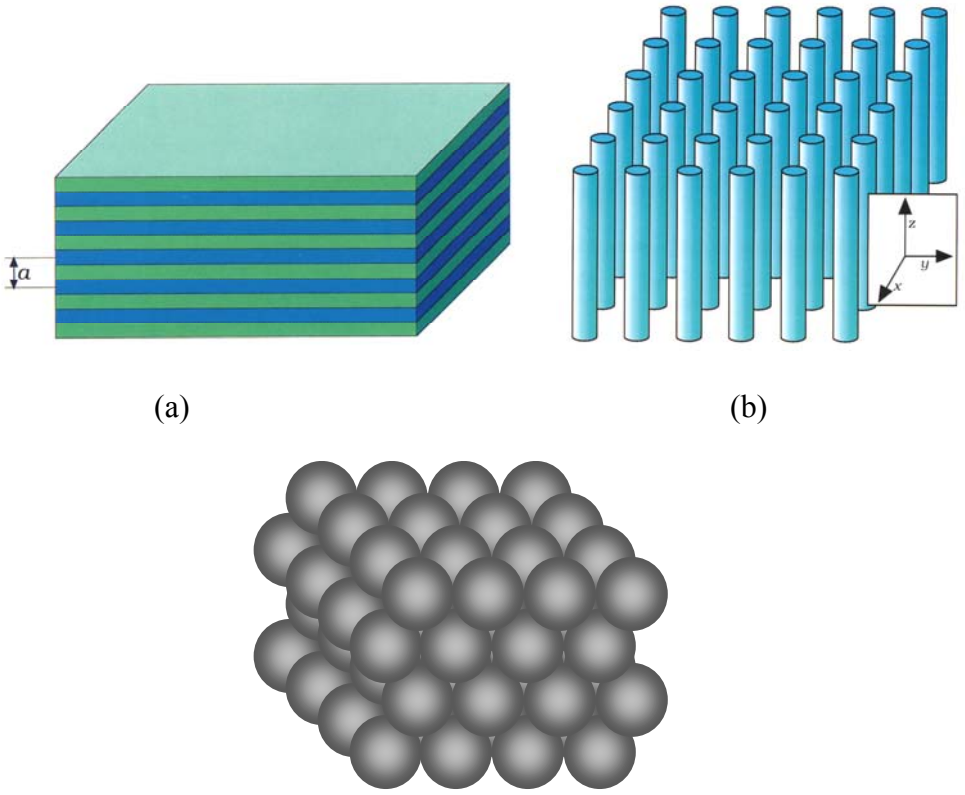

(a) (b)

(c)

Figure 2.1. Examples of (a) one-, (b) two-, and (c) three-dimensional photonic crystals.[1]

The semiconductor analogy also applies to the introduction of defects into the PC structure. The presence of defects results in the creation of allowed states within the band gap. Introducing dielectric defects in the photonic crystal structure can result in many exciting applications such as optical microcavities resulting from point defects and 2D waveguides associated with the introduction of line defects.[2]

Photonic crystals began as a theoretical proposal in order to realize specific applications. Two independent papers from Eli Yablonovitch and Sajeev John proposed exciting applications of the photonic crystal without realizing the challenge of determining a crystal structure and fabricating these crystal structures with sub-

micrometer scale spacing. For Yablonovitch, working with Bell Labs, the motivation was to find a way to inhibit spontaneous emission in order to increase lasing efficiency,[3] whereas John was researching light localization.[4]

Other proposed applications of PCs include zero-threshold semiconductor lasers, single-mode light-emitting diodes, resonant cavity enhanced detectors, highly directional resonant antennas, planar waveguides, filters, and optical limiters.[5] Most of the exciting applications of PCs require crystal structures that can interact with electromagnetic waves in the near infrared or visible light wavelengths. Therefore, dielectric periodicity must be on the same scale as the wavelength of light or the electromagnetic waves to be controlled. Visible light has a wavelength range of 400 to 700 nm. The required dielectric periodicity is approximately equal to $\lambda/2n$, which corresponds to periodicities of 100 to 200 nm. The small feature sizes required for PCs operating in the visible regime presents a challenge because they are approaching the limits of current microelectronic fabrication techniques.

2.1.2 Structural and Material Requirements for a PBG

The existence and width of a full photonic band gap depends on many variables including: crystal structure, the dielectric (or refractive index) contrast between the two materials, electronic energy gap and absorption edge of the high index material, and volume fraction of the high index material. The dielectric contrast required for a PBG depends on the crystal structure of the PC, but is typically at least 2. In order to minimize absorptive losses, the fundamental absorption edge of the high index material should occur at a wavelength below that of the PBG, which is <400 nm for visible light. Given

that the absorption edge is determined by the electronic energy gap of the material,[6] the band gap of the material should be greater than 3.1 eV.

The existence of a photonic band gap can be predicted for a given crystal structure using Maxwell's equations for a periodic dielectric structure.[7] These are written as follows:

$$\nabla \times \mathrm{E} = i\left(\frac{\omega}{c}\right)\mathrm{H}, \quad \nabla \times \mathrm{H} = -i\left(\frac{\omega}{c}\right)\varepsilon(r)\mathrm{E} \tag{2.1}$$

where E and H are the electric and magnetic fields, respectively, ω is the angular frequency of the incident electromagnetic wave, c is the speed of light, and ε(r) is the position dependent dielectric constant of the PC. Equation 2.1 can be further simplified to:

$$\nabla \times \left(\frac{1}{\varepsilon(r)}\nabla \times \mathrm{H}(r)\right) = \left(\frac{\omega}{c}\right)^2 \mathrm{H}(r) \tag{2.2}$$

Solving Equation 2.2 numerically for EM waves inside a photonic crystal determines the allowed photonic bands. The allowed frequencies are directionally dependent and can be used to construct a band diagram, as shown in Figure 2.2 for a FCC structure. Along the y-axis is plotted the normalized frequency, while wavevector, or direction, is plotted on the x-axis.

Initially it was thought that the FCC structure would have a full PBG (FPBG). The FCC structure has the roundest structure in reciprocal space, thereby reducing the chance of overlap of a forbidden gap. Yablonovitch and Gmitter reported a full photonic band gap for an experimental crystal consisting of air spheres in a dielectric material with

a refractive index of 3.5.[8] The crystal had a filling fraction of 14% dielectric material and 86% air spheres, which is greater than the close-packed filling fraction of 74%. Therefore, the air spheres in the crystal were overlapping. However, the calculations of Ho *et al.* showed that an FCC lattice with either dielectric or air spheres will only have a pseudogap as shown in Figure 2.2.[7] This pseudogap is due to a symmetry induced degeneracy at the W point in the first Brillouin zone (BZ) as shown in Figure 2.3. The degeneracy between the second and third bands was independent of the refractive index contrasts and filling ratio of the spheres. The second and third photonic bands also cross at the U point of the FCC BZ.

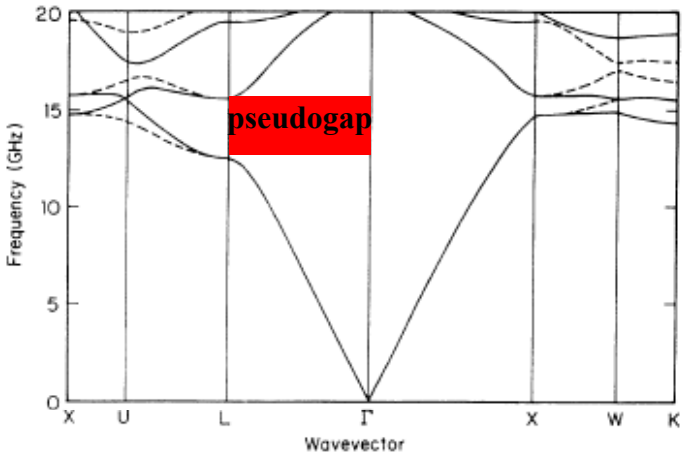

Figure 2.2. Calculated photonic band structure for a FCC dielectric structure composed of air spheres in a dielectric background of refractive index 3.5. The filling ratio is 86% air and 14% dielectric material.[7]

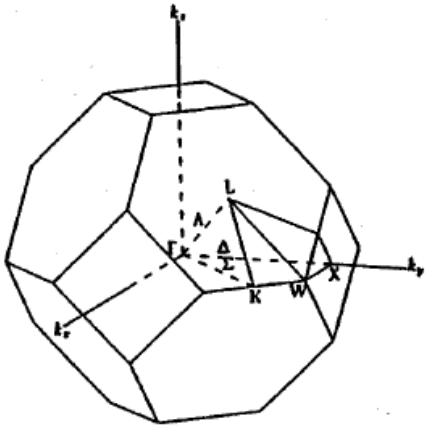

Figure 2.3. First Brillouin zone of the FCC crystal structure.

The degeneracy at the W point can be avoided by using a nonspherical basis for the formation of the FCC lattice. The diamond lattice retains the FCC BZ while changing the symmetry of the lattice. Research has also been done to find ways to make a PC using peanut shaped and other non-spherical particles as the basis in a FCC lattice in order to avoid the symmetry induced degeneracy in the PBG.

The diamond cubic lattice introduced by Ho *et al.* was the first structure theoretically predicted to have a full PBG.[7] A diamond cubic lattice with a refractive index contrast of 3.6 and a dielectric filling ratio of 34% has a full photonic band gap between the second and third bands as shown in Figure 2.4. The gap to midgap ratio was calculated for a refractive index contrast of 3.6. The maximum gap to midgap ratio, 15.7%, for dielectric spheres in a diamond lattice occurred at a filling ratio of 37%. Air spheres with a filling ratio of 81% resulted in a larger maximum gap to midgap ratio of 28.8%. Theoretical calculations for structures with a filling fraction of 34% dielectric spheres in air and 81% air spheres in dielectric predict that the diamond structure exhibits a PBG for refractive index contrasts greater than 2. While the diamond structure is

exciting because it has a FPBG at relatively small refractive index contrast, it is very difficult to fabricate at the sub-micron scale.

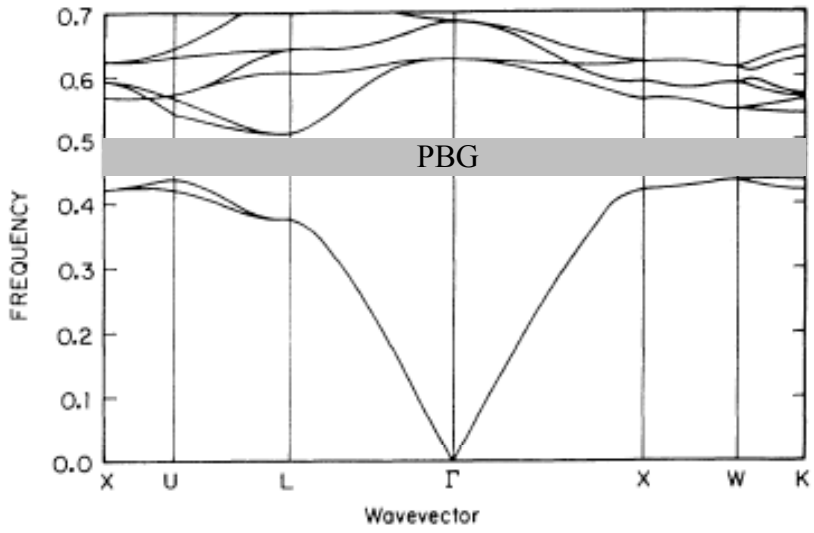

Figure 2.4. Calculated photonic band structure for a diamond dielectric structure consisting of dielectric spheres of refractive index 3.6 in an air background. The filling ratio of the dielectric material is 34%. The frequency is given in units of *c/a*, where *a* is the cubic lattice constant of the diamond lattice.[7]

As mentioned earlier, the inverse FCC structure, which consists of FCC packed air spheres in a high index matrix, has a pseudogap between the second and third photonic bands. Ho *et al.* only examined the first couple of bands in the structure and therefore missed the existence of a full PBG between higher energy photon bands. Sozuer *et al.* showed that the inverse FCC structure has a full PBG between the eighth and ninth bands, in addition to pseudogaps between the 2nd and 3rd bands and the 5th and 6th bands.[9] The FPBG between the 8th and 9th bands opens up for crystals with a refractive index contrast of greater than 2.8. The photonic band structure for an inverse FCC arrangement of air spheres in silicon is shown in Figure 2.5.[10]

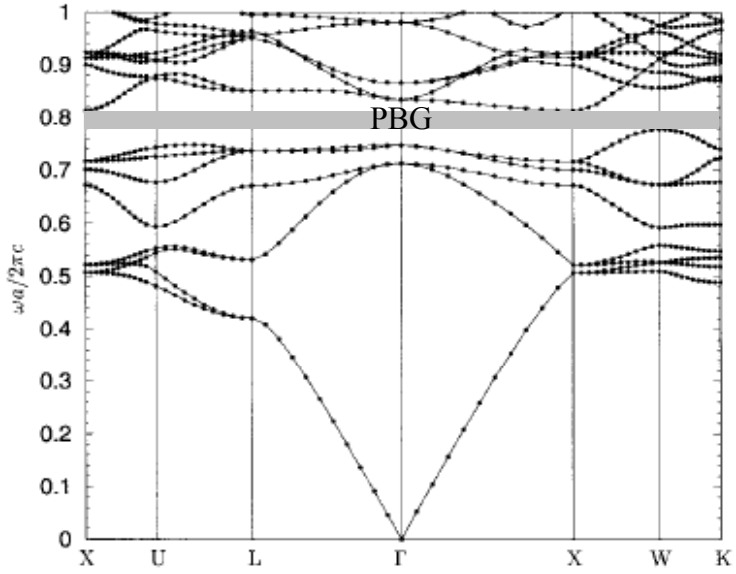

Figure 2.5. Calculated photonic band structure for a close-packed FCC lattice of air spheres in silicon ($\varepsilon \approx 11.9$).[10]

Since the refractive index of air is approximately 1.0, a material with an index of greater than 2.8 is needed in order to fabricate an inverse FCC photonic crystal with a complete PBG. For our study, this material must also be transparent in the visible part of the light spectrum. Some possible materials that meet these requirements are listed in Table 2.1 along with the relevant optical properties of the materials.

Table 2.1. Optical properties of some high index materials.[6,11,12,13,14]

Material	Index of Refraction	Transparency Range (nm)	Energy Gap (eV)
CdS	2.48 (@630nm)	500 -	2.5
Diamond (C)	2.42	250 - 80,000	5.1
Fe_2O_3	3.22, 2.94		
GaAs	3.34 (@780nm)	1000 - 20,000	1.42
GaP	3.42 (@550nm)	550 -	2.24
Si	3.42	1200 - 15,000	1.13
SiO_2	1.56	200 - 3000	
SnO_2	1.8 - 2.0	326 -	3.35 - 4.3
SnS_2	3.2 (@700nm)		2.4
TiO_2 (anatase)	o=2.59, e=2.52 (@546nm)	450 - 5000	3.2
TiO_2 (rutile)	2.92 (@488nm), 2.73 (@633nm)	450 - 5000	3.1
ZnO	2.05	370 -	3.4
ZnS	2.43 (@488nm), 2.35 (@633 nm)	400 - 14,000	3.76

Titania is one of the few materials that meet both the high index and transparency requirements needed for the realization of a full PBG. Titania has many polymorphs, the most common of which are brookite, anatase, and rutile. Brookite has an orthorhombic structure, whereas the anatase and rutile crystal structures are tetragonal as shown in Table 2.2. The temperatures of phase origination as well as the optical constants of the phases are highly dependent on the deposition process used.[15] Although brookite is one of the common low-pressure polymorphs of titania, it has not been observed in the thin film deposition of TiO_2 films. Hence the brookite structure has not been included in

Table 2.2, which contains a list of the physical and optical properties of the most common titania polymorphs.

Table 2.2. Crystal structures of titania.[16]

Polymorph	**Anatase[17]**		**Rutile[18]**	
Structure	Tetragonal		Tetragonal	
Space Group	I 4(1)/amd		P 4(2)/mnm	
Lattice Constants (Å)	A=3.7845		A=4.5937	
	C=9.5143		C=2.9587	
Atomic Positions	Ti	(0, 0, 0)	Ti	(0, 0, 0)
	O	(0, 0, 0.2081)	O	(0.3048, 0.3048, 0)
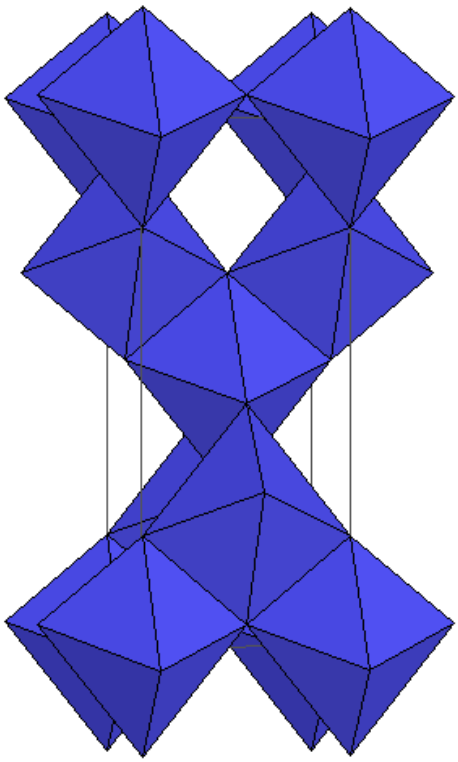			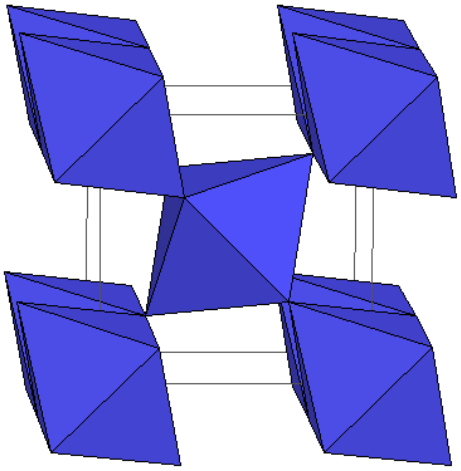	
Density (gm/cm^3)	3.89		4.25	
n (λ=633nm)	2.5		2.73	

Brookite and anatase are metastable phases below 800°C. Rutile is the thermodynamically stable phase at all temperatures[19] and is the most desirable for PC synthesis due to its higher index of refraction and birefringent properties. The refractive index of rutile versus wavelength is plotted in Figure 2.6. The promise of titania as a useful PC high dielectric material is obvious by the number of groups using it to infiltrate photonic crystal templates.[37-43]

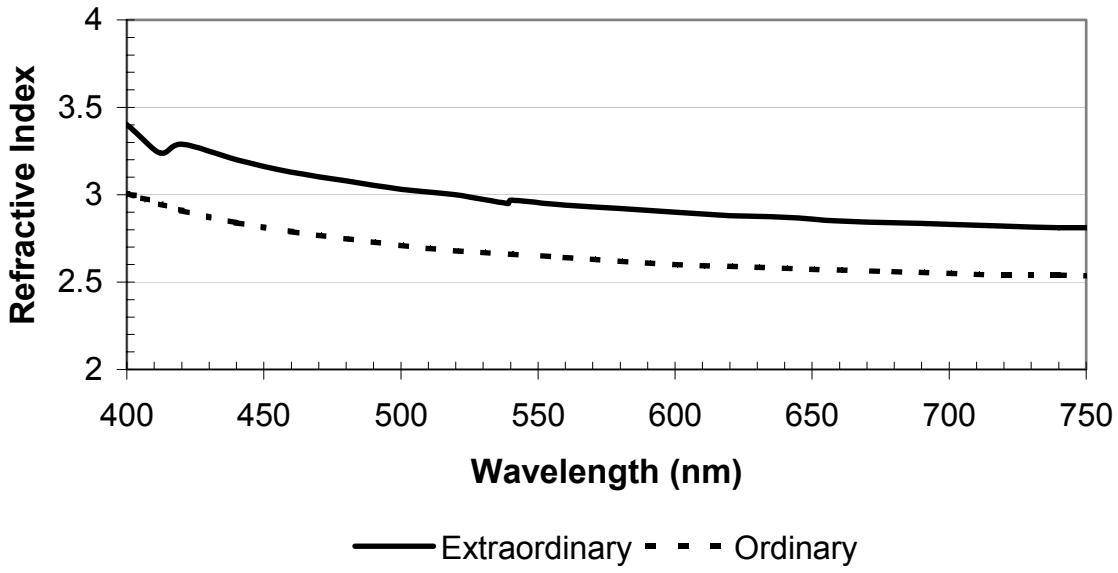

Figure 2.6. Refractive index versus wavelength for a rutile single crystal of titania.[14]

While it was initially a challenge, the theoretical determination of crystal structures having a PBG has been significantly easier than the fabrication of these structures. Whereas FCC structures are relatively easy to fabricate, the difficulty lies in finding a high index material that can be infiltrated into the FCC structure while still retaining the optical properties of the bulk material.

2.1.3 PC Fabrication Techniques

The synthesis of three-dimensional photonic crystals on the nanometer scale has been the subject of considerable research in the past decade. 3-D PCs with a full PBG have been fabricated for operation in the microwave and near-IR regimes, however a complete photonic band gap in the visible light regime has not yet been demonstrated.

The first full band gap PC was fabricated by Eli Yablonovitch in 1991. The structure, named Yablonovite, was fabricated by mechanical machining of a dielectric material.[2] Three intersecting arrays of holes were drilled at an angle of 35.26^{o} from the vertical into the top of a dielectric material in order to create a FCC structure with a non-spherical lattice basis.[20] A schematic of Yablonovitch's fabrication method as well as a picture of Yablonovite is shown in Figure 2.7. However, this PC operated at microwave wavelengths, which are substantially longer than the wavelength of visible light.

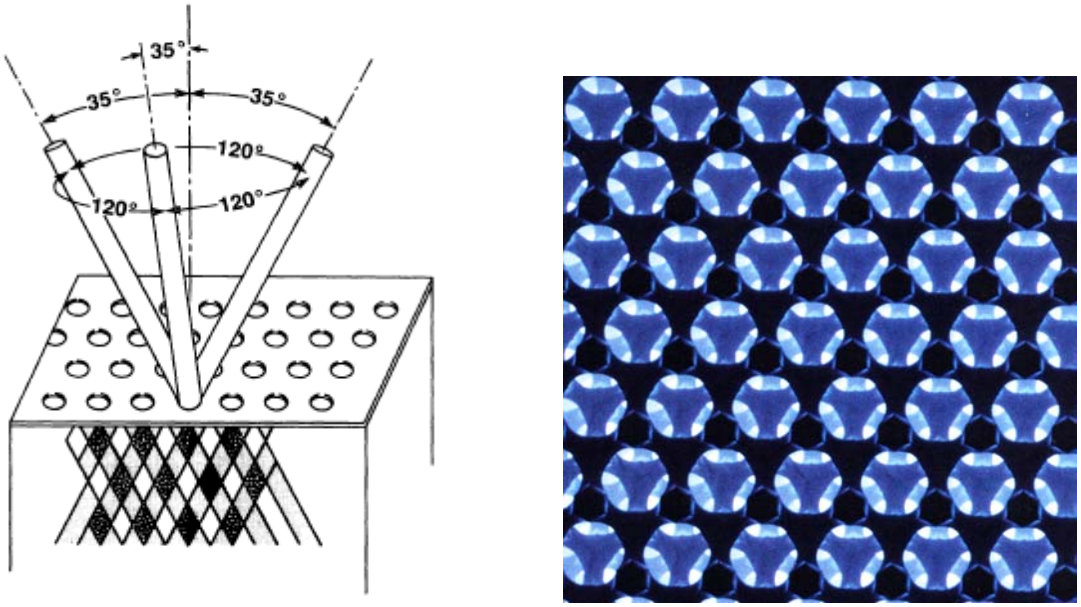

(a) (b)

Figure 2.7. (a) Schematic of fabrication of Yablonovite.[20] (b) Picture of Yablonovite.[21]

Yablonovitch proposed that the same method of drilling holes could be done at smaller scales by using reactive ion etching to "drill" the holes, instead of an actual drill bit. Groups have created Yablonovite-like structures using focused ion beam techniques, [22-23] x-ray lithography, [24-25] and holographic lithography[26] to "drill" the sub-micron sized holes. Structures have been successfully fabricated in the near-infrared (NIR) regime, however they contained only a pseudo PBG due to insufficient filling factor[22] or low refractive index contrast.[25] Another limitation of the Yablonovite "drilling" methods is the fabrication of only a few layers of the periodic structure, with the exception of holographic lithography which has produced as many as 80 close-packed layers. Lithography based structures result in insufficient dielectric contrast for a PBG because the resist typically has a refractive index of approximately 1.5-1.6. However, they might prove useful as templates for infiltration of a higher index material. While the Yablonovite method of "drilling" holes appeared promising, no one has been able to extend this method to the sub-micron sizes required for a PBG in the visible regime.

Other than Yablonovite-like structures, research has focused on two primary techniques for making PCs. Photonic crystals have been fabricated in a layer-by-layer stacking process[27,28,29,30] as initially demonstrated by a group at Iowa State. The layered structure was originally made by the stacking of micromachined silicon wafers,[27] but has since been made with more traditional lithography techniques.[28-29] Fan *et al.* introduced a variation of the layer-by-layer structure in 1994, however the structure was never experimentally demonstrated due to the complexity of the process.[30] Colloidal self-assembly using a confinement cell[31-32] has also been used to fabricate PCs similar in

structure to the FCC structure of the gemstone opal found in nature. The resulting crystal is often referred to as an opal because of this resemblance in structure.

The layer-by-layer stacking process demonstrated by a group at Iowa State has been used to fabricate diamond structures using standard microelectronic techniques. The structure consists of one-dimensional rods with a stacking sequence that repeats every four layers as shown in Figure 2.8. This structure is also referred to as the woodpile structure.[33] While this process is desirable because it uses current microelectronic techniques, research groups have only been able to fabricate a few layers of this structure. Lin *et al.* constructed a five-layer, 180 line width structure operating in NIR regime. In this case, the PBG occurred at 1.6 μm.[29]

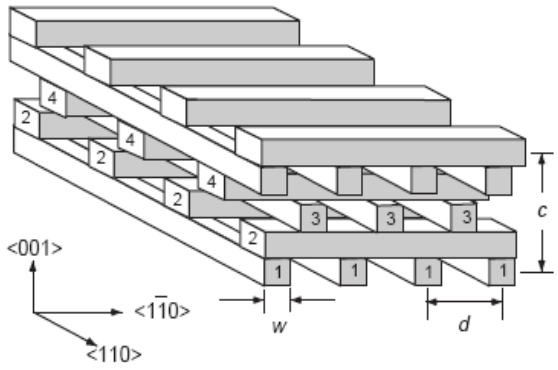

Figure 2.8. Schematic of the layer-by-layer or woodpile structure.[28]

The confinement cell process, first introduced by Park *et al.*, has proven to be a reliable route for making opal structures.[31-32] This process subjects monodispersed colloidal spheres to physical confinement as seen in Figure 2.9. The spheres were confined in a photoresist cell that was sandwiched between two glass substrates. The gasket had shallow trenches cut into one edge that could retain the spheres while allowing

the solvent to flow through. When under continuous sonication the colloidal spheres would form the cubic close packed structure with a packing density of ~74%. The resultant close-packed structure has the (111) face of the opal parallel to the substrate. The confinement cell method was successfully used to fabricate opals for colloidal spheres with a diameter from 50 nm to 1 μm regardless of the chemical composition and surface properties of the spheres. Polystyrene (PS), PMMA, and silica (SiO_2) spheres were used to demonstrate the effectiveness of the process. The ease of fabrication makes the confinement cell technique an attractive option for PC growth. However, the process is limited to FCC and hexagonal structures only. While the refractive index contrast is not enough to achieve a photonic band gap, stop bands occur depending on the sphere size and refractive index.

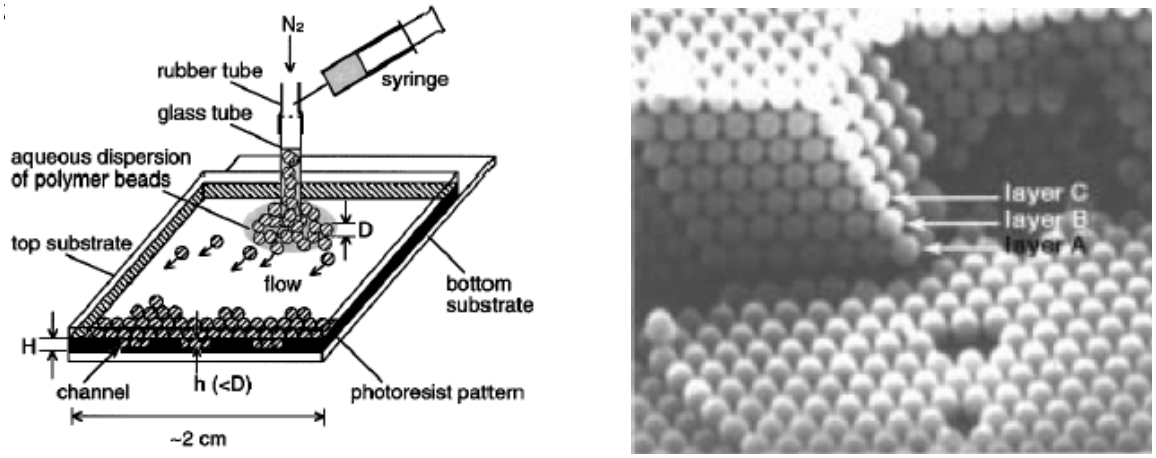

Figure 2.9. (a) Schematic outline of confinement cell method used to assemble colloidal spheres into 3-D crystalline lattices.[32] (b) Cross-sectional SEM micrograph of crystalline assembly of 480 nm polystyrene spheres.[31]

2.1.4 Template Assisted Fabrication of Inverse Structures

Recall that Maxwell's equations predict only a pseudogap in the FCC structure. The diamond or inverse FCC structure is required in order to have a full PBG. As mentioned earlier, the width of the PBG is typically larger for inverse structures that consist of a small percentage of high index material predominantly filled with air. These types of structures can easily be fabricated by infiltration of a PC template with a high index material, followed by subsequent removal of the PC template. Yablonovite,[26] woodpile[34], and opal structures[35,36,37,38,39,40,41,42,43] have all been used as templates for growth of high index photonic crystals. Opal templates consisting of silica,[35-36] polystyrene,[37-42] and PMMA[43] spheres are the most common of those used for the fabrication of inverse FCC structures. Metals,[34] semiconductors,[35-36] and insulators[26,37-43] have been used to infiltrate the various PC templates in order to fabricate an inverse structure.

Several techniques have been used to infiltrate the FCC structure of the synthetic opal with high index material in order to make the inverse FCC structure. These include photochemical deposition, sol-gel processes such as precipitation from liquid-phase chemical reactions,[37-43] chemical vapor deposition (CVD),[35-36] and atomic layer deposition.[44] Many deposition techniques result in films with an index much lower than the index of the bulk structure. Most techniques used thus far have resulted in very porous films, which results in a low filling fraction of the high index material. ALD is an attractive option for opal infiltration because of the self-limited growth and extremely conformal films possible with the technique.

Wijnhoven[37,39] and Vos[38] have fabricated shell structures consisting of titania coated polystyrene spheres with diameters between 120 and 1000 nm. Monodisperse PS spheres in a dispersed colloidal solution were used to form a colloidal crystal through sedimentation. The opal template was created by slow evaporation of the liquid suspension. The template was then infiltrated by precipitation of titania from a reaction of tetrapropoxy-titane (TPT) in ethanol and water vapor in the air. The penetration and reaction cycle was repeated up to eight times to ensure complete filling of the air voids in the opal. Calcination at 450^{o}C resulted in removal of the PS spheres as well as conversion of the amorphous TiO_2 into the anatase phase. The resulting structure was an ordered hexagonal pattern of close packed air spheres connected by windows or channels of titania as shown in Figure 2.10. Considerable shrinkage of ~33% occurred during the calcination step resulting in a low filling fraction of titania. Shrinkage can be prevented if the infiltrated material already has its final form before the calcination step.[39]

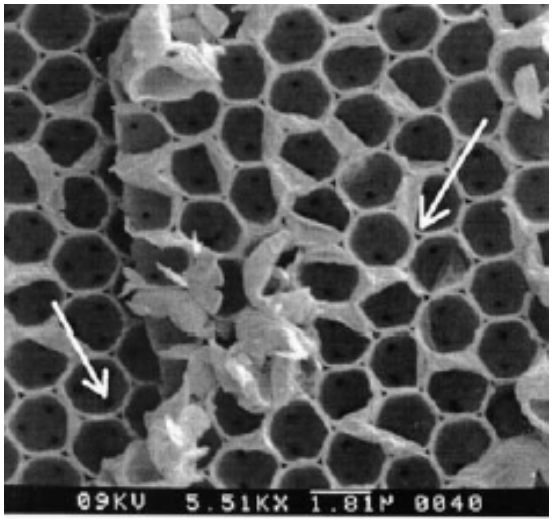

Figure 2.10. Details of a titania inverse opal with sphere radii of 987 ± 20 nm. The left arrow points to one of the holes that connect the air spheres. Small openings are apparent in the TiO_2 structure (right arrow).[37]

Later studies with sphere sizes between 830 and 860 nm revealed that the titania volume fraction varied from 6% to 12% as calculated by x-ray absorption. The dielectric constant of the anatase TiO_2 was estimated from the sphere size and filling fraction using a modification of Bragg's law. The calculation yielded a dielectric constant of 6.25 at a frequency of 8700 cm^{-1}, which is equivalent to that of bulk anatase.[38]

Inverse titania opals fabricated by other groups using techniques akin to Vos and Wijnhoven have yielded similar results.[40] However, Dong *et al.* reported the observation of a new type of inverse structure when using the precipitation technique to grow inverse titania opals.[41-42] The new structure, named the skeleton structure, was observed deep inside the opal grains, whereas the previously reported shell structure was observed at the surface of the opal samples. The structure consisted of titania cylinders connecting the tetrahedral and octahedral voids between the template spheres as shown in Figure 2.11.

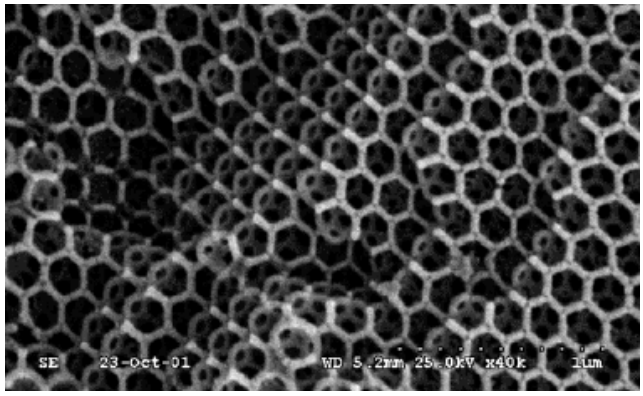

Figure 2.11. SEM micrograph of the skeleton structure observed at the inner part of the sample.[41]

A schematic of the skeleton structure and the accompanying band gap diagram is shown in Figure 2.12. The pseudo gap between the 5^{th} and 6^{th} photon bands in the

inverse FCC structure becomes a complete PBG in the skeleton structure. The skeleton structure also exhibits a full PBG between the 8th and 9th photon bands. The filling ratio of high index material required for the appearance of the 5-6 gap is 9.4% to 40.2% and for the 8-9 gap is 22.7% to 42.4%. The minimum refractive index contrast required for the 5-6 gap and the 8-9 gap is 2.9 and 3.1, respectively. Therefore, only pseudo band gaps were observed in the titania skeleton structure due to the low refractive index contrast of less than 2.5.

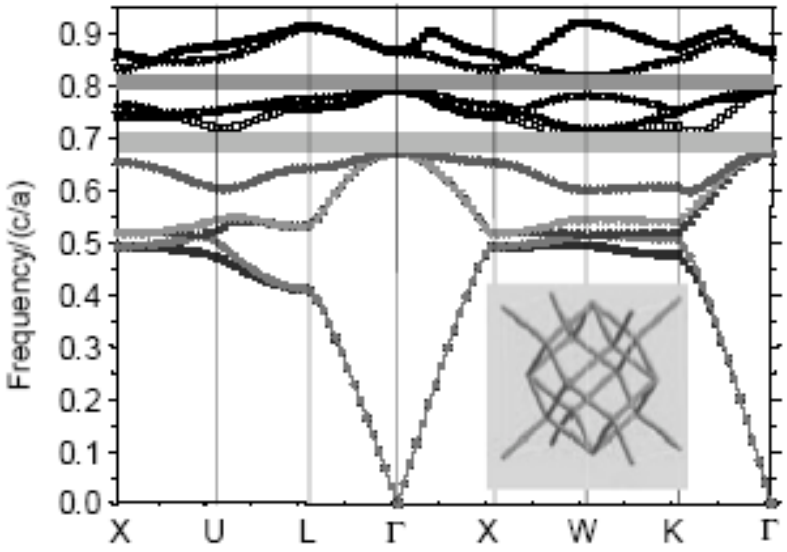

Figure 2.12. Band structure of the skeleton structure with a cylinder radius of *0.096a*. The cylinder is composed of silicon with ε=11.9. The inset shows the cubic unit cell of the skeleton structure with lattice constant *a*.[42]

Inverse titania opals have also been constructed without the use of an opal template. In this method, the ordering of the opal template and the infiltration of the titania background was done at the same time as separately reported by Subramania[45-46] and Subramanian.[47] Nanocrystalline titania with the desired anatase phase was used

instead of alkoxide precursors to reduce the shrinkage associated with the heat treatment induced amorphous-to-anatase phase transformation.[47] Subramanian *et al.* estimated a pore shrinkage of 7%, which was substantially less than the shrinkage reported for alkoxide infiltrated structures.[37-40] Despite the improvement in titania shrinkage, the refractive index of the anatase titania backbone was insufficient for the appearance of a complete PBG, however stop bands were observed at wavelengths corresponding to the PS template sphere size.

While inverse titania opals have already been successfully fabricated, no one has been able to fabricate an inverse opal with good filling fraction and sufficient refractive index to exhibit a full PBG. The research presented in this thesis uses SiO_2 opal templates based on the confinement cell method of PC fabrication due to its ease of use.

2.2 Atomic Layer Deposition

2.2.1 ALD Overview

Atomic layer deposition, pioneered by Toumo Suntola in the 1970s, is a modification of the chemical vapor deposition process that is used to deposit monolayer films.[48] The process was originally called atomic layer epitaxy (ALE) due to the epitaxial nature of the growth. The more general term of ALD is used to describe deposition of films where the film structure does not necessarily have the same structure as the growth substrate. ALD is also referred to as atomic layer chemical vapor deposition (ALCVD), molecular layering, and molecular layer epitaxy in the literature. ALD was originally developed for the deposition of ZnS:Mn and amorphous Al_2O_3 films.

Materials that can be deposited using ALD include oxides, nitrides, II-VI compounds, III-V compounds, and single elements.[49] ALD films can be grown on amorphous and single crystal substrates.

The ALD process proceeds through saturative steps resulting in a constant thickness increase of conformal films. A metal precursor is pulsed into the process chamber where it is chemisorbed on the surface of the substrate. The chamber is then purged to remove any precursor still in the gas phase as well as any physisorbed reactant. The second pulse of nonmetal precursor is now introduced into the chamber. The nonmetal gas chemisorbs on the surface and undergoes an exchange reaction with the metal layer forming a molecular thin film. Gaseous byproducts are also produced which are removed with the subsequent purge. Any unreacted gas and physisorbed nonmetal reactant is also removed from the chamber during the purge. Films are deposited one layer at a time due to the chemisorption of the reactants. Therefore, ALD is a self-controlling process.[48]

A typical ALD run consists of a metal precursor pulse followed by a purge with an inert gas. Next, the non-metal source gas is pulsed, followed again by an inert gas purge. A schematic illustration of the ALD process is shown in Figure 2.13 below.

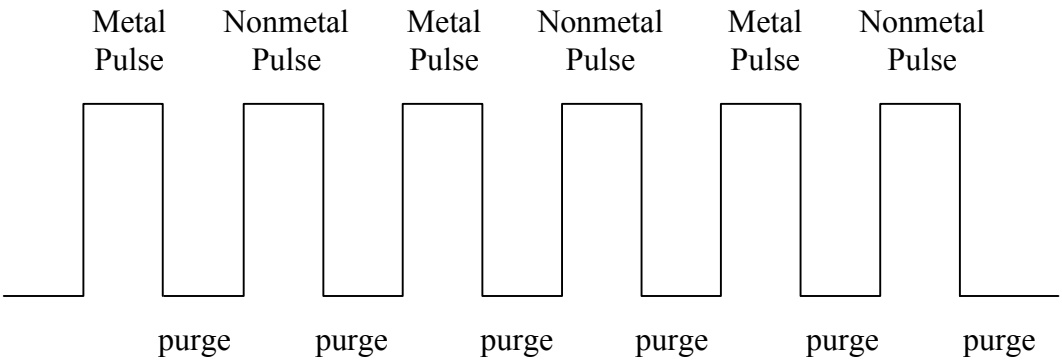

Figure 2.13. ALD Reaction Process

ALD precursors must be volatile, thermally stable, and have rapid reaction with substrate surface groups.[48-50] The precursors must be thermally stable so that they do not decompose at higher temperatures leading to multilayer growth instead of the self-limited ALD growth. In addition to thermal stability, the precursor should not dissolve into the film or etch the film. Dissolution of the precursor into the film is another means for destroying the self-limiting growth mechanism, whereas precursor etching will inhibit film growth. However, dissolution of the precursor is rarely reported in the literature. Unlike CVD, aggressive reactions are preferable for ALD because of quicker reactions and shorter cycle times.

A wide variety of metal precursors have been studied. These fall into five categories: halides, alkyls, alkoxides, electropositive metals, and cyclopentadienyl compounds. Halide research has focused mainly on chlorides, but also on fluorides, bromides, and iodides.[50] Elemental metals such as Zn, Cd, and Hg have also been used as ALD sources.[48] A limited number of precursors have been investigated for the non-metal source. The majority of research has focused on hydrides such as H_2O, H_2S, NH_3, and AsH_3. Hydrogen peroxide (H_2O_2) has also been used as a nonmetal source.

2.2.2 Titania ALD

Titania thin films have been the subject of extensive research due to the many applications in electronic and optical circuits, fuel cell devices, chemical sensors, and photocatalysts. The deposition of ALD titania films has primarily focused on using the metal sources titanium chloride, titanium isoproxide, and titanium ethoxide. More recently titanium iodide has been investigated as a possible precursor. Water and hydrogen peroxide are the primary nonmetal precursors used for titania growth. This thesis is focused on ALD of titania thin films using $TiCl_4$ and H_2O as precursors.

In the idealized TiO_2 ALD reaction between $TiCl_4$ and H_20, the incoming $TiCl_4$ adsorbs on the substrate surface and reacts with surface hydroxyls producing hydrochloric (HCl) gas as a byproduct. Once all of the hydroxyl sites have reacted, no more $TiCl_4$ molecules can be adsorbed on the surface. The extra $TiCl_4$ molecules and byproduct HCl gas is removed from the reaction chamber during the purge sequence. The water molecules then react with the $(\text{-O-})_n TiCl_{4\text{-}n}$ species resulting in a hydroxyl covered surface and more HCl byproducts. The idealized $TiCl_4$ and H_2O reaction proceeds as follows:[51]

$$n(-\mathrm{OH})(\mathrm{s}) + \mathrm{TiCl}_4\ (\mathrm{g}) \rightarrow (-\mathrm{O}-)_n\ \mathrm{TiCl}_{4-n}(\mathrm{s}) + n\mathrm{HCl}(\mathrm{g}) \qquad (2.3)$$

$$(-\mathrm{O}-)_n \mathrm{TiCl}_{4-n}(\mathrm{s}) + (4-n)\mathrm{H_2O}(\mathrm{g}) \rightarrow (-\mathrm{O}-)_n \mathrm{Ti(OH)}_{4-n}(\mathrm{s}) + (4-n)\mathrm{HCl}(\mathrm{g}) \qquad (2.4)$$

However, the TiO_2 reaction is not as simple as indicated by the above reactions. Ritala *et al.* suggested that the growth process consists of several competing chemical reactions, not just the idealized reactions mentioned in the above equations. As shown in Figure 2.14 the TiO_2 surface is covered with hydroxyl groups that are either terminal

or bridging between two Ti cations. The $TiCl_4$ can react with surface hydroxyls in an exchange reaction as described above or it can react with the oxygen bridges as shown in Equation 2.5. While both of these reactions lead to film growth, the reaction in Equation 2.5 leads to slower film growth.

$$\mathrm{Ti(-O-)_2Ti(s) + TiCl_4\ (g) \rightarrow Ti(Cl) - O - Ti(OTiCl_3)(s)} \qquad (2.5)$$

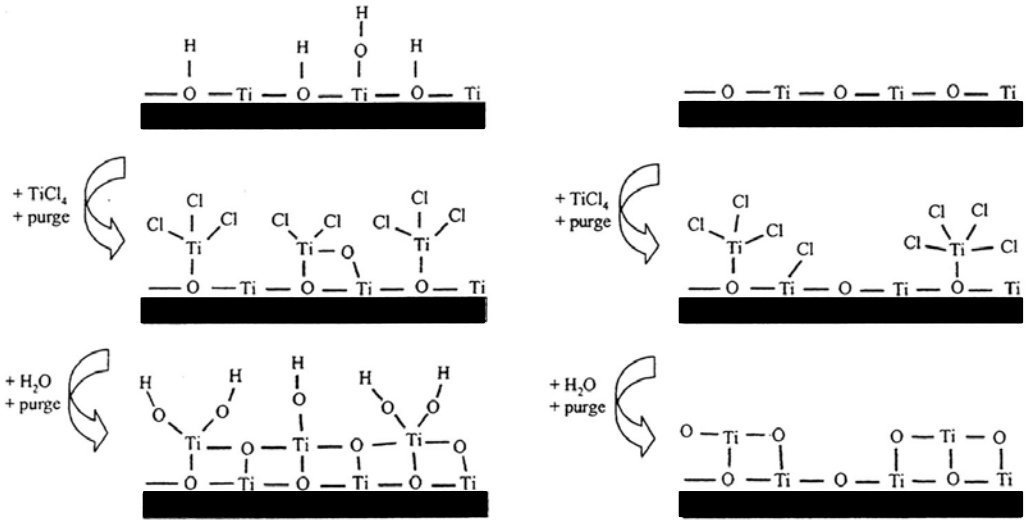

(a) (b)

Figure 2.14. Schematic of TiO_2 growth by (a) exchange reactions with surface hydroxyls and (b) true chemisorption of reactant precursors on the dehydroxylated substrate.[49]

Some reactions can take place that hinder film growth. For example, surface hydroxyls can condense with each other rather than reacting with the $TiCl_4$, thus resulting in a reduction in film growth. The reactions for adjacent and terminal hydroxyls are shown in Equations 2.6 and 2.7, respectively. These reactions result in the dehydroxylation of the surface.

$$\mathrm{Ti(OH)-O-Ti(OH)(s) \rightarrow Ti(-O-)_2\ Ti(s) + H_2O(g)} \tag{2.6}$$

$$\mathrm{2\text{-}Ti(OH)(s) \rightarrow -Ti\text{-}O(s) + -Ti(s) + H_2O(g)} \tag{2.7}$$

The HCl reaction byproducts can also adsorb onto the TiO_2 surface, thereby reducing the number of adsorption sites available to the H_2O molecules and limiting film growth. The reaction of HCl with either surface hydroxyls or oxygen bridges is described in Equation 2.8 and 2.9, respectively.

$$\begin{aligned} \mathrm{Ti-OH(s) + HCl\ (g)} &\leftrightarrow \mathrm{Ti(H_2O)-Cl(s)} \\ &\leftrightarrow \mathrm{Ti-Cl(s) + H_2O(g)} \end{aligned} \tag{2.8}$$

$$\mathrm{Ti(-O\text{-})_2 Ti(s) + HCl\ (g) \leftrightarrow Ti(OH)-O-Ti-Cl(s)} \tag{2.9}$$

The majority of TiO_2 ALD research has been conducted by Mikko Ritala of University of Helsinki and Jaan Aarik of University of Tartu. Ritala *et al.* first published TiO_2 ALE results in 1993.[51] They used a Microchemistry F-120 flow type ALD reactor with a 2 mm channel between substrates to stabilize the flow conditions. The channel between substrates increases the chance of the precursor reacting with the substrate. The overall reactor pressure was approximately 10 mbar. The precursors used for TiO_2 deposition were $TiCl_4$ and H_2O, which were temperature controlled in water baths at 25°C and 20°C, respectively. Reactants were transported into the reaction chamber using nitrogen gas. Pulse and purge times were typically 0.2 s and 0.5 s, respectively. The film growth was studied for both amorphous and crystalline substrates at temperatures between 150 and 600 degrees Celsius. The film growth rate, crystal structure, optical

properties, and composition were investigated. A theory for the ALD film growth of TiO_2 was also presented.

Film growth occurred at all temperatures in the 150 to 600°C range with reported growth rates between 0.35 and 0.56 Å/cycle. The growth rate appeared to be substrate dependent as shown in Figure 2.15. The growth rate for soda lime glass increased with deposition temperature, whereas the growth rate for Corning 1733 was temperature independent. The decrease in the growth rate of soda lime glass from 150 to 200°C was due to the desorption of H_2O at low substrate temperatures. The growth rate between 200 and 400°C appeared to be limited by reaction kinetics as demonstrated by the 14% increase in growth rate when the pulse length at 300°C was increased from 200 ms to 400 ms. Increasing the purge length had the opposite effect, resulting in a 9% decrease when the purge length was increased from 500 ms to 1000 ms. The growth rate stabilized at 400°C, although it did decrease slightly due to dehydroxylation of the surface at higher temperatures.

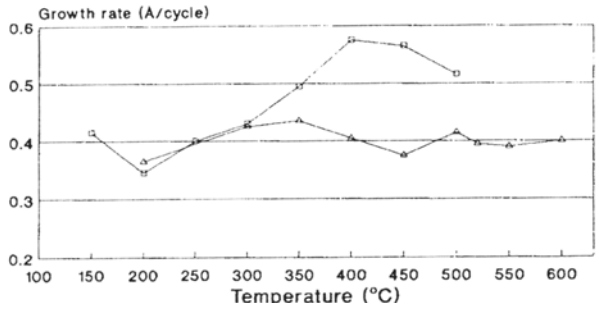

Figure 2.15. Growth rates on soda lime glass (squares) and Corning 1733 glass (triangles) substrates as a function of temperature.[51]

As shown in Figure 2.16 there was a decrease in the growth rate as the number of cycles increased. This was most likely due to a decrease in the hydroxyl group density as a result of condensation reactions on the surface. Since hydroxyl groups are more effective adsorption sites than the surface oxides, the reduction of the number of hydroxyl groups resulted in the decreased growth rate.

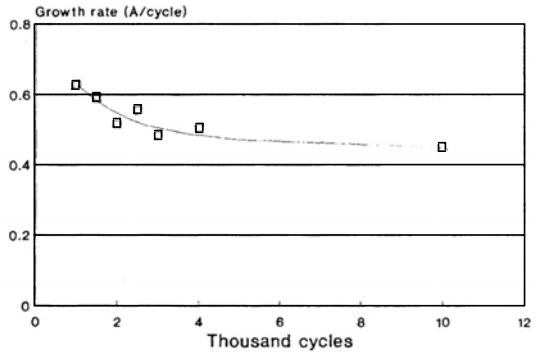

Figure 2.16. Growth rate at 500°C as a function of the number of reaction cycles used.[51]

An uneven thickness profile was observed on the substrate. As shown in Figure 2.17, the thickness tapered to a constant value about 15 mm from the leading edge. The increased thickness at the leading edge was believed to be due to CVD growth from the desorption of precursor gas species from the tube walls between precursor pulses. If the thickness profile resulted from CVD, the desorbed species would be exhausted shortly after the crossing point of the two precursors, therefore moving the substrate further away from the crossing point would eliminate the thickness profile. However, it was found that the thickness profile actually resulted from HCl re-absorption on the later region of the surface. As the $TiCl_4$ pulse reaches the -OH groups on the leading edge of the sample, HCl is produced and carried along the sample where some fraction re-absorbs to the

surface, thereby reducing the number of surface site available to $TiCl_4$ molecules. The solution to this thickness profile is to introduce a dummy sample used to generate HCl ahead of the actual sample. This results in a lower growth rate, but the film is more uniform.

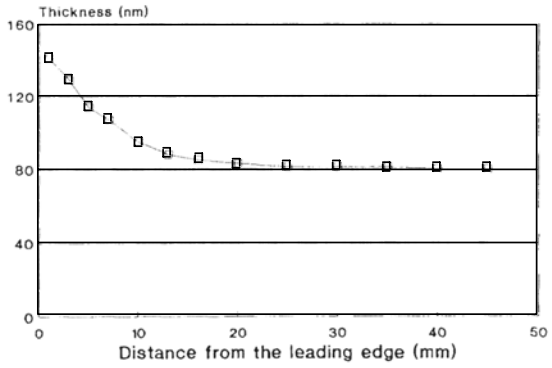

Figure 2.17. Film thickness as a function of distance from leading edge of the substrate. The film was deposited onto Corning 1733 at 600°C using 2000 reaction cycles.[51]

XRD revealed that all films grown on amorphous substrates were amorphous even at substrate temperatures of 600°C. The films grown on crystalline substrates were crystalline with either anatase or rutile structure. Only the anatase (101) and (004) peaks were observed for a growth temperature of 500°C on a silicon substrate, however rutile peaks were observed at the same temperature for mica substrates. Crystal structure was not reproducible. Partial orientation was observed in both anatase and rutile films, however conclusions on preferred orientation were hindered by the difference in intensity of the thin film as compared to the powder version of TiO_2.

SEM showed the films to be smooth and crack free with an approximate grain size of 100 nm. A chlorine content of 2 at.%, as measured by RBS, was observed in the

film grown at 150°C. However, no chlorine was detected in films grown at 500°C. The hydrogen content of the film, most likely due to adsorbed water and hydrocarbon contamination, was measured at 0.3 at% at 150°C and 0.1 at% at 500°C.

The refractive index at a wavelength of 580 nm increased from 2.4 at 150°C to 2.6 at 450°C. Film thickness did not have any effect on the index.

Aarik *et al.* first reported TiO_2 ALD growth using $TiCl_4$ and H_2O as precursors in 1995.[52] Deposition was done in a flow-type low-pressure hot-wall ALD reactor. The reaction zone had two different configurations. The first was a channel-type reactor similar to that used by Ritala *et al.* with a channel height of 2 mm. The second set-up was an open configuration where the substrate lies on a graphite susceptor in a 35 mm diameter quartz tube. The films were grown at a pressure of 250 Pa, which corresponds to the pressure of the nitrogen carrier gas. Carrier gas flow rates were typically 0.8 and 15 m/s in the open type and channel type reactors, respectively. The precursors were kept at room temperature. A typical cycle consisted of a 2 s $TiCl_4$ pulse, followed by a 1s purge, then a 1s H_2O pulse, followed by a 2s purge. The flow rates for $TiCl_4$ and H_2O were 1.2×10^{-3} and 0.73×10^{-3} Pa m^3/s, respectively. Films were grown on amorphous and crystalline substrates at reactor temperatures of 100 to 500°C.

As shown in Figure 2.18 the growth rate decreased drastically as the growth temperature increased, which is in disagreement with the results reported earlier by Ritala *et al.*[51] Aarik *et al.* used longer pulse times than Ritala *et al.*, which is most likely the cause of the increased growth rate at low temperatures. The increase in growth rate was probably due to CVD-like multilayer adsorption, whereas the decrease in growth rate for Ritala *et al.* was caused by slow reaction rates.[49]

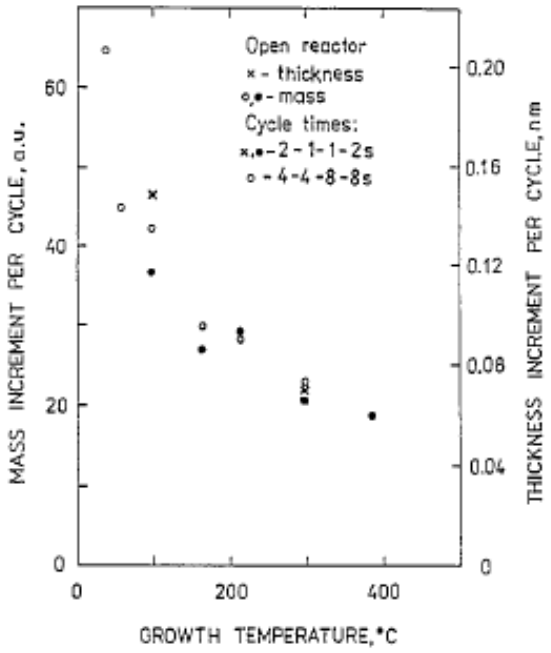

Figure 2.18. Deposition rates measured by quartz microbalance and calculated from the transmission spectra as functions of growth temperature.[52]

Films grown at temperatures above 165°C were nearly stoichiometric TiO_2, but residual chlorine was found in the films grown at 100°C. The chlorine/oxygen ratio at a deposition temperature of 100°C was 0.014. Films deposited at 100°C had a relatively smooth surface, whereas surface roughening and agglomeration on the film surface occurred as the growth temperature was increased.

Unlike Ritala, Aarik *et al.* reported the growth of crystalline films on both amorphous and crystalline substrates. Films grown below 140°C had an amorphous structure, whereas polycrystalline structure appeared at deposition temperatures at or above 165°C regardless of the crystallinity of substrate. Films grown at 210°C revealed polycrystalline anatase structure for film thicknesses of 15 to 55 nm. Thicker films showed preferred orientation of the crystallites with the [110] normal to the substrate.

Films grown at 300°C showed anatase structure at thickness of 2 nm. Thus, the minimum thickness for crystallization to occur decreases as the deposition temperature increases. Rutile crystal structure began to appear in films grown at or above 350°C. Films grown at 400 and 500°C had a mixed anatase and rutile crystal structure, with rutile being the dominant structure. No preferred orientation was observed in these films. It was concluded that chlorine contamination hindered crystallization at low deposition temperatures thereby reducing the stoichiometry of the films.

Further data on the optical properties[53] and growth mechanisms[54] of $TiCl_4$ precursor ALD films were presented in papers published by Aarik *et al.* in 1997 and 2001, respectively. The absorption of the TiO_2 films increased with increasing deposition temperature as shown in Figure 2.19.[53] Recall from Section 2.1.2 that a non-absorbing film is essential to photonic crystal applications for the coherent localization of light. Therefore, the increase in absorption at higher deposition temperatures is discouraging because the high temperatures needed for development of the rutile phase will result in an increase in the absorption of the film.

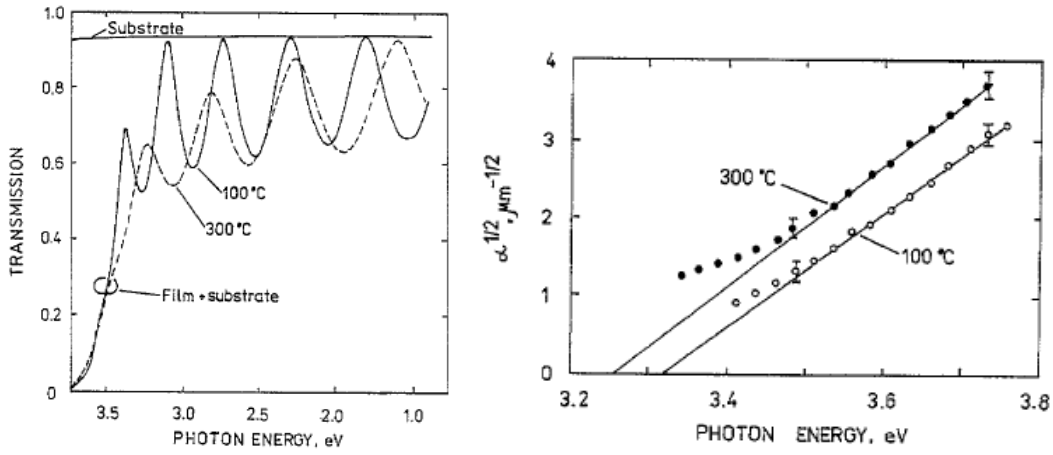

(a) (b)

Figure 2.19. (a) Transmission spectra of the films grown on silica substrates at 100 and 300°C. The thickness of the films are 460 and 320 nm, respectively. (b) Dependence of $\alpha^{1/2}$ on photon energy determined for films grown at 100 and 300°C.[53]

An increase in the refractive index was observed up to 300°C, followed by a decrease at 400°C. The decrease in the refractive index at 400°C was unusual because the rutile structure should have a higher index than the anatase structure. The decrease in refractive was attributed to the decreased order of crystallites in rutile films as well as the presence of voids in the rutile film that were not present in the anatase film. The difference in refractive index values reported in Figure 2.20 is because the optical constants in Figure 2.20(a) were calculated from the transmission spectrum, whereas the data presented in Figure 2.20(b) was measured by ellipsometry.

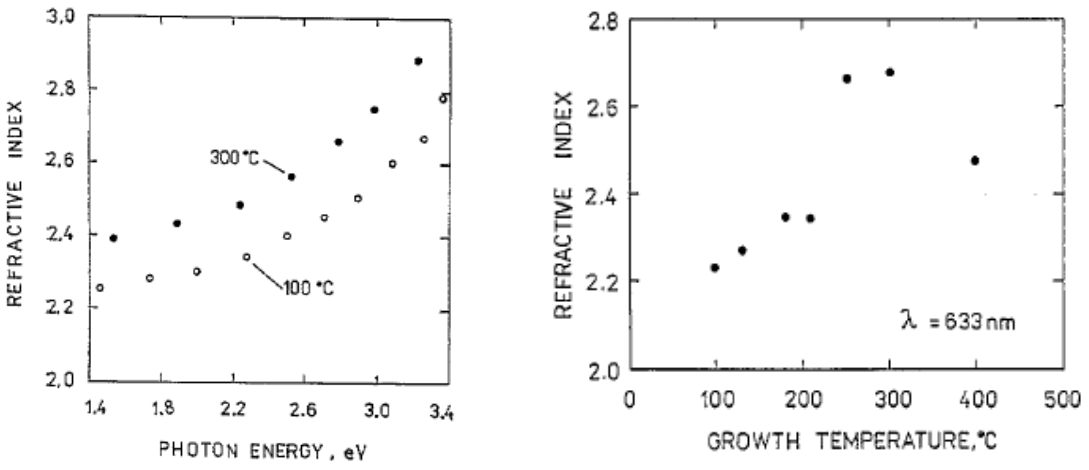

(a) (b)

Figure 2.20. Refractive index versus (a) photon energy and (b) growth temperature.[53]

Aarik *et al.* also reported the growth of a fourth polymorph of TiO_2 known as TiO_2-II.[55-56] TiO_2-II is a high-density crystal modification of titania that has the same crystal structure as α-PbO_2. A mixture of rutile and TiO_2-II was initially observed at a substrate temperature of 400°C,[55] although it was later found that mixtures of rutile and TiO_2-II could be grown between temperatures of 375 to 550°C.[56] The water vapor pressure during the water pulse reportedly controlled the percentage of rutile to TiO_2-II.[55] The $TiCl_4$ vapor pressure was kept constant during the experiments. Films grown at low H_2O pressures were typically of the TiO_2-II structure, whereas higher H_2O pressures resulted in the rutile structure.

Further investigation revealed that the TiO_2-II structure was only observed in films below a critical thickness.[56] Films exceeding this critical thickness showed mixed rutile/TiO_2-II character, with the amount of rutile phase increasing with increasing thickness. The critical thickness was dependent on the precursor dose and purge times.

No refractive index data is reported for the TiO_2-II polymorph, however it is most likely higher than that of the rutile structure due to the higher density of the α-PbO_2 structure.

We have constructed a home-built ALD system for the deposition of TiO_2 thin films. Our research has focused on $TiCl_4$ and H_2O as reactant precursors, due to the wide range of temperatures that result in film growth. The main motivation of our work was to develop a reliable method for growing uniform, conformal coatings of titania in synthetic opal films. Since rutile titania has the highest refractive index, we originally sought to grow rutile films directly in the opal. However, the roughness of the crystalline titania films (both anatase and rutile) resulted in poor quality opal infiltrations. To circumvent this limitation, we investigated the growth of amorphous titania films followed by heat treatments to convert to rutile.

2.3 Heat Treatment of Titania

The heat treatment of titania is the topic of frequent research due to the exceptional optical properties of the high temperature rutile phase. Despite the high index of the bulk rutile structure, it is difficult to make thin films of rutile titania with comparable refractive index. Since the high index rutile structure is hard to grow, the thin films are often heat treated in order to improve the optical properties of the film. While the effect of heat treatment has been studied previously for titania thin films deposited by sputtering,[57,58,59] evaporation,[60] metal organic CVD,[61] and sol-gel dip coating,[62] there is very little data published for the heat treatment of titania ALD films.

Since the optical properties of titania are strongly process dependent,[15] the effect of heat treatment on our ALD films will be investigated.

Martin *et al.* conducted a thorough study of the heat treatment of TiO_2 films deposited by rf magnetron sputtering in 1997.[58] The films were deposited at a temperature of 150°C resulting in a thickness of approximately 400 nm. Films were annealed for 1 hour at temperatures from 300 to 1100 degrees Celsius. XRD of the heat-treated samples began to reveal signs of anatase structure at 300°C. The phase transformation from anatase to rutile took place somewhere between 700 and 900°C, however the films were not completely converted to the rutile phase until 1100°C. The anatase films were randomly oriented at 300°C, but began showing preferred orientation in the (101) direction at 700°C. The rutile preferred orientation at 1100°C was (110). The XRD patterns for samples heat treated at different temperatures are shown in Figure 2.21.

The RMS roughness decreased gradually from 150 to 500 degrees, and then increased sharply above 700°C with the onset of the rutile phase transformation.

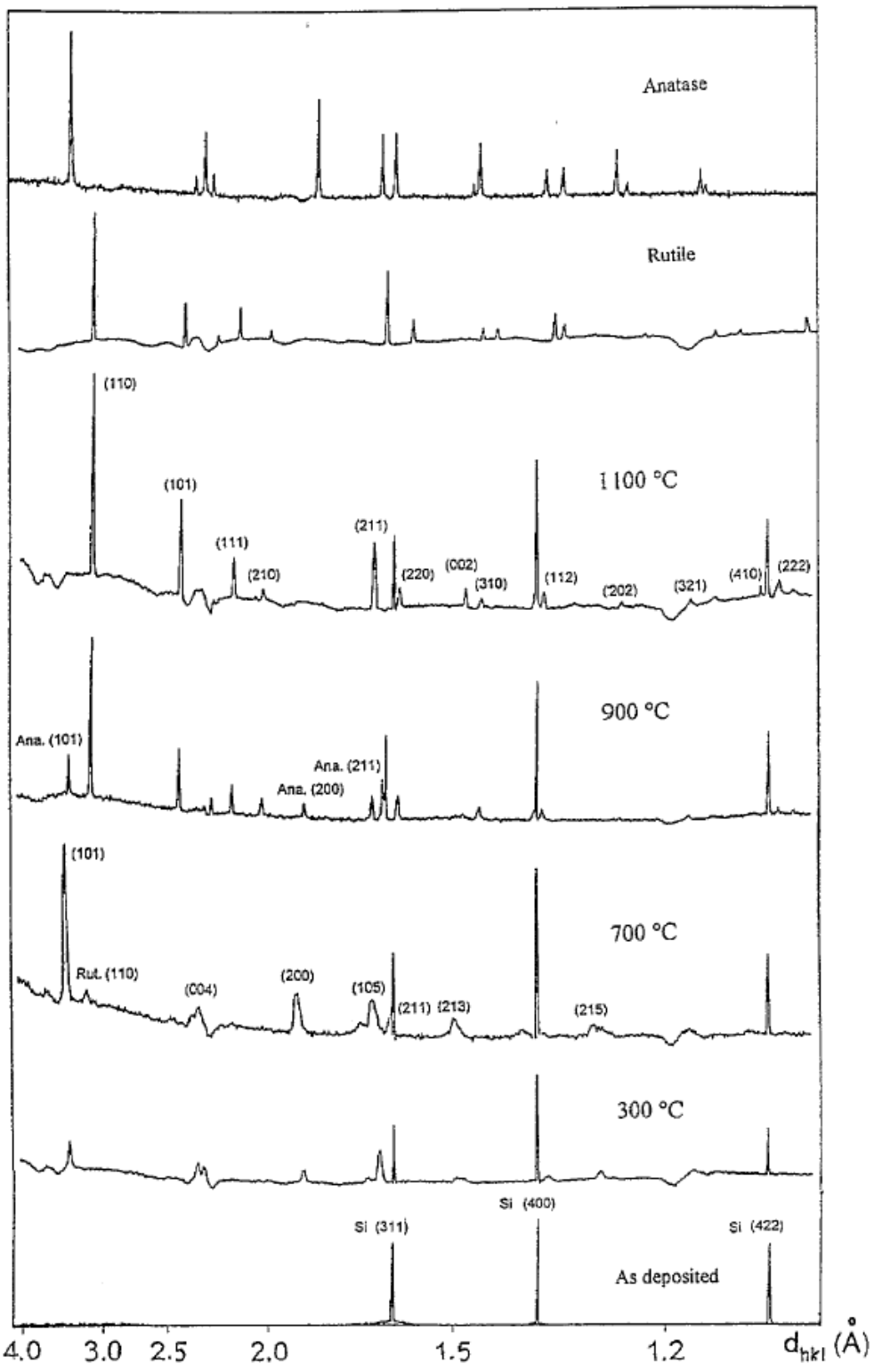

Figure 2.21. X-ray diffraction patterns of TiO_x, thin films at different annealing temperatures and as deposited on (100) silicon. Top curves represent a typical X-ray spectrum TiO_2 powder sample crystallized in the rutile and anatase structure.[58]

The transmittance decreased weakly with increasing temperature for temperatures below 700°C, then drastically at temperatures of 900°C and above as shown in Figure 2.22. The index of refraction and extinction coefficient, as shown in Figure 2.23, increased with increasing temperature. However, the increase shown was due to the densification of the TiO_2 film rather than the existence of the rutile phase since it did not appear until 700°C.

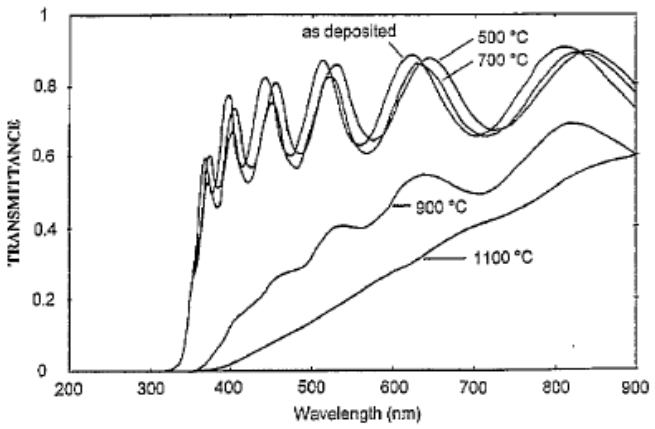

Figure 2.22. Optical transmittance as a function of wavelength of titanium oxide thin films.[58]

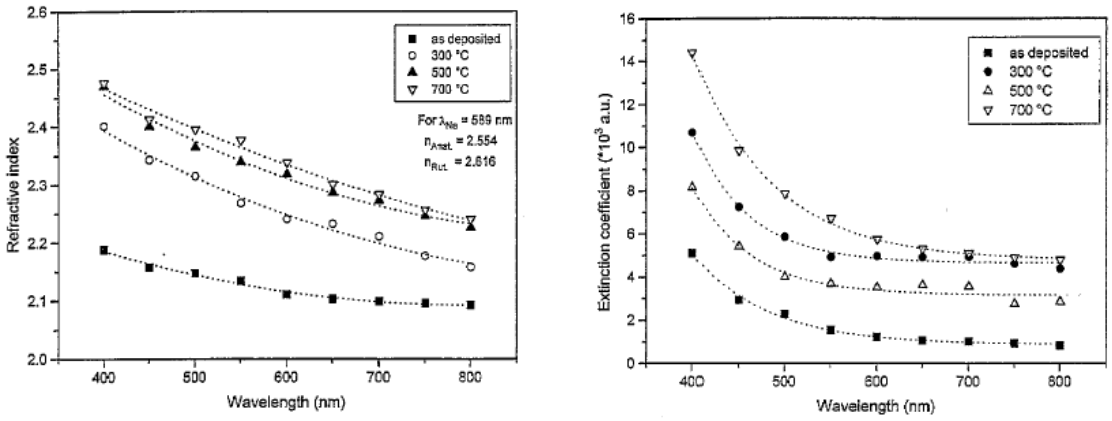

(a) (b)

Figure 2.23. The variation of (a) refractive index and (b) extinction coefficient as a function of wavelength of titanium oxide films before heat treatment and for annealing temperatures contained between 300°C and 700°C.[58]

Mardare *et al.* also reported data on the effects of thermal treatment on the structure of titania films.[59] The films examined were TiO_2 deposited by DC sputtering on a quartz substrate. The films were amorphous and had a thickness of 300 nm. The samples were heat treated in air at 400, 600, and 900°C for 12, 2, and 3 hours, respectively. XRD of the films showed mixed anatase and rutile phases, indicating that rutile phase conversion can occur at temperatures below that reported by Martin *et al.* if the anneal time is long enough. The sample annealed at 400°C for 12 hours showed a weight percentage of 54% anatase. Weight percentage calculations are based on Spurr and Myer's formula,[63] which will be presented in detail in Section 3.5.1. The weight percentage of anatase increased to 78% for a 2 hour anneal at 600°C. Rutile was the dominant phase in the sample annealed at 900 degrees for 3 hours, which only had a 25% anatase weight percentage.

The refractive index as measured at a wavelength of 552 nm increased from 2.21 for as deposited amorphous films, to 2.62 for films with a majority of the rutile phase. Index values reported were slightly higher than those reported by Martin *et al.* which could be process dependent or a result of the nonstoichiometry of the films studied by Martin *et al.*

The anatase to rutile phase conversion temperature as well as the refractive index of the deposited film is highly process dependent. There is even variation in the index of refraction within a particular process as demonstrated by the difference in results reported by Martin,[58] Mardare,[59] and Suhail.[57] The first appearance of rutile phase has been reported anywhere between 300°C and 800°C. Therefore, the conversion temperature

and index of our ALD TiO_2 will be investigated and compared to the results summarized above.

CHAPTER 3

EXPERIMENTAL METHODS AND PROCEDURES

3.1 Inverse Opal Synthesis

SiO_2 opals were fabricated using a variation of the confinement cell process introduced by Park and Xia in 1999.[31] The confinement cell was used as a guide for the self-assembly of silica colloidal spheres, which automatically formed an FCC structure. However, silica does not have sufficient refractive index for a full PBG to emerge. Therefore, the SiO_2 PC structure was then used as a template for the ALD infiltration of the high index material TiO_2. The SiO_2 spheres were etched out leaving a TiO_2 inverse opal.

3.1.1 Fabrication of Confinement Cell

A confinement cell composed of epoxy-based photoresist was fabricated using traditional photolithography methods. The cell was made in a four-step process: aluminum mask level, aluminum deposition and lift-off, gasket mask level, and gasket removal.

In the first step, glass microscope slides from Corning (No. 2947 75x50) were spin-coated with Shipley's 1813 positive photoresist. The slide was exposed to UV light for 6 sec through a mask containing a square of parallel lines. A schematic of the first mask level is shown in Figure 3.1a. The photolithography process was carried out on a Karl Suss MJB-3 mask aligner. The slide was soaked in chlorobenzene for 10 minutes

before developing in order to bevel the edges of the photoresist for easier aluminum lift-off later in the process. After a 10 minute bake, the slide was developed for 30 seconds in Shipley's AZ-351, a solution of 1-5% sodium hydroxide.

Subsequent to developing the photoresist, a 130 nm film of aluminum (Al) was deposited using a Veeco electron beam evaporator. The unwanted aluminum was then lifted off by placing the sample in an acetone bath agitated by an ultrasonic cleaner. The sonication of the bath had multiple benefits. First, sonication of the slide allowed for easier lift-off of the unexposed aluminum film. Second, the sonication also resulted in better-defined Al lines.

The aluminum patterned substrate was then spin-coated with Microchem's SU-8 2010 negative resist. The confinement cell process originally used SU-8 10 photoresist. However, SU-8 2010 produced cells with much cleaner edges and shorter development times. The film thickness was 10 μm. The SU-8 film was exposed through a square mask for 2 min. See Figure 3.1b for a schematic of the mask. After developing, a square epoxy cell with shallow grooves was left on the slide. The cell was 10 μm thick, 2 cm on a side, with 150 nm deep grooves on the underside of the cell as shown in Figure 3.1c.

The cell was separated from the aluminum lines by soaking the slide in water. The aluminum-patterned substrate should be soaked in acetone after removal of the gasket. In the original process the gasket was removed by etching the aluminum with AZ-351. However, it was later realized that the gasket could be removed from the aluminum pattern by soaking in water overnight. This procedure allows for the reuse of the aluminum-patterned substrate, which reduces gasket fabrication time by eliminating the first two steps in the process.

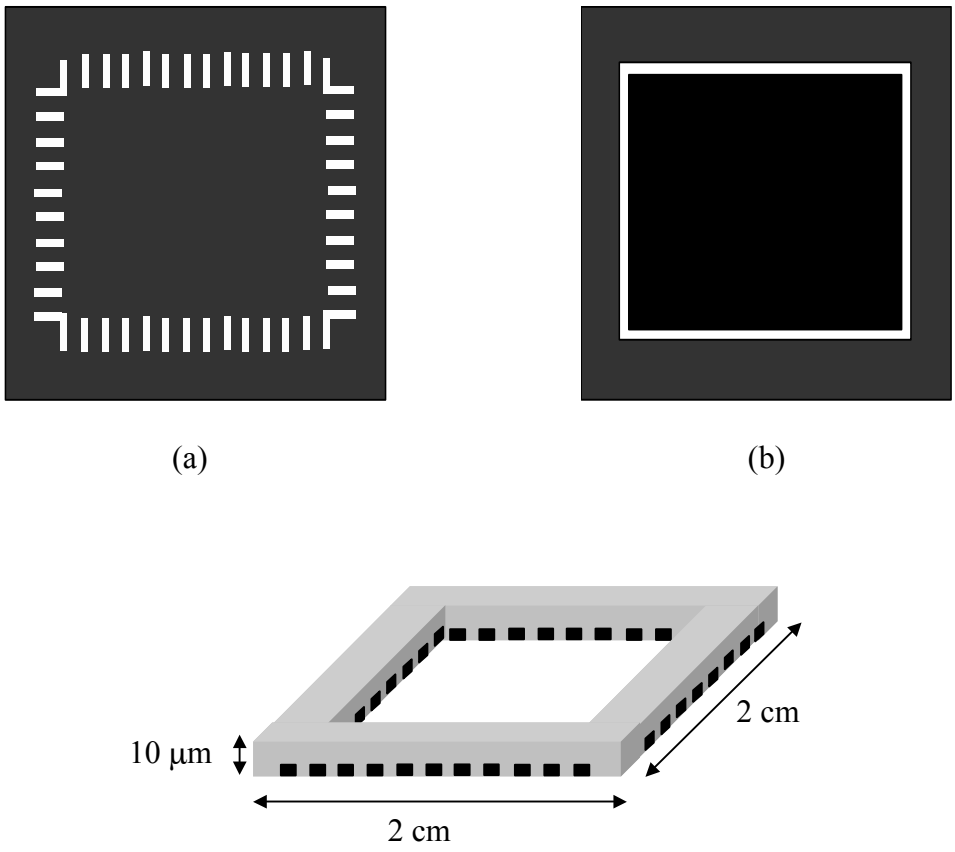

Figure 3.1. Schematic of Confinement Cell Process (a) mask level 1, (b) mask level 2, and (c) schematic of gasket. Schematics are not to scale.

A more detailed description of the confinement cell fabrication process is included in Appendix A.

3.1.2 Fabrication of Synthetic Opal

The confinement cell was sandwiched between silicon or quartz substrates and a top glass plate. Silicon was required for this thesis because the hydrofluoric (HF) acid used to etch out the silica spheres in the inverse opal process would attack the quartz substrate. The top glass plate has a small 1/8" hole drilled in the center where a 3" glass

feedtube was attached with epoxy resin. The colloidal solution was introduced to the cell through this feedtube as shown in Figure 3.2.

Monodispersed silica spheres were made through the Stober process, which is basically the hydrolysis of metal alkoxides in alcoholic solution.[64] Tetraethylorthosilicate (TEOS) was hydrolyzed in the presence of an ammonia catalyst in order to make silica spheres. Spheres were also purchased from companies such as Duke Instruments Corporation. However, spheres of the size scale needed for this research were hard to purchase commercially. Spheres were made in the size range of 190 to 440 nm.

After introducing the colloidal solution into the feedtube, a positive pressure was applied to the cell by the flow of N_2 gas. Water from the colloidal solution escaped from the gasket through capillary forces leaving behind the silica spheres. Cells are sonicated in order to facilitate the self-assembly process of the spheres. Depending on the concentration of the colloid, an opal film could be assembled in 1 to 5 days. The opals were dried in air for several hours before removing the gasket.

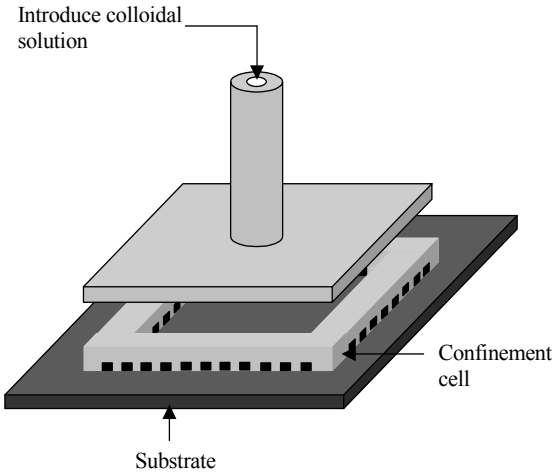

Figure 3.2. Schematic of opal synthesis process.

The synthetic opals were sintered in air for 2 hours at 800^{o}C to remove the water and promote necking of the spheres. The temperature was ramped at a rate of 10^{o}C/minute. Necking of the spheres promotes the structural stability of the opal, which allows the opal to withstand further processing such as infiltration and etching.

Opal films of dimensions of 20 mm by 20 mm were fabricated using the process described above. The opals were composed of grains that were approximately 20-100 microns in length and aligned in multiple directions. The (111) plane of the opal grows parallel to the substrate.

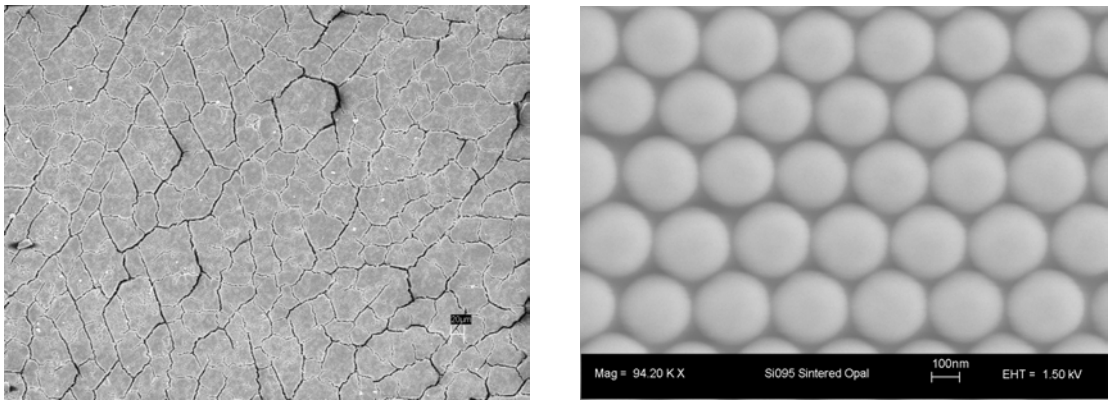

(a) (b)

Figure 3.3. (a) SEM micrograph of opal grains. Scale bar = 10μm. (b) SEM of (111) plane of opal. Image courtesy of J. S. King.

3.1.3 Fabrication of Inverse Opal

Photonic crystals fabricated using self-assembly have an FCC structure. An inverse opal can be fabricated by infiltrating the opal template with a high index dielectric material such as titania. The infiltrated material was deposited using atomic layer deposition, a modified CVD process. TiO_2 was deposited at a substrate temperature

of 100°C in order to achieve smooth, conformal growth. The resulting film was amorphous. The infiltrated opal was then heat treated at 400°C for 2 hours in order to convert the amorphous TiO_2 film to the anatase crystal structure. This step is required for the selective etching of the SiO_2 spheres, since TiO_2 will also etch in HF if it is not in crystalline form. The opal was then ion milled for 15 minutes at an angle of 15° from parallel to remove the top layer of the TiO_2 so that the SiO_2 etchant could penetrate the opal surface. After milling, the silica spheres were etched in 2% hydrofluoric (HF) acid for 30-45 minutes. The resulting PC structure was composed of a thin backbone of titania and a large air space, as illustrated in Figure 3.4 below.

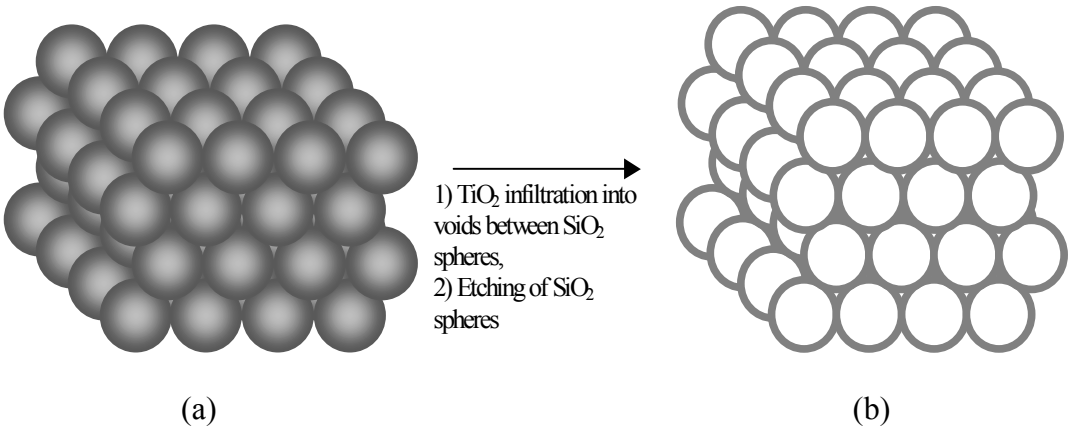

Figure 3.4. Schematic of the Fabrication of Inverse Opal: (a) FCC packing of SiO_2 spheres in synthetic opal and (b) Thin TiO_2 coating of air spheres in FCC arrangement.

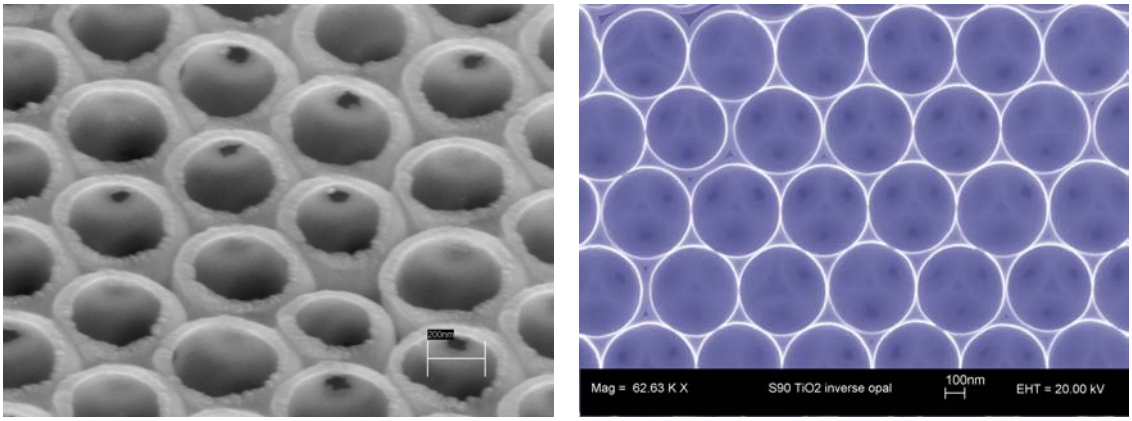

Figure 3.5. SEM micrograph of an inverted opal. (a) The top surface of the opal was ion milled for 60 minutes so that the inside of the TiO_2 shell was exposed. Scale bar = 200 nm. (b) Top-down view of an inverted opal. Image courtesy of J. S. King.

3.2 Atomic Layer Deposition System

3.2.1 Final ALD Configuration

Titania films were deposited using a custom-made flow-type ALD reactor as shown in Figure 3.6, which consists of a heated reaction chamber and a gas control system. The deposition tube was made of 1.5 mm thick quartz. The process tube was heated using a Thermolyne F79440 furnace, which has a 24" long heat zone with a temperature range of 100 to 1200 degrees Celsius. Nitrogen was used as a carrier and purge gas. A MKS 1179A Mass-Flow Controller was used to control the nitrogen gas flow which was typically set to 200 sccm. Chamber pressure was measured using an MKS Instruments Baratron type 722A absolute pressure transducer.

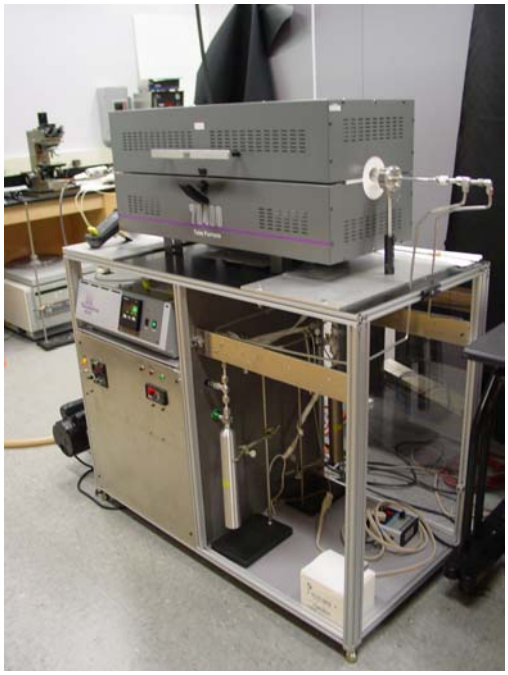

(a)

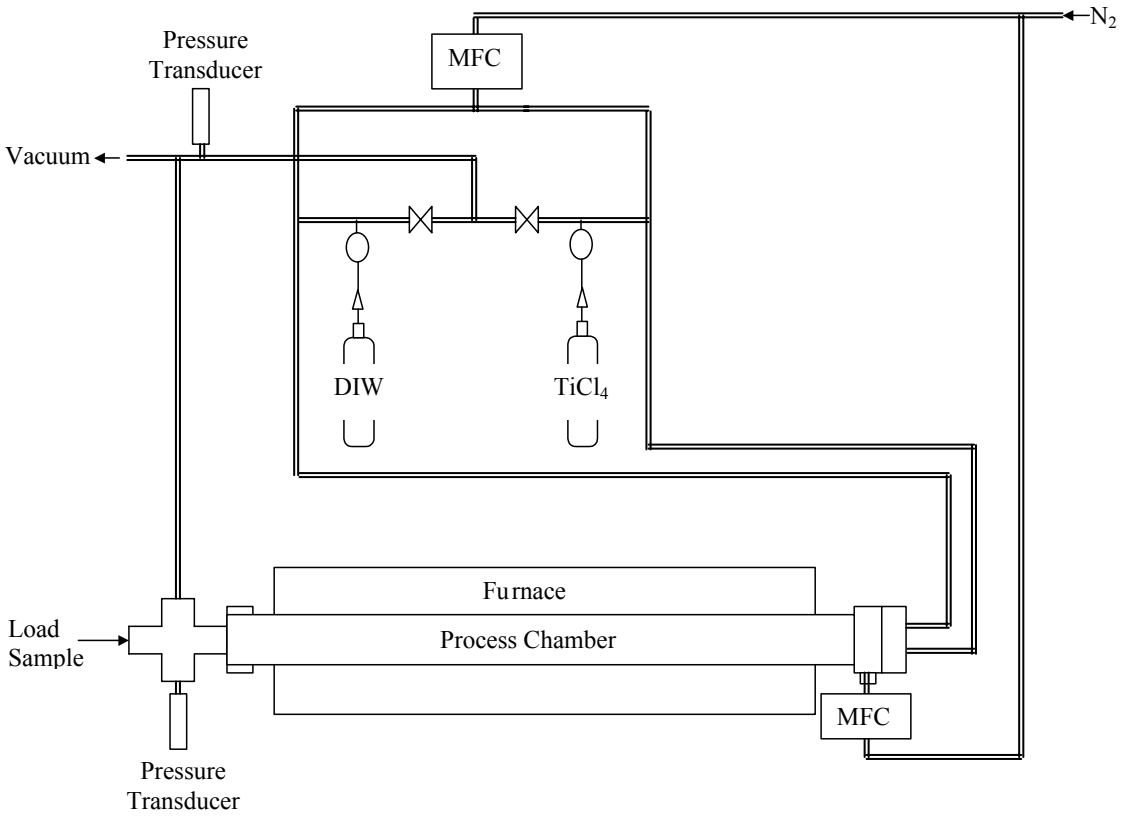

(b)

Figure 3.6. ALD System (a) picture and (b) schematic.

The titania precursors were 99.0% $TiCl_4$ from Alfa Aesar and deionized H_2O (DIW). The DIW was produced using a Barnstead Nanopure Diamond system. The deionized water had a resistivity of ~18.2 Ω/□. Both sources were housed in separate stainless steel (SS) containers, which were held at room temperature. Precursor sources were controlled with a Skinner 71215 2-way, normally closed solenoid valve. Source flow was restricted by a needle valve, which was set to 0.500 for the DIW source and left wide open for the $TiCl_4$ source.

The precursor gases were introduced to the process chamber through separate SS tubes. Each inlet tube had an outer diameter (OD) of ¼" and protruded 5" into the process chamber. A separate N_2 line was also attached to the front of the reaction chamber in order to eliminate any dead space behind the gas inlet tubes. The extra N_2 line was set at a flow rate of 25 sccm at all times during the ALD process.

Silicon (100) and quartz, approximately 1 cm by 2 cm in size, were used as substrates. Substrates were cleaned using an organic solvent rinse of acetone, ethanol, and DIW and were housed on a quartz boat in order to keep samples flat in the reaction chamber. The boat, shown in Figure 3.7, had an indented channel where the sample sits so that its surface is even with the boat surface. A dummy substrate was placed in front of the sample in order to eliminate any thickness gradient due to readsorption of the HCl byproduct. The front edge of the boat was sloped to minimize gas flow turbulence.

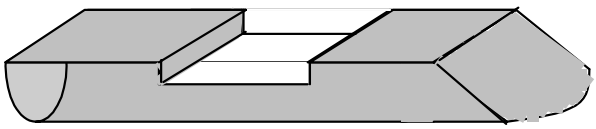

Figure 3.7 Schematic of quartz sample boat.

The system was kept under low pressure using an Alcatel Pascal series 2033C2 rotary vane vacuum pump with a nominal flow rate of 30 m^3/h. Typical chamber pressure values ranged between 1 and 8 Torr. Fomblin Y25/6 oil, purchased from Kurt J. Lesker, was used in the vacuum pump for increased resistance to corrosive gases. Unlike most synthetic oils, Fomblin is a perfluoropolyether. All seals within the ALD and vacuum pump system were chemical resistant Viton. The nitrogen bubbler and gas ballast purge were both used to pump 5 scfh of nitrogen through the pump at all times.

A Mystaire 10 gallon scrubber was used to clean the pump exhaust gases. The scrubber solution was composed of 5 wt.% NaOH pellets in water resulting in a starting pH of 13.3. 100% sodium hydroxide pellets were purchased from Alfa Aesar.

3.2.2 ALD System Improvements

Originally a home-built scrubber was used to clean the exhaust gases, but the capacity was insufficient to handle the volume of exhaust gases from the vacuum pump. This constriction caused backflow from the scrubber to flow into the vacuum pump resulting in corrosion of the pump. The pump oil was contaminated with titania, water, and glass beads from the scrubber in addition to rust particles. The pump was disassembled and cleaned with Perfluorosolv (PFS-2), a perfluoropolyether solvent, purchased from Kurt J. Lesker. While there was rust on the outer casing of the pump, the rotors were not damaged. The metal parts were baked after the solvent clean and the pump was reassembled.

After the pump was cleaned and reassembled, N_2 lines were added to the pump to decrease the accumulation of titania contamination. One line was connected to the oil

bubbler. The bubbler line constantly agitates the oil with N_2 in order to saturate the oil with nitrogen. The other line was connected to the gas ballast to further dilute the corrosive gasses entering the pump. In addition to the nitrogen purge lines, a commercial scrubber with a capacity of ten gallons was added to the system to replace the home-built scrubber. However, titania particles continue to collect in the pump despite these corrective measures. The titania coating does not seem to reduce the effectiveness of the vacuum pump.

Several different configurations were used for the inlet gas plumbing before the optimal configuration was determined. In the original system the gas reactants met in a type 304 stainless steel tee approximately 3 inches outside of the furnace tube, which was held at room temperature. A schematic of this gas configuration is shown in Figure 3.8. Clogging, due to the premature chemical reaction of the precursors at room temperature, was often a problem at the joint where the reactant gases first met. Clogging of the tee joint between the incoming nitrogen carrier gas and the $TiCl_4$ solenoid valve was also an issue, although it was not as bad as the clogging in the tee where the gases first met. The $TiCl_4$ line was heated from the solenoid valve tee to the beginning of the furnace tube in an effort to eliminate the clogging. While heating the line did result in a delay of the clogging, it did not completely eliminate the issue. Also, heating the $TiCl_4$ line had detrimental effects on the deposited film quality such as charring and flaking of the deposited film. The clogging problems were eventually eliminated by changing the incoming gas configuration so that the precursor reactants did not meet until they were well inside the process chamber.

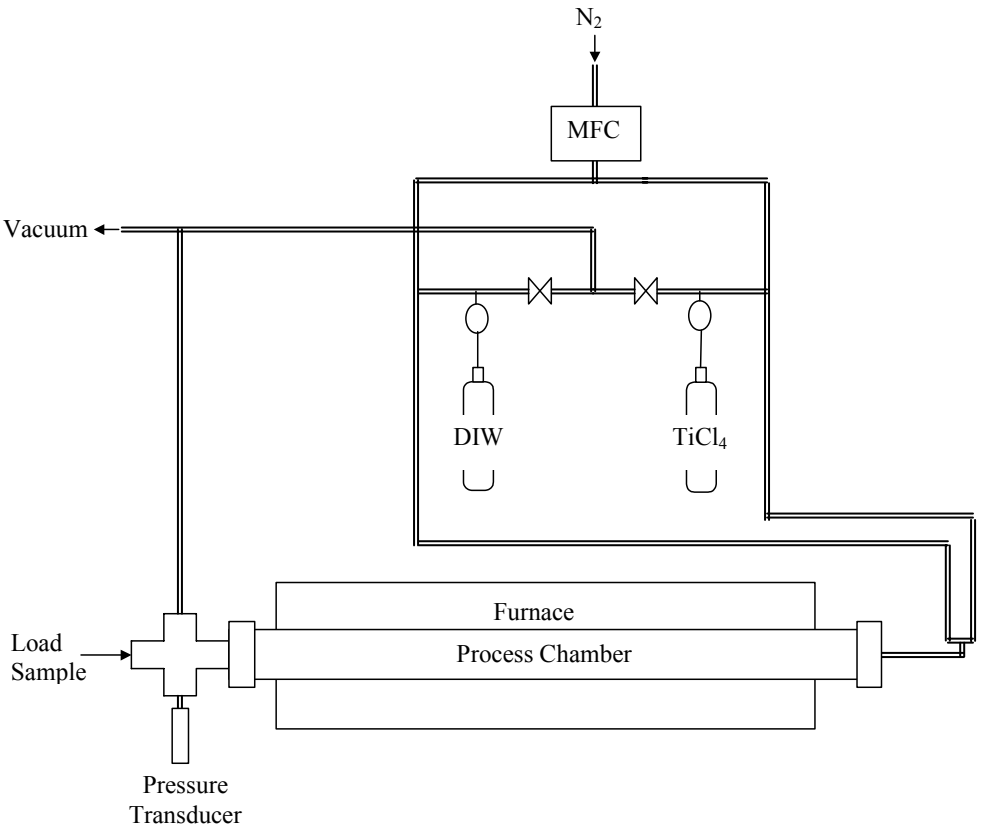

Figure 3.8. Original gas configuration.

In the second configuration, the gases were introduced into the reaction chamber through separate ¼" OD by 10" long quartz tubes which were part of the process tube itself. This configuration is illustrated in Figure 3.9. Unlike the previous configuration, the gases met inside the furnace, and therefore were roughly at the same temperature as the substrate. While this configuration eliminated the clogging problem, the design was very fragile. Because of the shorter length of the process tube, the sample could only be a maximum of 12" from the gas inlet, which was not enough room to get out of the CVD deposition region.

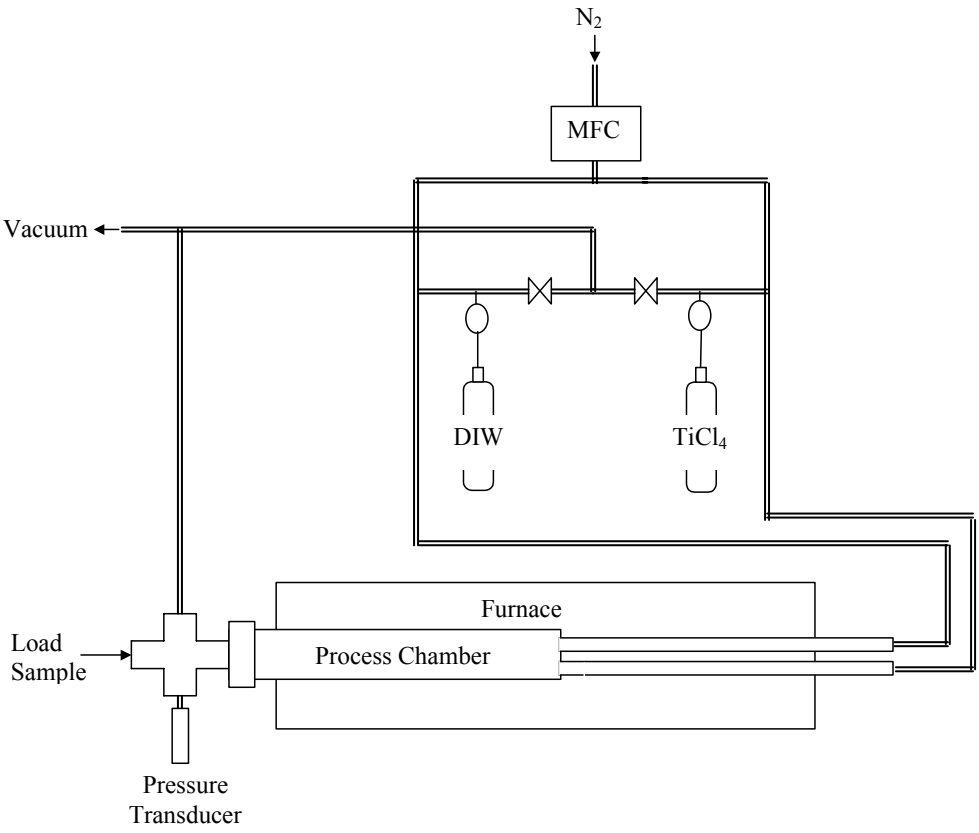

Figure 3.9. Second gas configuration.

The third configuration also introduced the gases into the chamber through separate lines. However, in this configuration the stainless steel gas lines entered through a flange connected to the end of the quartz process tube thereby increasing the length of the tube available for deposition. The region of CVD growth where gas enters the tube stretches for approximately 6 inches. The initial SS configuration had the gas inlets pointing down towards the bottom of the tube, thus creating turbulence. While the flow pattern in the furnace is unknown, we suspect a possible dead space where the precursors can collect and react with the next pulse.

When the system was first converted to the SS gas inlet configuration, there was a problem with samples being blown out of position during the deposition run. Some samples were even blown all the way to the end of the process chamber, a distance of approximately 12". We believe the displacement of the samples was caused by the high pressure during the water pulse, which was more than double the chamber pressure. Consequently, needle valves were added to both sources in order to constrict the precursor flow. Also, the gas inlet tubes were aligned parallel to the process tube, thus reducing the turbulence at the gas inlet.

After these system modifications clogging and substrate displacement was no longer an issue. However, we noticed a problem with the growth rate consistency of films grown at temperatures below 200^{o}C. A flange was added to the end of the process tube with an additional N_2 line. The continuous flow of the N_2 line purged the dead-space behind the gas inlets, thus removing any collected gases that may react with the next pulse. The third and final configuration is shown in the drawing of the ALD system seen previously in Figure 3.6(b).

3.3 ALD Deposition Parameters

3.3.1 Thin Film Deposition

Before film growth the substrates were cleaned using a typical organic solvent wash cycle of acetone, ethanol, and DI water. Samples were dried with N_2 gas after the final DIW rinse, then baked at 100^{o}C for 10 minutes prior to loading into the ALD furnace tube.

The ALD films were deposited through the sequential pulse and purge sequence of H_2O and $TiCl_4$. As mentioned in the literature review for titania grown by ALD, most groups begin the ALD cycle with the $TiCl_4$ pulse instead of the H_2O pulse. However, our program was written to start with the water pulse, which should not have any effect on the film growth process. A typical run consisted of a 1 s H_2O pulse, 2 s N_2 purge, 2 s $TiCl_4$ pulse, and 2 s N_2 purge as illustrated in Figure 3.10. The program would repeat this sequence of conditions for a specified number of cycles; typically 500 – 4000 pulse/purge cycles. The solenoid valve pulse/purge timing was controlled through a LabVIEW graphical interface (Figure 3.11).

The furnace was heated in an uncontrolled ramp to the deposition temperature, at a rate of approximately 10°C/min. At the end of the pulse/purge sequence the furnace was cooled down to room temperature as fast as the furnace would allow. A more detailed description of the ALD process is included in Appendix B.

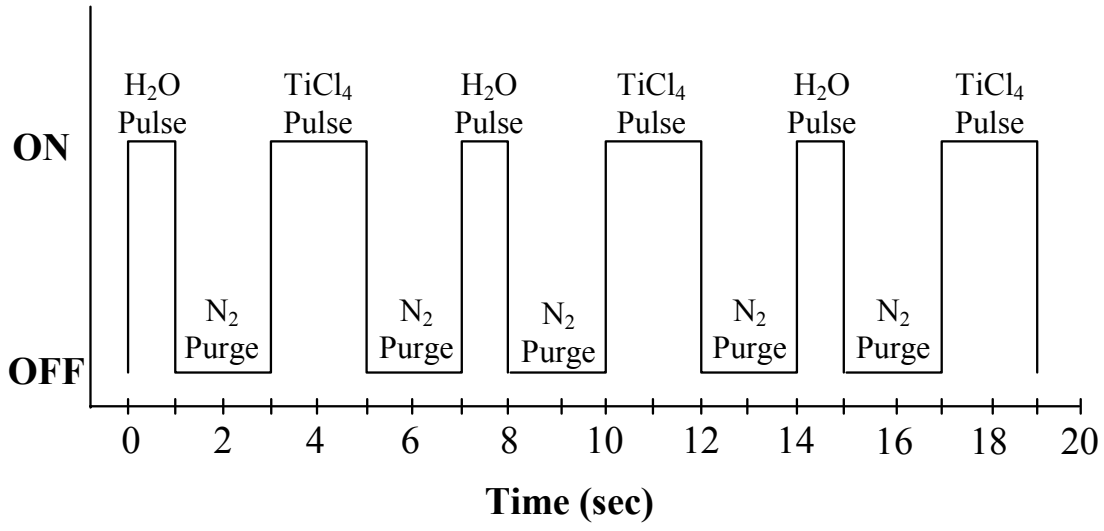

Figure 3.10. ALD Pulse/Purge Sequence

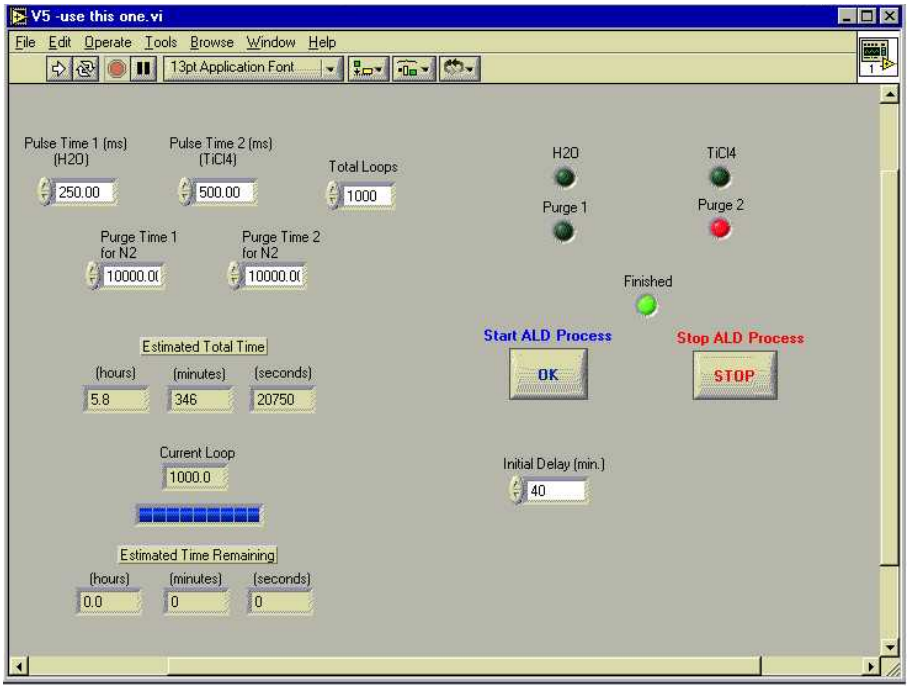

Figure 3.11 LabVIEW ALD program

3.3.2 Opal Infiltration

The infiltration of opal structures is far more complex than the planar deposition of thin films for several reasons. First, the surface area of the opal is much larger than that of a planar substrate. The surface area, *S*, of a 2cm x 2cm opal film that is 10μm thick is given by:

$$S = 17.76 \times 10^4 / d \text{ cm}^2, \tag{3.1}$$

where *d* is the sphere diameter in nm. See Appendix C for a detailed derivation of Equation 3.1. For an opal made with 400nm diameter silica spheres, the surface area of the film is 444 cm^2, which is 111 times greater than the planar area. Therefore, it will take a much larger precursor dose to saturate the surface of the opal film as compared to a planar substrate. Second, the films must be smooth and conformal in order to achieve the

maximum filling fraction. This requires the deposition of films at low temperatures, since they are typically smoother than those deposited at higher temperatures. Finally, the precursors must have enough time to diffuse into the voids of the opal structure. This requirement indicates a need for longer pulse and purge lengths.

The desired film thickness, t, for maximum opal filling fraction is given by:

$$t = 7.75\%\ d = 0.0775\ d. \tag{3.2}$$

As shown in Appendix D, this is the thickness where the infiltrated films will begin to touch inside the tetrahedral opal voids. Consequently, the number of cycles for each opal run was chosen based on the thin film growth rate needed to achieve the desired film thickness.

3.4 Heat Treatment

Two heat treatment studies were performed on ALD titania films in order to convert the films to the rutile structure. In the first study, amorphous films were heat treated at temperatures between 600^{o}C and 1100^{o}C as illustrated in Figure 3.12. The sample was held at the anneal temperature for 8 hours before ramping to the next anneal temperature. Therefore, the same films were heat treated for a total of 48 hours.

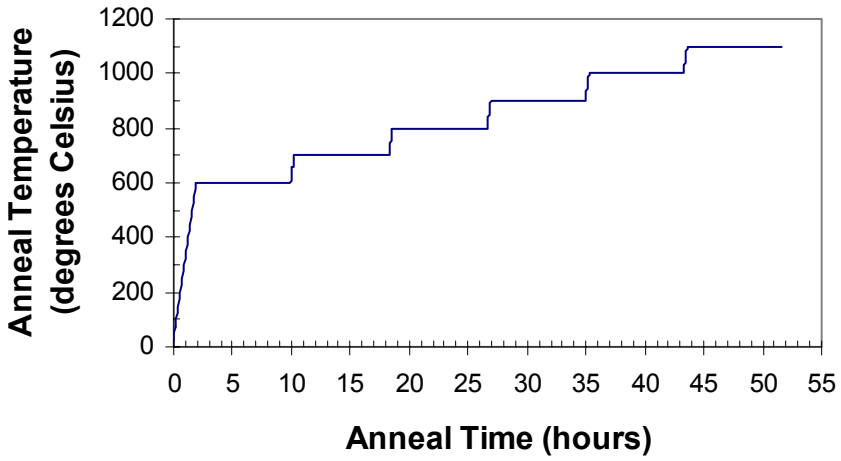

Figure 3.12 Conditions for first heat treatment study.

The second study was a more systematic thermal treatment of the films at one temperature in 6 hour increments. As shown in Figure 3.13, films were heat treated at 700, 800, 900, 1000, and 1100°C. Amorphous, anatase, and anatase-rutile mixed films were annealed in the second heat treatment study.

All ALD thin films were annealed in an air atmosphere using a Keith furnace with a ramp rate of 10°C/min.

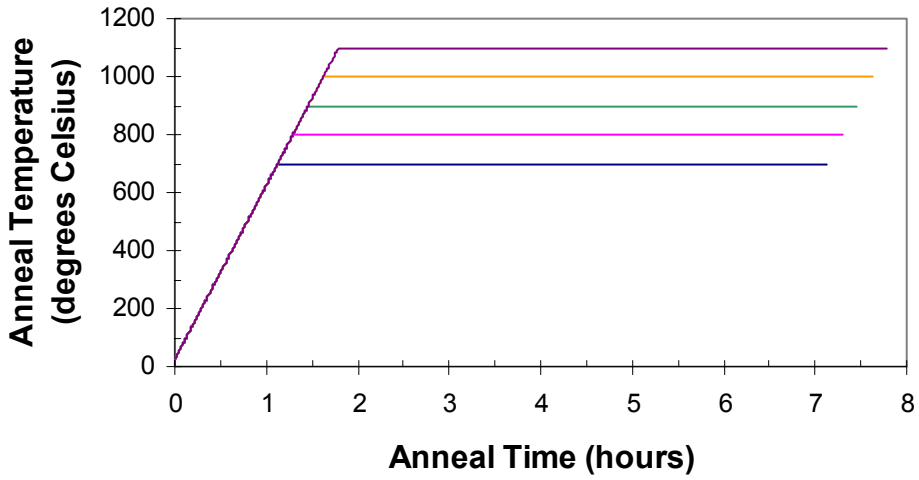

Figure 3.13 Conditions for second heat treatment study.

3.5 Characterization Methods

3.5.1 X-ray Diffraction (XRD)

The crystal structure of the deposited films was determined using a Philips PW 1800 X-Ray Diffractometer with Cu Kα radiation, α_1 = 1.54056Å. Samples were scanned from 20 to 60° 2θ with a step size of 0.02°. XRD patterns were compared with powder diffraction files from the JCPDS-International Center for Diffraction Data in order to determine the crystalline phases present. Samples on (100) silicon were slightly tilted from the horizontal position in order to avoid the appearance of a large silicon peak at approximately 33°. Tilting of the sample resulted in weaker intensity of the XRD peaks, however the relative peak intensities did not change.

The percentage of anatase and rutile phase was calculated for samples with mixed phases using Spurr and Myer's formula:[63]

$$x_A = \frac{w_A}{w_A + w_R} = \frac{1}{1 + \left(\frac{1}{k}\right)\frac{I_R}{I_A}} = \frac{1}{1 + 1.26\left(\frac{I_R}{I_A}\right)} \tag{3.3}$$

where x_A is the weight fraction of anatase present, I_R is the intensity of the strongest rutile peak, and I_A is the intensity of the strongest anatase peak. A k value of 0.79 is used except when x_A is less than 20 percent. A k value of 0.68 should be used for lower anatase weight fraction mixtures. The weight percentage of the anatase phase in mixed amorphous-anatase phase films could not be determined from the x-ray data alone.

3.5.2 Scanning Electron Microscopy (SEM)

Material composition was confirmed using a Hitachi S800 Field Emission Gun (FEG) SEM. The SEM is equipped with an energy dispersive spectrometer (EDS) detector for determining the relative chemical composition. The LEO 1530 thermally-assisted FEG SEM was used to determine conformality of ALD films and ALD penetration depth in opal structures. The LEO was also used to estimate the thickness of planar thin films as an accuracy check for the optical measurements.

Infiltrated opals were milled with a Gatan Dual Ion Mill (Model 600) in order to see inside the opal grains. The ion beam was masked with a 3mm Cu foil containing a 200μm by 1mm slot aperture. The inverted opals were milled for 4 hours at a beam voltage of 4 kV. The beam was tilted at an angle of 45^{o} relative to the sample. Tilting the sample inside the SEM allowed us to identify regions in the grains that were not fully penetrated. The penetration depth was estimated from the SEM pictures.

3.5.3 Spectral Reflectance

A Filmetrics F-20 UV/VIS Spectral Reflectometer was used to measure the thickness and optical constants of the as-deposited and heat treated titania thin films. The F-20 can measure a minimum film thickness of 20 nm. The reflectance was measured at normal incidence for a wavelength range of 220 to 850 nm and then fitted to known dispersion models. The best fit was obtained from the Cauchy model and a Filmetric specified "Amorphous" model. All index and extinction coefficient values were reported at a wavelength of 632.8 nm.

Some of the better-known dispersion models are Cauchy, Sellmeier, Lorentz, and Drude. The Drude model is typically for metals where the dielectric function is governed by free carriers. However, all of the other models can be applicable to transparent insulating films.

The Cauchy model is an empirical set of equations, which assumes a transparent insulator with little to no roughness. The Cauchy model is written as follows:

$$n(\lambda) = A_n + \frac{B_n}{\lambda^2} + \frac{C_n}{\lambda^4} + \ldots$$
$$k(\lambda) = A_k + \frac{B_k}{\lambda^2} + \frac{C_k}{\lambda^4} + \ldots \tag{3.4}$$

where A_n, B_n, C_n, A_k, B_k, and C_k are the six fitting parameters and the wavelengths are expressed in microns.[65]

The Sellmeir relation is a generalization of the Cauchy equations used for transparent materials and some semiconductors. It is expressed by the following equations:

$$n(\lambda) = \left(A_n + \frac{B_n \lambda^2}{\left(\lambda^2 - C_n^2\right)} \right)^{1/2}$$
$$k(\lambda) = \left[n(\lambda) \left(B_1 \lambda + \frac{B_2}{\lambda} + \frac{B_3}{\lambda^3} \right) \right]^{-1} \tag{3.5}$$

where A_n, B_n, C_n, B_1, B_2, and B_3 are the fitting parameters.

The spectral reflectometer has a manufacturer specified "amorphous model" that was also a good fit for most samples measured. Unfortunately, the dispersion model is proprietary so that the exact relation is unknown.

The Lorentz oscillator is consistent with the Kramers-Kronig relations. The model is described by the equations:

$$n^2 - k^2 = 1 + \frac{A\lambda^2}{\lambda^2 - \lambda_0^2 + g\lambda^2 / \left(\lambda^2 - \lambda_0^2\right)}$$
$$2nk = \frac{A\sqrt{g}\lambda^3}{\left(\lambda^2 - \lambda_0^2\right)^2 + g\lambda^2} \tag{3.6}$$

where λ_0 is the oscillator central wavelength, A is the oscillator strength, and g the damping factor.

Unfortunately, spectral reflectance of the films did not yield reliable results. Historically, measurement of TiO_2 using spectral reflectometry has provided inaccurate results for the optical constants.

3.5.4 Ellipsometry

Since the spectral reflectometer did not yield consistent values for the optical constants, the refractive index and extinction coefficient for a few as-deposited samples was also measured using ellipsometry. The VB-250 VASE from J.A. Woollam was used for measuring the refractive index and extinction coefficient of films.

Samples were scanned at wavelengths from 200 to 1100 nm. The samples were strongly absorbing at ~300 nm so the Cauchy model was not useful at lower wavelengths. However, the films were not absorbing at wavelengths above 800 nm. Therefore, the Cauchy model was fitted to the data at wavelengths from 800 to 1100 nm based on the thickness guess and Cauchy parameters A_n, B_n, and C_n. The values for n and k were determined from the Cauchy model, and then used as the initial guess for a point-to-point

model of the data over the entire wavelength range. All optical constant values obtained using ellipsometry were reported at 630 nm.

Another method for determining the optical constants of thin films is known as the envelope method or Swanepoel's method.[66] Swanepoel's method determines the thickness, refractive index, and extinction coefficient by constructing an envelope around transmission fringes. Curves are drawn corresponding with the maxima and minima of the transmission fringes. The optical constants and thickness values are then calculated by using values from the maxima and minima curves in specified equations. However, the envelope method is only useful for films thick enough to have several transmission fringes. Thin films result in only a few transmission fringes, therefore the accuracy of Swanepoel's method for the films produced in this research project is questionable. The envelope method is also limited to films deposited at lower temperatures, because the transmission spectrum of films deposited or annealed at higher temperatures tends to lose its order. Despite these issues, the thickness and optical constants of thicker films were manually calculated using Swanepoel's method and compared to results from the spectral reflectometer and ellipsometer.

3.5.5 Atomic Force Microscopy (AFM)

A Topometrix Autoprobe CP AFM was used to measure the surface roughness of the ALD films deposited at various temperatures. AFM also gave valuable insight into the formation of the crystal structure. The topography images were acquired in the contact mode using mounted microlever type cantilevers.

3.5.6 Non-Normal Incidence Reflectivity

A Beckman DU640 Spectrophotometer was used to measure the reflectivity of opals at 15° incidence and transmission at normal incidence. The reflectivity measurements were used to determine the location of the opal band gap before and after titania infiltration. The wavelength, λ, of the (111) Bragg peak can be calculated from Bragg's law for optical diffraction:

$$\lambda = 2d_{hkl}\sqrt{\varepsilon_{eff} - \sin^2\theta} \tag{3.7}$$

where d_{hkl} is the distance between (111) planes, ε_{eff} is the effective dielectric constant of the material, and θ is the angle of incidence of the incident EM waves. The interplanar spacing is related to the lattice constant, a, and sphere diameter, d, by the equation:

$$\begin{aligned} d_{hkl} &= \frac{a}{\sqrt{h^2+k^2+l^2}} = \frac{2d}{\sqrt{2}\cdot\sqrt{h^2+k^2+l^2}} \\ \therefore d_{111} &= \frac{2d}{\sqrt{2}\cdot\sqrt{1^2+1^2+1^2}} = \frac{2d}{\sqrt{6}} \end{aligned} \tag{3.8}$$

where h, k, and l are the Miller indices for the plane. Therefore, Equation 3.7 becomes:

$$\lambda = 2\left(\frac{2d}{\sqrt{6}}\right)\sqrt{\varepsilon_{eff} - \sin^2\theta} = 1.63d\sqrt{\varepsilon_{eff} - \sin^2\theta} \tag{3.9}$$

Equation 3.7 is derived from a combination of Snell's law and Bragg's law. Bragg's law of diffraction assumes the incident light will not change direction upon entering the crystal. Therefore, the incident angle is equal to the diffracted angle. While this is true for x-rays, it is not true for electromagnetic waves with wavelengths in the

visible regime. Consequently, Snell's law must be used to account for the refraction of light when entering a material of higher index.[67]

The effective dielectric constant is calculated from the volume fraction, *f*, of the high index material as follows:

$$\varepsilon_{eff} = f\varepsilon_a + (1-f)\varepsilon_b \tag{3.10}$$

where ε_a and ε_b are the dielectric constants of the high and low index materials, respectively. Since the synthetic opal consists of close packed spheres of silica in air, the effective refractive index is easy to calculate. FCC packing results in a volume fraction of 74%.

Infiltration of the synthetic opal with TiO_2 should result in an increase in the effective dielectric constant, and as a consequence the wavelength of the Bragg peak should also increase. Since the TiO_2 fills the interstitial voids between the silica spheres, the maximum volume fraction of TiO_2 is 26%. While the exact volume fraction of TiO_2 is unknown, it can be approximated using the following expression for the refractive index of the infiltrated opal:

$$\varepsilon_{eff} = 0.74\varepsilon_{SiO_2} + (0.26-f)\varepsilon_{air} + f\varepsilon_{TiO_2} \tag{3.11}$$

The wavelength dependent dielectric constant was used in the calculations of filling fraction reported in Chapter 4.

Etching of the SiO_2 spheres resulted in a titania inverse opal consisting of air in a thin TiO_2 matrix. Consequently, the peak reflectivity wavelength will shift to a shorter

wavelength after etching, that is however, still longer than the reflectivity wavelength of the original SiO_2 opal.

3.5.7 X-Ray Photoelectron Spectroscopy (XPS)

XPS was used to determine the surface composition of the ALD films. XPS was performed using a SSX-100 ESCA spectrometer manufactured by Surface Science Instruments. Monochromatized Al Kα radiation with an energy of 1486.6 eV was used to irradiate the sample with a spot size of 800 μm. Survey scans were taken from 0 to 1100 eV with a step size of 1 eV. Detailed scans of the oxygen and titanium peaks were taken at step sizes of 0.1 eV in order to determine the type of bond.

CHAPTER 4

RESULTS AND DISCUSSION

4.1 ALD Titania Thin Film Characterization

4.1.1 Growth Mechanisms

ALD growth is typically characterized using film growth experiments and in situ reaction mechanism studies, however our custom built system does not have any built in measurement equipment so we relied on ex situ methods alone. Film growth studies include the examination of growth rates as well as film properties such as crystal structure, composition, and morphology. The effects of substrate temperature, reactant pulse length, and N_2 purge length on the growth rate were investigated as part of the film growth experiments.

ALD runs were performed using the parameters described previously in Section 3.3.1. For thin film runs the length of the water pulse was always set at half that of the $TiCl_4$ pulse length. The effect of pulse length was a combined effect of changing the H_2O and $TiCl_4$ pulse by the same amount. The purge lengths for both precursors were also set to the same length. See Appendix E for a complete list of all runs performed.

There was considerable variation in the thickness values calculated using spectral reflectance and ellipsometry, especially at higher deposition temperatures. Table 4.1 shows the values calculated using the two optical techniques as compared to the measured value from the SEM images. All growth rate values were calculated from the thickness of the film as measured by spectral reflectance (and fitted to the Cauchy model

as described in Equation 3.4) divided by the number of cycles. Spectral reflectance was chosen based on it's ease of use more than it's accuracy.

Table 4.1. Thickness values obtained using different characterization methods for varying ALD deposition temperatures.

Deposition Temperature	**Ellipsometry**	**Spectral Reflectance**	**SEM**
(^{o}C)	**(nm)**		
100	72	72	74
300	96	106	119
400	87	102	
500	77	97	
600	94	125	91

Effect of Substrate Temperature on Growth Rate:

As shown in Figure 4.1 three different growth regions can be identified from the study of growth rate versus substrate temperature. In the first region, low temperature deposition between 100 and 200^{o}C, the growth is characterized by high growth rates. The growth rate stabilized in the second growth region that spans from 200 to ~500^{o}C. Finally, the growth rate dropped off at deposition temperatures above 500^{o}C. The growth regions above 200ºC correspond with the development of the anatase and rutile crystal structures, which will be discussed further in Section 4.1.2. In general, the growth rate decreased with increasing temperature, which is consistent with growth rate relations reported by Aarik *et al.*[52]

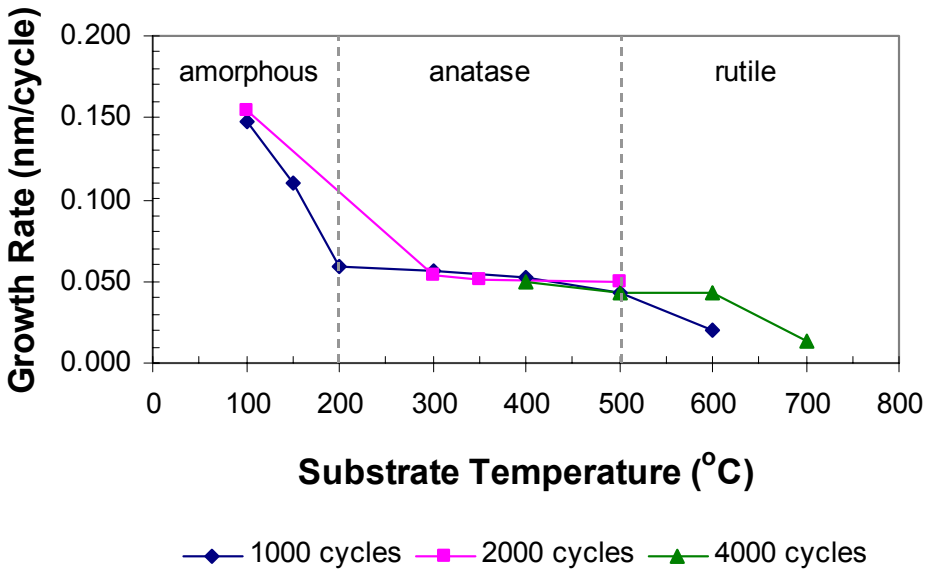

Figure 4.1. Growth rate versus temperature for TiO_2 samples grown with a 0.5s H_20 pulse, 1s $TiCl_4$ pulse, and a 4s purge for 1000, 2000, and 4000 cycles.

The high growth rate for the sample grown at 100°C is attributed to a combination of ALD and CVD growth. At lower temperatures, the reactants do not desorb from the furnace tube walls before the next reactant pulse. Thus, the presence of both reactants in the tube results in continuous gas phase CVD reactions and in a much thicker film. However, the thickness of the film is limited by the slower reaction rate at low temperatures. Inconsistent growth rates were found at temperatures between 100 and 200°C, which will be discussed shortly.

As shown in Figure 4.1 the growth rate plateaus, and is fairly stable in the temperature range from 200°C to 500°C. This is the temperature range where self-limited ALD growth takes place. The length of the pulse and purge time has very little effect on the growth rate in the pure ALD regime. Pure ALD growth is possible in the other

growth regions, however, the selection of pulse and purge lengths are more critical in obtaining quality films.

A rapid drop in the growth rate occurs at temperatures above 500^{o}C most likely due to precursor desorption. Consistent film quality is a challenge at higher substrate temperatures.

The film thickness was uniform as long as the substrate was always the same distance from the gas inlet tubes.

Effect of Pulse and Purge Length on Growth Rate:

The growth rate versus pulse and purge length was also investigated for each of the growth regions described above. The growth rate variation with $TiCl_4$ pulse length also showed temperature dependence as seen in Figure 4.2. As expected, the growth is self-limited at deposition temperatures of 300 and 600^{o}C, however the growth rate at 100^{o}C resembles CVD-like growth of multiple layers.

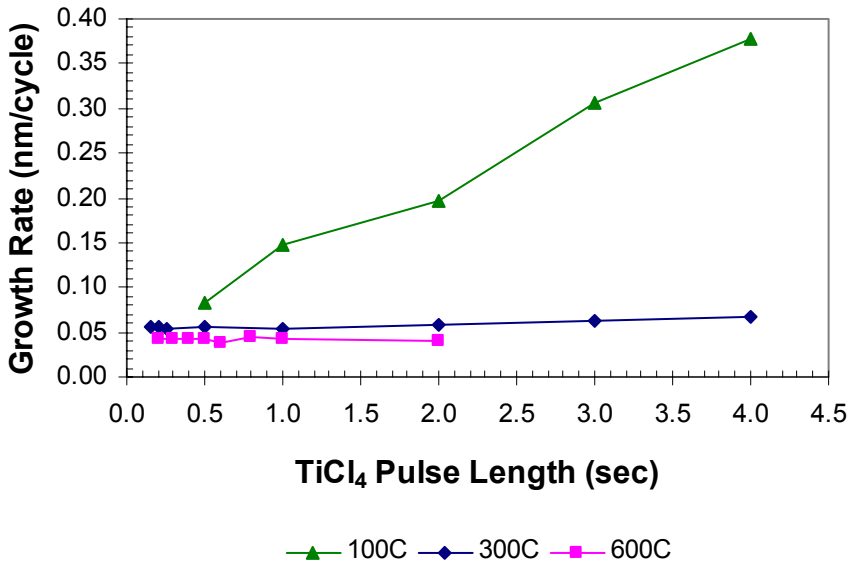

Figure 4.2. Comparison of growth rate versus $TiCl_4$ pulse length for samples grown at 100°C, 300°C, and 600°C. 100°C samples were grown for 1000 cycles with a 4s purge. Samples grown at 300°C have a 6s purge and were grown for 2000 cycles. 600°C samples were purged for 2s and grown for 3000 cycles.

The pulse and purge time has a significant effect on the growth rate for films grown at temperatures ≤200°C. Before the addition of the N_2 purge flange, a CVD-like growth rate occurred for longer pulses even when the purge length was doubled to 8 seconds as shown in Figure 4.3. We established that the precursor gases were collecting in the dead-space behind the gas inlet tubes, and then reacting with the next pulse thereby producing gas phase reactions resulting in thick films. The addition of a continuous N_2 purge line at the end of the process chamber resulted in a growth rate curve that is more typical of the ALD process, however the growth rate is still higher than the growth rate at higher deposition temperatures. The dead-space was not an issue at higher deposition temperatures due to the increased rate of reaction. It was not until the addition of the extra N_2 purge that the growth rate showed saturation for pulse lengths between 2 and 6

sec. The growth rate begins to increase again at pulse lengths of 7 sec and above, which again is most likely due to an insufficiently long purge length.

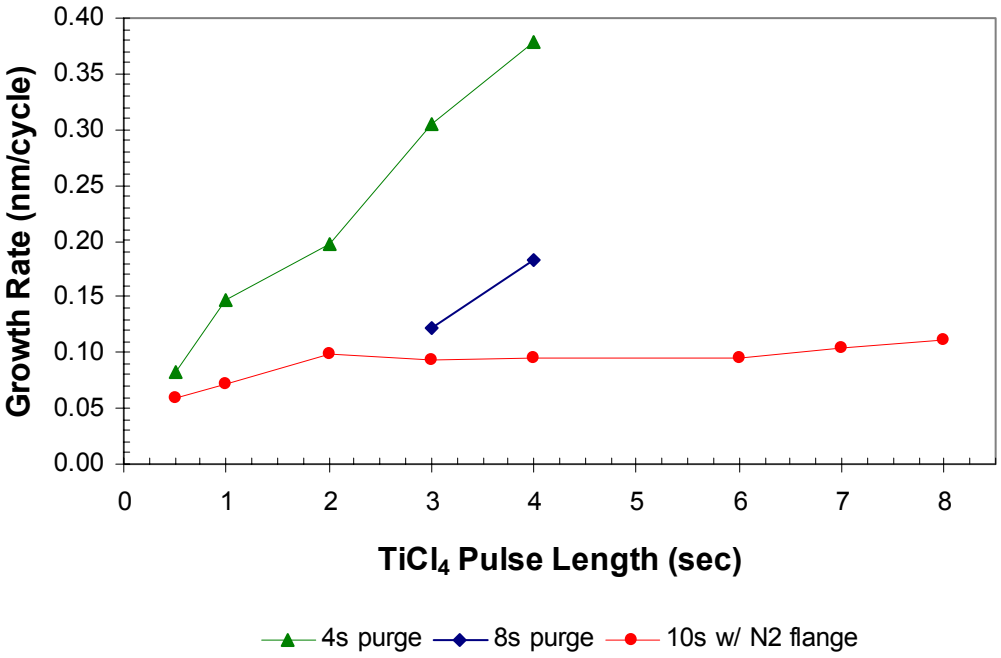

Figure 4.3. Growth rate versus $TiCl_4$ pulse length for samples grown at 100°C. Samples were grown for 1000 cycles with a 4s purge, 500 cycles with a 8s purge, and 1000 cycles with a 10s purge (plus continuous N_2 flange purge).

The purge length for low temperature runs was more critical than for higher temperature runs. See Figure 4.4 for the effect of purge length on growth rate for films deposited at a substrate temperature of 100°C. Self-limited growth is possible without the N_2 flange if the purge length is long enough, however the longer purge length results in a longer cycle time. While the addition of the N_2 flange greatly reduced the effects of pulse and purge length on the growth rate, the growth rates at 100°C are still more variable than those at higher temperatures.

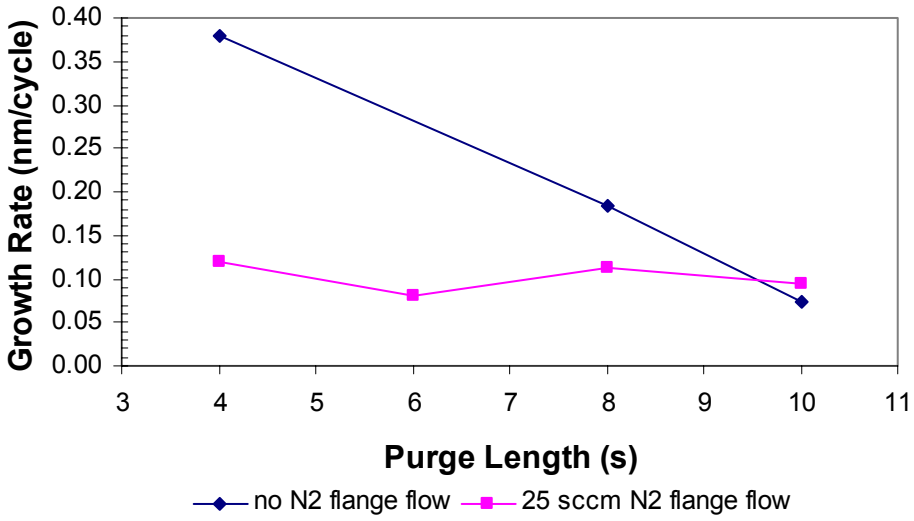

Figure 4.4. Growth rate versus purge length for films grown at 100°C for 1000 cycles with and without the N_2 flange. Pulse times were 2s for the H_2O pulse and 4s for the $TiCl_4$ pulse.

As shown in Figure 4.5 the growth rate at 300°C was constant for pulse lengths greater than 150 ms. We were not able to determine the saturation point for our system, because we did not want to switch the solenoid valves any faster than 150 ms. Other groups have reported saturation at a pulse length of 200 ms when $TiCl_4$ is the precursor.[51] The 300°C growth rate is constant for $TiCl_4$ pulse lengths up to1 sec. At a pulse length of 2 s the growth rate begins to increase again. This is attributed to multilayer CVD reactions, which could be prevented if the purge length was increased. The data shown in Figure 4.5 was taken before the addition of the N_2 flange, therefore the increase in growth rate at longer pulse lengths may be eliminated by the extra purge from the continuous N_2 flow from the flange.

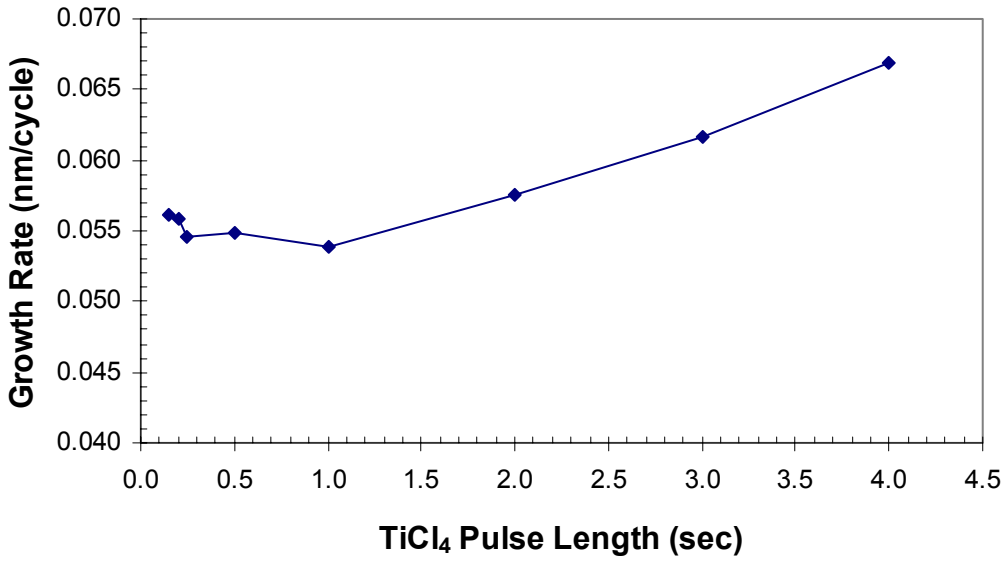

Figure 4.5. Growth rate versus $TiCl_4$ pulse length for samples grown at 300°C before the addition of the N_2 flange. Samples were grown for 2000 cycles with a 6s purge.

As shown in Figure 4.6, the purge length had little to no effect on the growth rate for films grown in the self-limited growth region at 300°C. The growth rate for the 2 s $TiCl_4$ pulse was stable for purge lengths as high as 4 times the pulse length. Therefore, the chemisorbed layer is stable and stays attached to the surface at any purge length. The 1 sec pulse length showed a slight decrease in the growth rate with increased purge length. Therefore, there is some desorption of the precursor for longer purge lengths.

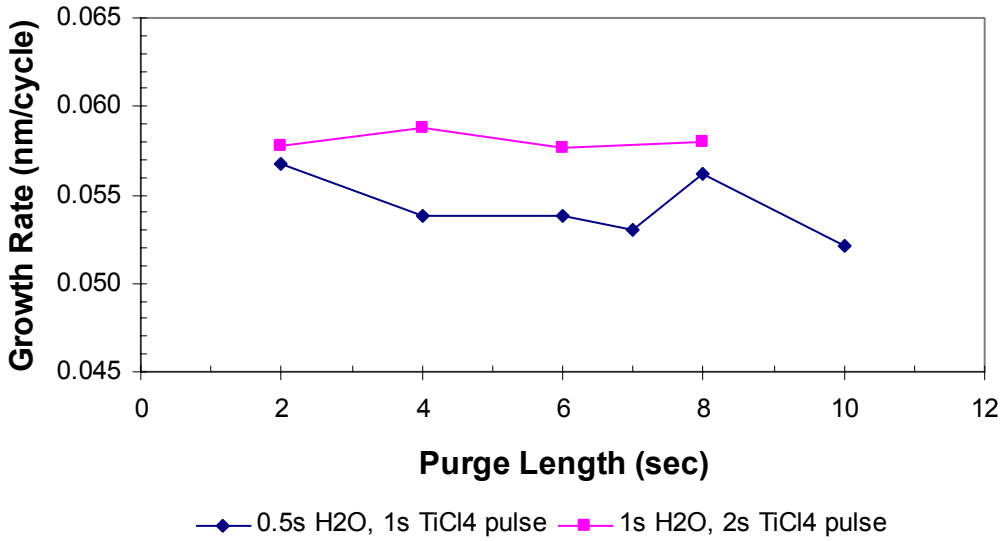

Figure 4.6. Growth rate versus purge length for samples grown at 300°C before the addition of the N_2 flange. Sample were grown for 2000 cycles.

Growth rate versus pulse length for high substrate temperatures also showed saturation in the growth rate as shown in Figure 4.7. The growth rate at 600°C is stable for longer pulse lengths than the growth at 300°C. The increase in growth rate due to CVD is not seen at higher temperatures, probably due to the higher reactivity of the precursors at that temperature. Despite the uniform growth rate, samples grown at 600°C do not yield consistently uniform films. Some films are uniform, while others have a gradient in the growth rate at the edges of the samples or no edge deposition at all. The lack of edge deposition could indicate that there is not enough material to cover the entire substrate, however the edge effects were observed for both short and long pulse times.

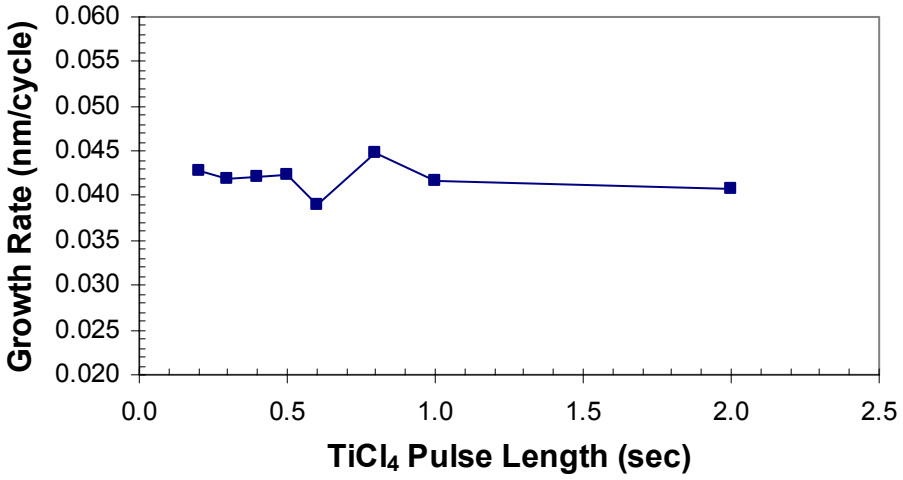

Figure 4.7. Growth rate versus $TiCl_4$ pulse length for samples grown at a substrate temperature of 600°C before the addition of the N_2 flange. Samples were purged for 2s and grown for 3000 cycles.

The growth rate versus purge length at growth temperatures of 600°C was not investigated. However, due to the high reactivity of the precursors at higher temperatures, long purge lengths are probably not necessary. Other groups have reported little effect of the purge length at 600°C.[49]

4.1.2 Crystal Structure

X-ray diffraction revealed the development of the anatase crystal structure at temperatures as low as 200°C. The transformation from the anatase crystalline structure into the rutile structure did not occur until temperatures of at least 400°C. Films still had a mixture of the rutile and anatase phases even at deposition temperatures of 600°C. The weight percentage of rutile phase for the anatase-rutile mixed phase samples at 600°C

varied from 29.0 to 78.2%. The reason for this variability could not be determined. A pure rutile film was grown at a deposition temperature of 700°C once, however the growth could not be duplicated beyond that one time. The high density TiO_2-II polymorph, as reported by Aarik *et al.*,[55-56] was not observed for any deposition conditions or temperatures. See Figure 4.8 for XRD spectrums of samples grown at various deposition temperatures.

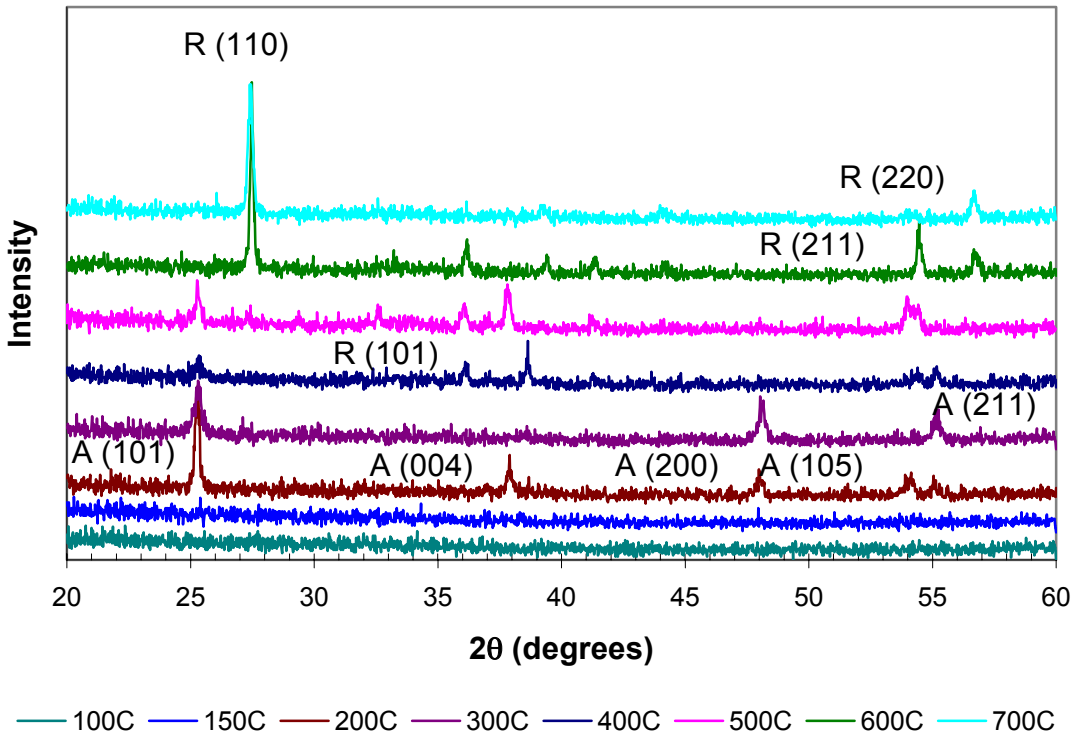

Figure 4.8. XRD spectra for ALD films grown at varying substrate temperatures.

The crystallinity of the films was not always consistent with deposition temperature. Some films showed very weak diffraction patterns. It has been reported that crystallization will not occur until a certain film thickness is reached.[52] However, even some of the relatively thick films had weak XRD patterns.

4.1.3 Film Composition and Roughness

SEM pictures of the ALD films, as shown in Figure 4.9, revealed the appearance of crystal grain structure at 300°C that corresponded with the formation of the anatase phase as shown by XRD. The grain structure was more defined at a deposition temperature of 600°C. The combination of large (300 nm) and small (50 nm) grains at 600°C was probably due to the presence of both the anatase and rutile phases. The sample was 65% rutile. The XRD pattern of the sample pictured in Figure 4.9a showed the existence of an "amorphous hump" in addition to diffraction peaks corresponding with anatase structure, which could explain why the grains are not as well-defined as those in Figure 4.9b.

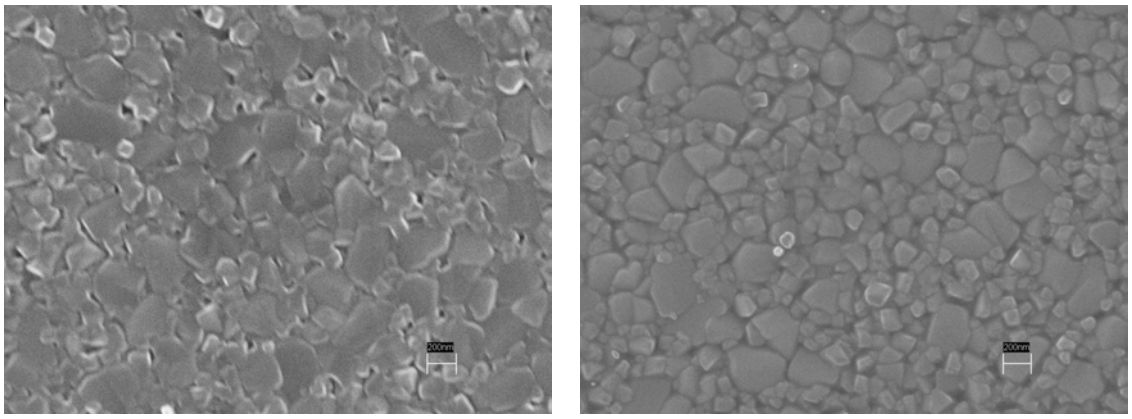

(a) (b)

Figure 4.9. SEM micrographs of ALD films deposited at substrate temperatures of (a) 300°C and (b) 600°C. Scale bar = 200 nm.

The RMS roughness of the deposited films, as measured by AFM, increased as deposition temperature increased. Films deposited at 100°C were relatively smooth. Films became rougher as the crystalline structure developed. See Figure 4.10 for RMS

roughness values and AFM pictures for films deposited at temperatures of 100, 300, and 600^{o}C. The circular area in the middle of the grains deposited at 300^{o}C is a tip artifact, not part of the actual TiO_2 grain structure.

r_{RMS} = 0.2nm

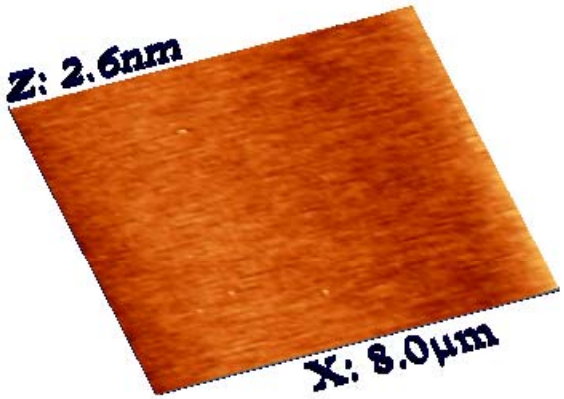

(a)

r_{RMS} = 2.1nm

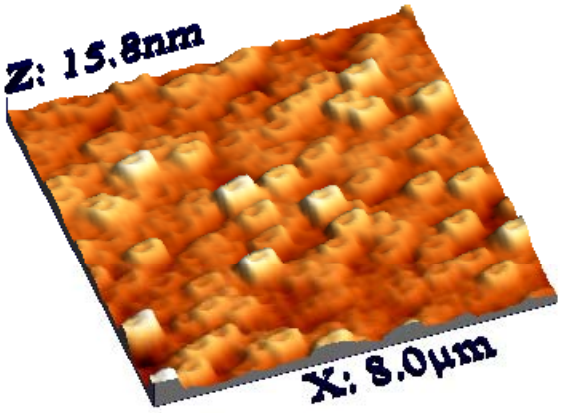

(b)

r_{RMS} = 9.6nm

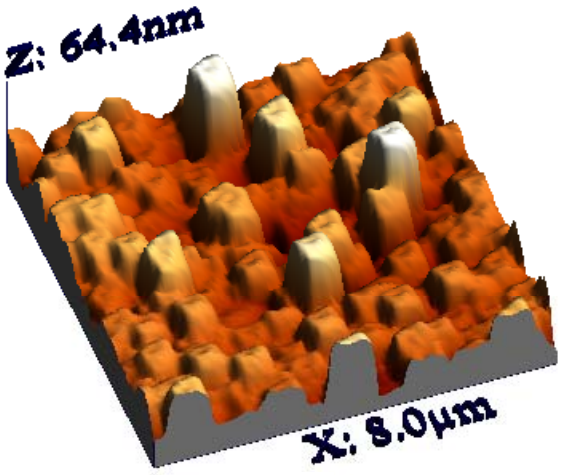

(c)

Figure 4.10. AFM images and roughness values for TiO_2 films grown at (a) 100°C, (b) 300°C, and (c) 600°C.

The ALD films had a small amount of residual chlorine from the $TiCl_4$ source when deposited at low temperatures as shown in the EDS spectrum in Figure 4.11. This residual chlorine is due to incomplete reactions at low temperatures and has been reported by other groups when growing ALD TiO_2 using $TiCl_4$ as a precursor.[51-52] Chlorine was not detected in samples deposited at temperature of 300°C or above.

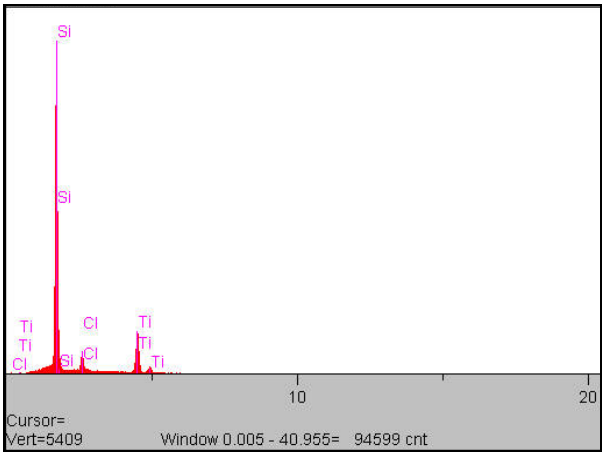

Figure 4.11. EDS spectrum for ALD TiO_2 film deposited at a substrate temperature of 200°C.

XPS was used to determine the stoichiometry of the ALD TiO_2. Survey scans of samples at temperatures between 100°C and 600°C revealed the presence of small amounts of sodium (Na), fluorine (F), phosphorous (P), and carbon (C) in addition to the expected titanium (Ti), oxygen (O), and chlorine (Cl) peaks. The additional peaks, which correspond with elements that are common contaminants found in the air, were not observed in all of the samples. All three contaminants were not found in any one sample. An example of the XPS data obtained in the survey scan is shown in Figure 4.12, which plots data for a sample deposited at 100°C. Chlorine was detected in samples deposited at temperatures of 100 and 600°C. The chlorine content found in films at 600°C is

unexplained, since it was not detected in EDS analysis of the films. The survey scan of another sample deposited at 600°C did not show any chlorine. The presence of chlorine at higher temperatures is an indication of precursor decomposition, however this was not the case for our system because the growth rate would have increased at high temperatures if the precursor was decomposing, since self-limited growth would have been defeated.

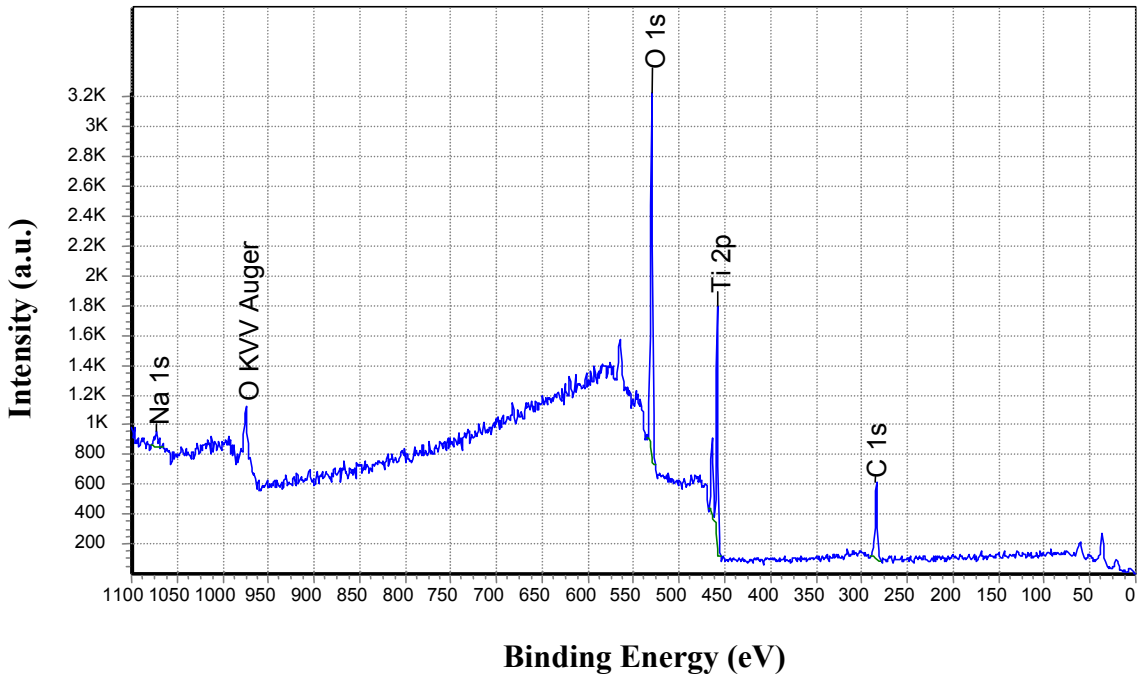

Figure 4.12. Survey scan of a TiO_2 thin film sample deposited at 100°C. Scan step size was 1 eV. Atomic percentages were 52% O, 32% C, 14% Ti, and 2.3% Na.

The survey scan alone was not enough to reveal the bonding characteristics of the constituent elements, thus high resolution scans were performed on the titanium and oxygen peaks. As shown in Figure 4.13, the high-resolution scan of the titanium 2p peak for a sample deposited at 100°C showed a doublet separation between the $2p_{1/2}$ and $2p_{3/2}$ peaks of ~5.7eV, which is indicative of TiO_2 bonding.[68]

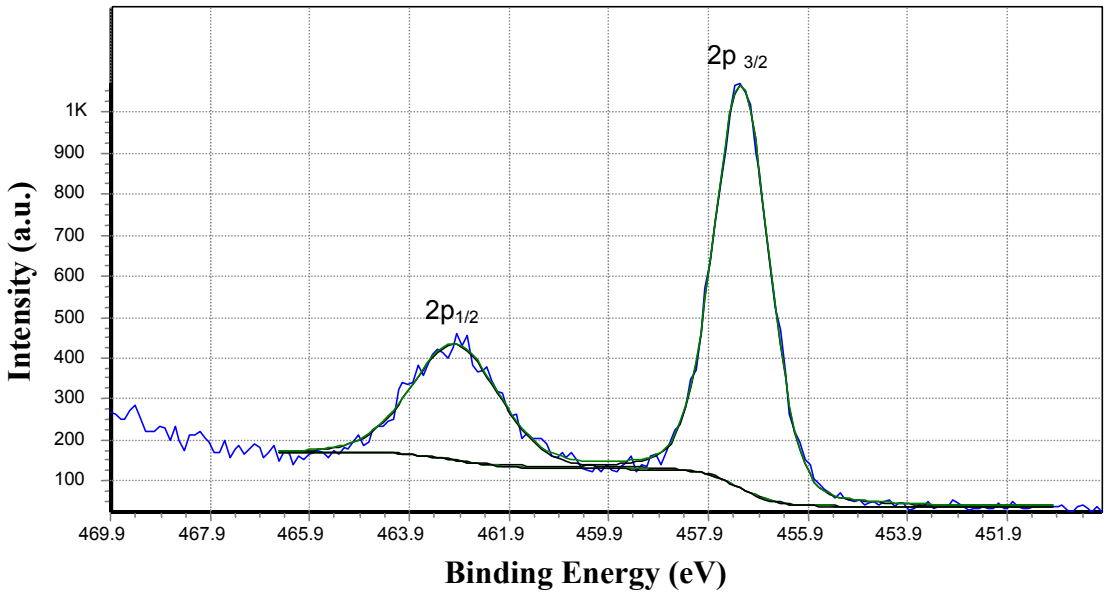

Figure 4.13. High resolution scan of Ti 2p peak from 450 to 470 eV with a step size of 0.1 eV. Pk01= 457.236 eV, Pk02= 462.969 eV, Delta= 5.733 eV. Sample is the same as that used for the survey scan shown in Figure 4.12.

As shown in Figure 4.14 the high-resolution scan of the oxygen 1s peak revealed an asymmetric peak with a wider tail on the high-energy side which indicates the presence of two overlapping peaks. The binding energy of the larger peak is ~530eV, which corresponds with the published binding energy of oxygen in TiO_2. The binding energy of the smaller peak could not be correlated to a single chemical species. Various organic solvents and hydroxyls have binding energies in the 531.7eV range. Unfortunately, the exact nature of the bonding cannot be determined without a high resolution scan of the carbon peak. The two energy peaks are most likely a result of oxygen bonding with TiO_2 and acetone organic solvent. The samples were cleaned with acetone, ethanol, and DIW shortly before being loaded into the XPS system. It is

possible that some residual from the acetone solvent remained on the surface even in the vacuum, although pure ethanol should remove the majority of acetone residues.

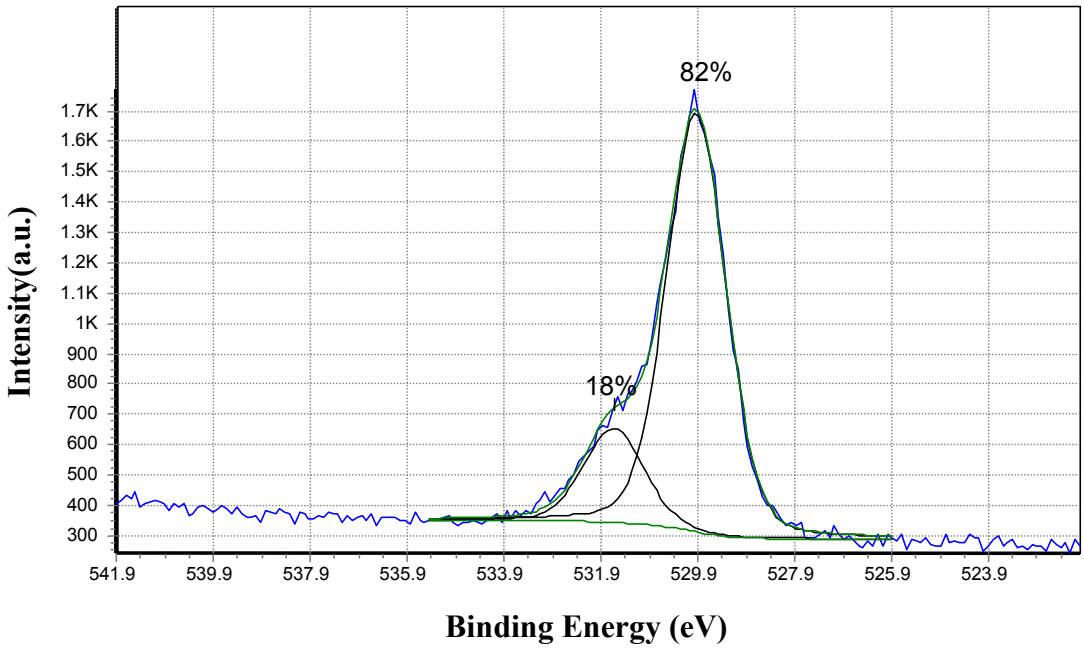

Figure 4.14. High resolution scan of O 1s peak from 522 to 542 eV with a step size of 0.1 eV. Sample is the same as that used for the survey scan shown in Figure 4.12.

Two samples deposited at 300 and 500°C revealed three overlapping oxygen peaks in the high resolution O 1s scan as shown in Figure 4.15. Another scan at 300°C only had two overlapping peaks in the high resolution scan of the oxygen 1s peak. The binding energies associated with the two largest peaks are the same as those observed in the two peak scan described above. The bonding resulting in the third peak is a result of oxygen bonding in water, which has a published value of 533.1eV.

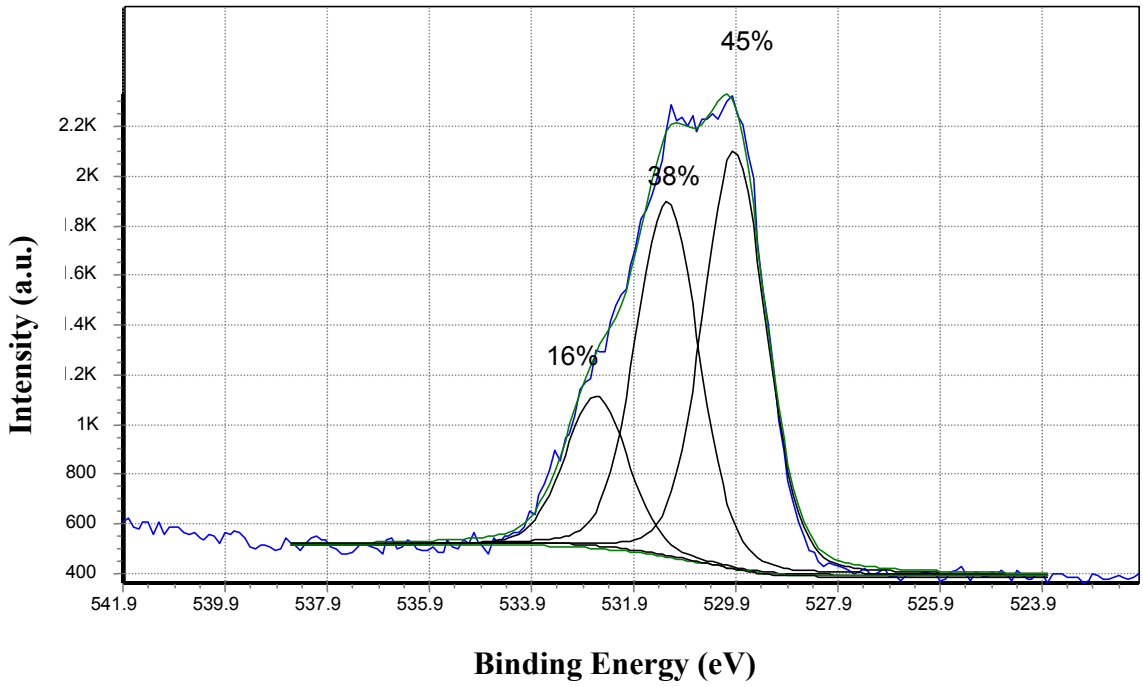

Figure 4.15. High resolution scan of O 1s peak from 522 to 542 eV with a step size of 0.1 eV. Sample was deposited at 500°C.

4.1.4 Optical Properties

The optical constants of the thin films were measured using several different techniques and equipment as described in Section 3.5.3-4. However, data obtained from these methods were inconsistent. The values obtained for the refractive index at deposition temperatures of 100°C were similar for all characterization methods used, however for higher deposition temperatures the values obtained from different methods varied considerably as illustrated in Table 4.2. Ellipsometry yielded the most believable values for the optical constants, therefore the optical data presented in this section were measured using ellipsometry.

Table 4.2. Comparison of methods for determining optical constants of films deposited at 300°C. A film of ~350nm was used for the spectral reflectance and envelope measurements.

Characterization Method	Index of Refraction	Extinction Coefficient
Spectral Reflectance	2.21	0.024
Ellipsometry	2.54	0.049
Envelope Method	2.71	

The index of refraction versus wavelength for samples deposited at temperatures between 100 and 600°C is plotted in Figure 4.16. The index values were not calculated at shorter wavelengths for some of the samples due to the poor fit of the point-by-point model because of the TiO_2 absorption peak. However, the index values calculated at the non-absorbing higher wavelengths should be representative of the true refractive index of the sample at those wavelengths.

The refractive index appears to show a sharp increase at a deposition temperature of 300°C, which corresponds to the onset of the polycrystalline anatase phase. However, there is very little difference in the index value for temperatures between 300 and 600°C. We expected to see a further increase in the refractive index with the conversion to the rutile phase, however the index value dropped at a deposition temperature of 500°C. The index of refraction change with substrate temperature is shown in Figure 4.17. The index values obtained are equivalent to typical values found for the anatase phase.

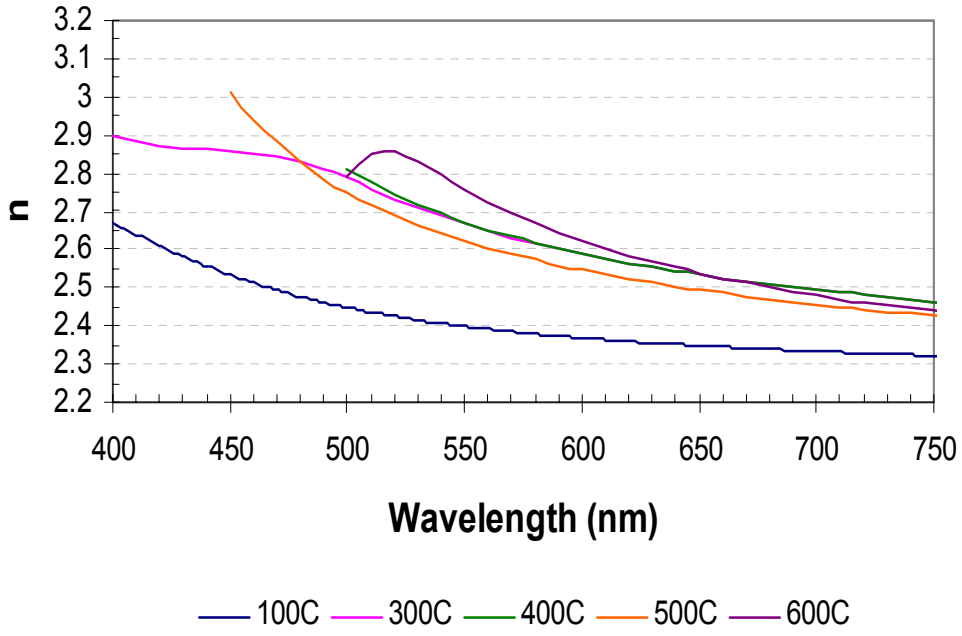

Figure 4.16. Index of refraction versus wavelength for ALD thin film samples deposited at substrate temperatures between 100 and 600°C.

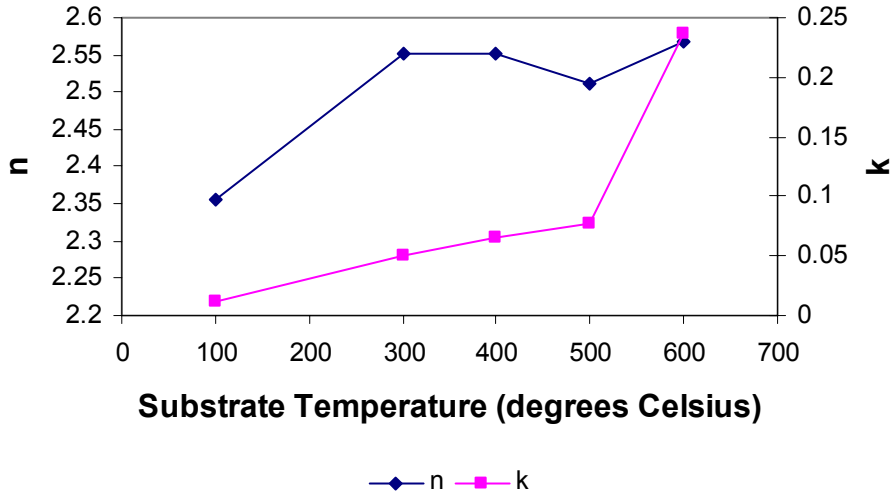

Figure 4.17. Index of refraction and extinction coefficient measured at 630 nm versus substrate temperature for ALD TiO_2 thin films.

4.2 Heat Treatment of Titania Thin Films

Since the refractive index of the as-grown ALD TiO_2 films was less than the required index of 2.8 for a full photonic band gap for the majority of the wavelength range of interest, the conversion to the high index rutile phase was attempted by heat treatment of the as-deposited films at various temperatures and conditions. Recall that two heat treatment studies were performed on ALD titania films in order to convert the films to the rutile structure as described in Section 3.4. In the first study, two amorphous films grown at 100°C were heat treated for 8 hours each at temperatures between 600°C and 1100°C. The temperature was increased by 100°C for each separate heat treatment. The same films were heat treated for a total of 48 hours. The second study was a more systematic thermal treatment of the films at one temperature for increments of 6 hours at a time. Films were heat treated at 700, 800, 900, 1000, or 1100°C. Amorphous, anatase, and anatase-rutile mixed films, grown at 100, 300, and 500 or 600°C, respectively, were annealed in the second heat treatment study.

4.2.1 Changes in Crystal Structure

Thermal annealing was first done on amorphous thin films in an attempt to convert to the rutile phase. Both amorphous films showed anatase peaks after annealing for 8 hours at 600°C. Rutile peaks were not observed until 1100°C, which is considerably higher than the temperature required to grow rutile films directly through ALD. The onset of the rutile phase was significantly higher than the anatase-to-rutile conversion temperatures of 700 to 900°C reported in the literature. While the crystal structure did not change after heat treatment from 600 to 1000 degrees, there were changes in the XRD

patterns as shown in Figure 4.18. The intensity of the anatase peaks increased as the anneal temperature was increased, indicating better crystallinity. The peak in the as deposited film at 33° is due to diffraction from the (100) silicon substrate, which can usually be eliminated by slight tilting of the sample in the x-ray specimen holder. Changes in the film color were also observed.

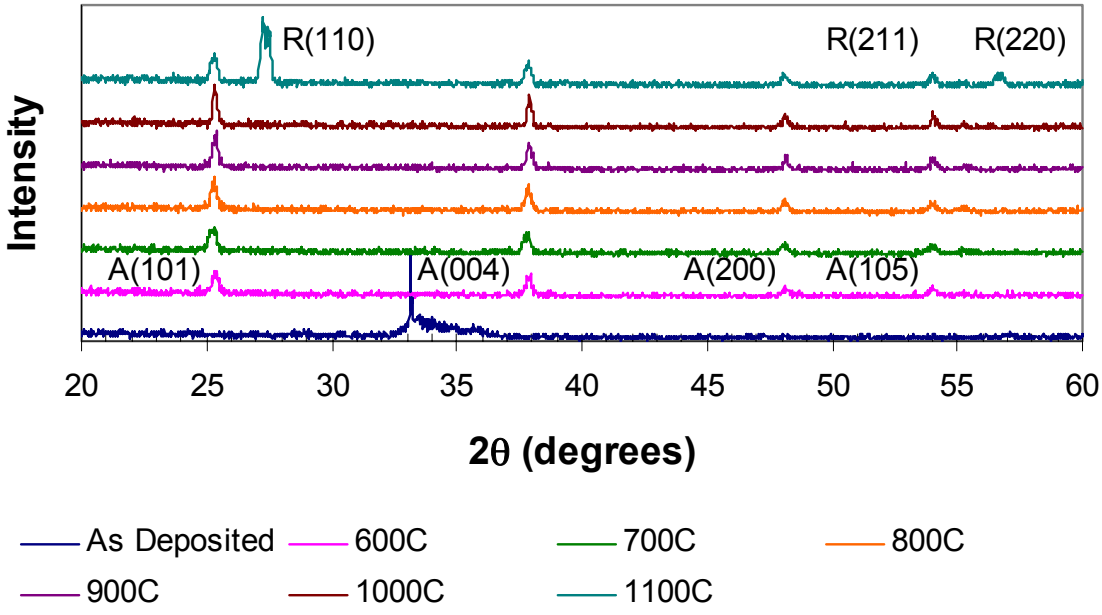

Figure 4.18. XRD patterns for an amorphous film annealed for 8 hours at temperatures from 600 to 1100°C.

The second heat treatment study yielded more useful results. Figure 4.19 plots the intensity of the strongest anatase peak (solid lines), A(101), as a function of anneal time for temperatures between 700 and 1100°C on the primary y-axis, and the rutile phase weight percentage (broken lines) on the secondary y-axis. Amorphous films deposited at 100°C have no anatase or rutile phase present before the heat treatment study began as indicated by the zero intensity A(101) peak and rutile wt.% value at an anneal

time of 0 hours in Figure 4.19. All samples converted to the anatase phase after 6 hours of heat treatment at all annealing temperatures as indicated by the sudden increase in A(101) peak intensity at 6 hours. Amorphous films were difficult to transform into rutile phase films even at temperatures of 900°C as shown in Figure 4.19. Samples annealed at temperatures between 700 and 900°C still had not converted to rutile after 30 hours of anneal time. Films annealed at 1100°C converted to 95% rutile after a 6-hour anneal, which is shown on the secondary y-axis in Figure 4.19. Films heat-treated at 1000°C were converted to a mixed 48 wt.% anatase – 52 wt.% rutile composition after 12 hours of annealing. Subsequent heat treatment at 1000°C for longer anneal times did not increase the rutile weight percentage. The intensity of the anatase peak would have decreased until it disappeared with the onset of the rutile phase.

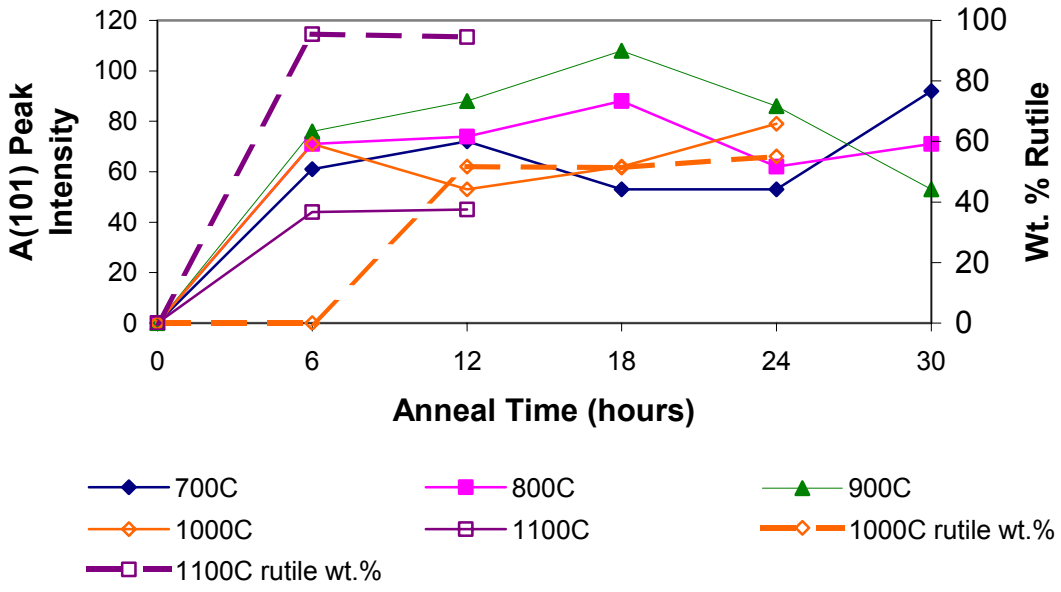

Figure 4.19. Anatase peak intensity versus anneal time for amorphous films annealed at temperatures of 700, 800, 900, 1000, or 1100 degrees Celsius. Wt.% rutile is plotted on the secondary y-axis for the 1000 and 1100°C samples that have begun the rutile phase transformation.

As shown in Figure 4.20, complete conversion to the rutile phase was not achieved at 700°C even for as-deposited films that started out as an anatase-rutile mixture. 700°C was on the low end of the reported rutile phase transformation temperature range, so this result is not surprising. However, the weight percentage of the rutile phase did increase from 38% rutile phase in the as-deposited film to 50% rutile phase after 30 hours of annealing at 700°C. The figure shows a corresponding decrease in the A(101) intensity of the anatase-rutile mixed film as the rutile weight percentage of the sample increases.

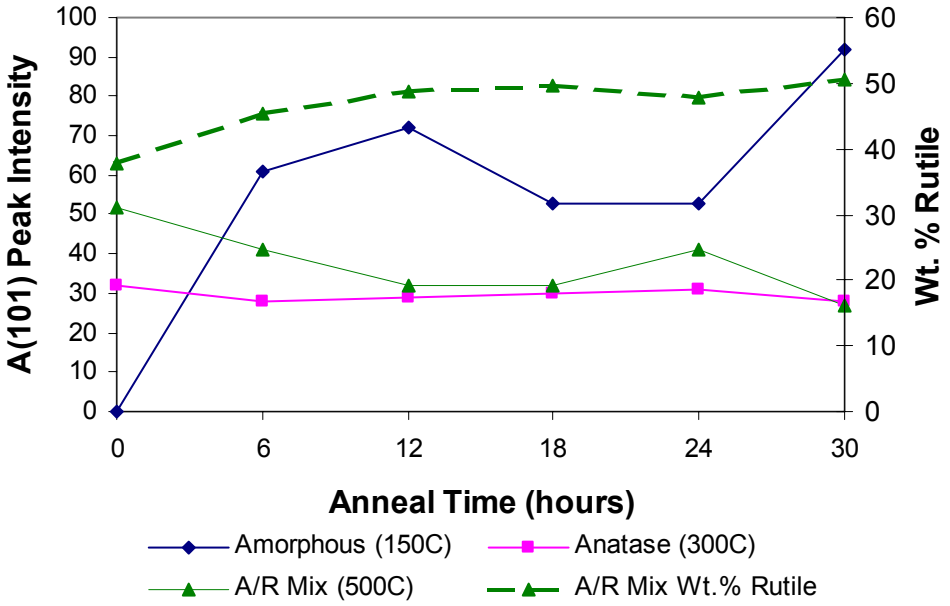

Figure 4.20. Anatase peak intensity (solid lines) versus anneal time for an amorphous, anatase, and anatase-rutile mixed film annealed at 700°C. The rutile weight percentage (broken line) for the anatase-rutile mixture is plotted on the secondary y-axis. The film was initially composed of 62% anatase and 38% rutile phases.

As–deposited anatase films grown at 300°C were very quickly converted to the rutile phase at anneal temperatures above 800°C as shown in Figure 4.21, which plots the rutile phase weight percentage versus anneal time for films annealed at temperatures

between 800 and 1100°C. All films started out in the anatase phase as indicated by the zero wt. % rutile value at 0 anneal time. The films heat-treated at 800, 1000, and 1100°C only took 6 hours to convert to 100% rutile phase. The anatase film heat treated at 900°C took longer than the other films. The intensity of the strongest anatase peak had decreased to the background level after six hours of heat treatment at 900°C, but the higher order (211) anatase peak did not completely disappear until 18 hours of heat treatment. Another anatase sample heat treated at 800°C had only converted to 68% rutile phase after 6 hours of annealing. The starting film had much better crystallinity than the anatase film which converted to rutile after 6 hours of heat treatment at 800°C.

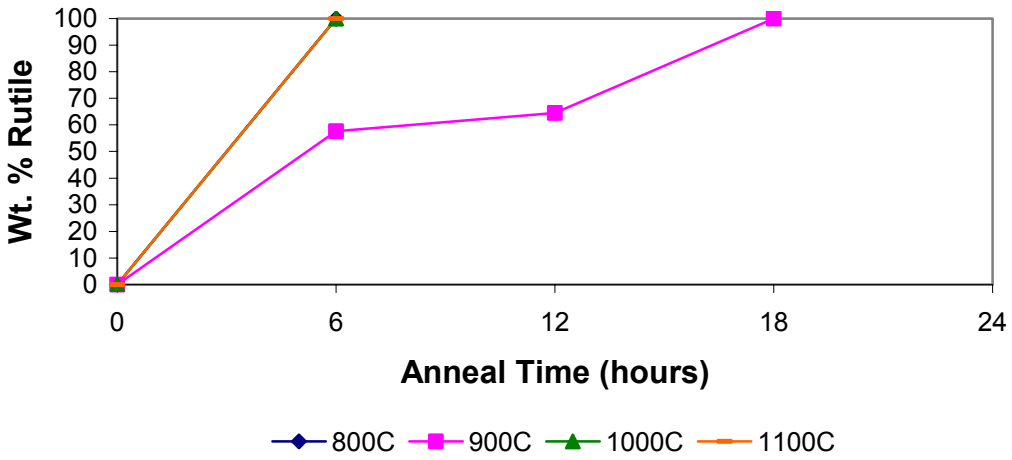

Figure 4.21. Rutile weight percentage versus anneal time for anatase films heat treated at temperatures of 800 to 1100 degrees Celsius.

Anatase-rutile mixtures converted to the rutile phase in 6 hours at anneal temperatures of 900°C and above as shown in Figure 4.22. The anatase-rutile mixture annealed at 800°C still had not converted to the pure rutile phase even after 30 hours of annealing. The anatase film heat treated at 800°C converted to rutile after only 6 hours,

so the reason for the lack of transformation of the anatase-rutile mixtures is unknown. The as-deposited film used in the heat treatment study at 800°C had a lower starting rutile phase percentage than the other films. It was also thinner than the other films, which could affect the onset of crystallization. Recall that film thickness does have an affect on the temperature at which crystallization begins as reported by Aarik *et al.* [52]

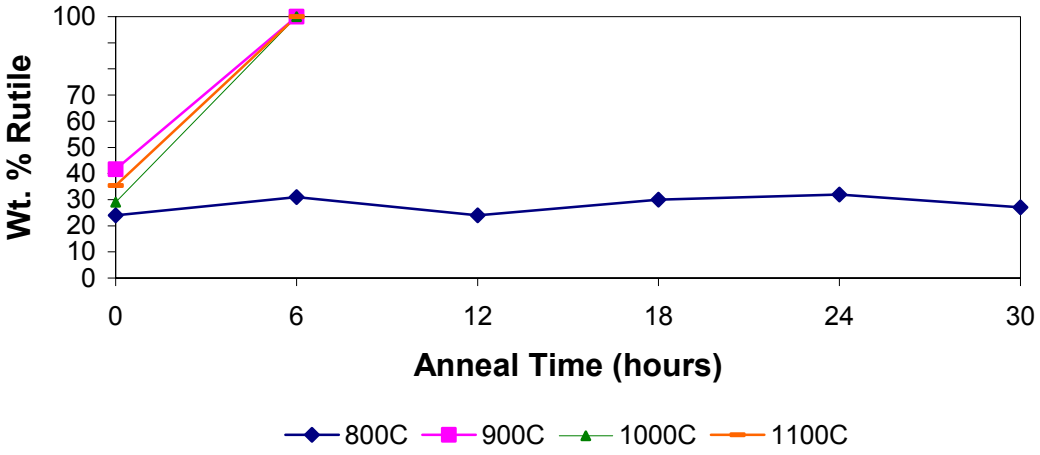

Figure 4.22. Rutile weight percentage versus anneal time for anatase-rutile mixed phase films annealed at temperatures of 800 to 1100 degrees Celsius.

4.2.2 Changes in Film Composition and Roughness

SEM pictures of an amorphous film annealed at 1100°C for 6 hours revealed the development of highly directional step-like features. After the anneal, the film was approximately 95 wt. % rutile. Unfortunately, the roughness value for this film was not obtained. The corners of the steps contained what could be a nucleation site for the development of the rutile phase as shown in Figure 4.23(b).

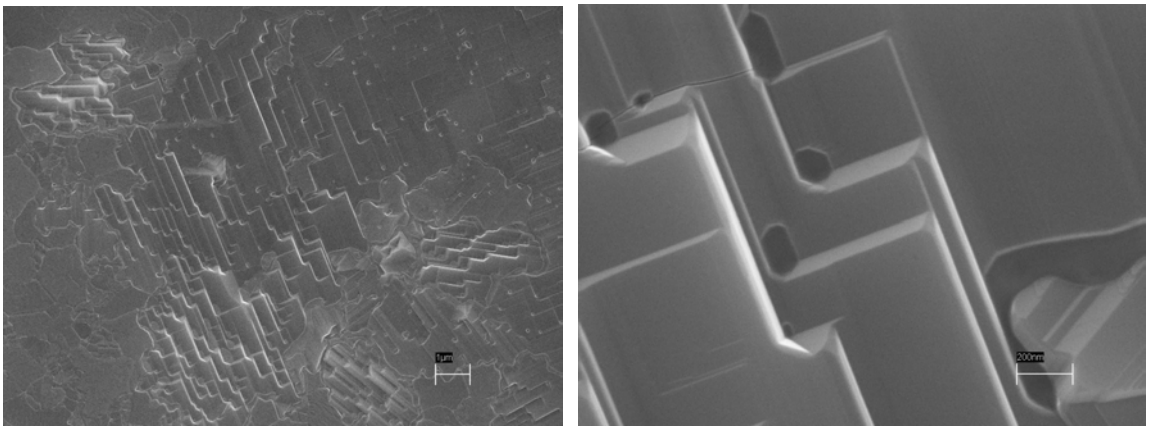

(a) (b)

Figure 4.23. (a) Low and (b) high magnification SEM images of an amorphous film heat treated at 1100^{o}C for 6 hours. Scale bar size is (a) 1μm and (b) 200nm.

4.2.3 Changes in Optical Properties

The refractive index values presented in this section were measured using specular reflectance and are comparable to the measured index values obtained from ellipsometry of the as-deposited thin films reported in Section 4.1.4. However, the fitting error for samples heat treated at 700^{o}C and above was greater than the desired error limit of 0.100 for the Filmetrics spectral reflectometer. Samples heat treated above 800^{o}C could not be fitted to a dispersion model at all due to the loss of reflectance fringes. For the first heat treatment study, the index of refraction increases with increasing anneal temperature as shown in Figure 4.24. This is consistent with the literature. The index of films annealed above 800^{o}C could not be measured due to the decrease in the reflectance fringe intensity at higher temperatures. This is attributed to increased surface roughness.

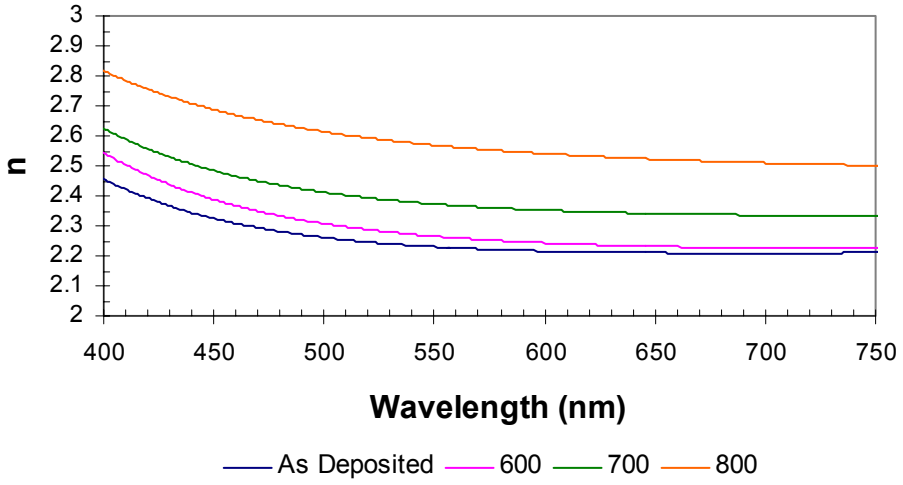

Figure 4.24. Index of refraction as a function of wavelength for an amorphous film annealed at temperatures of 600 to 800°C.

Optical measurements for the second heat treatment study yielded inconsistent data for the refractive index value. We expected to see a decrease in the film thickness as the structure underwent phase transformation from amorphous to anatase to rutile. However, only a few samples showed this result. The majority showed an increase in the film thickness or no trend at all. Examples of the trends seen in the thickness and refractive index data are shown in Figure 4.25.

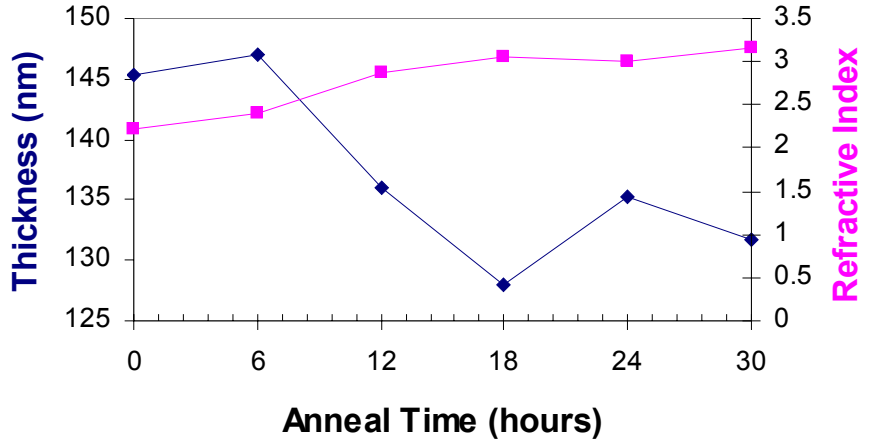

(a)

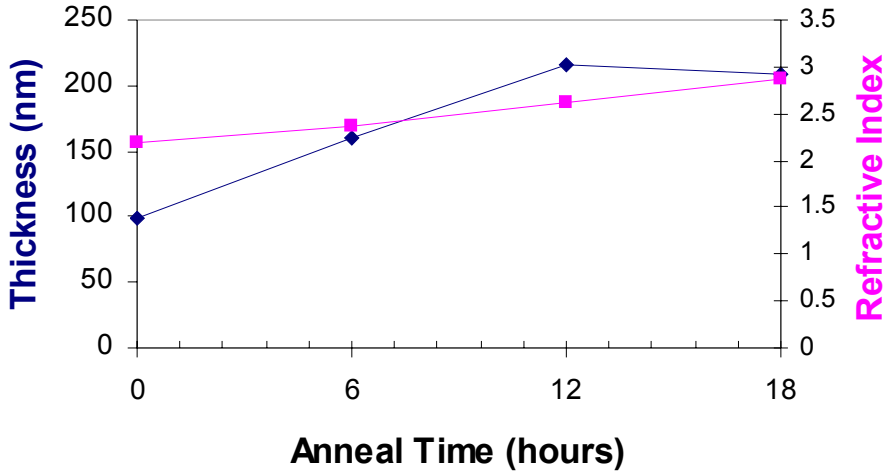

(b)

Figure 4.25. Thickness and refractive index versus anneal times with the (a) expected thickness trend and (b) unexplained increase in thickness.

4.3 Opal Infiltration

The degree of opal infiltration is typically characterized by the filling fraction of the infiltrated material. The filling fraction is calculated from the location of the (111) Bragg peak as shown in Equation 3.9, since the (111) plane of the opal grows parallel to

the substrate. The filling fraction can be determined from either reflectivity or transmission data, however transmission measurements are not reported as frequently because the loss of order over the entire crystal makes the transmission peaks wider and shallower than the corresponding reflectivity peaks. The height and width of the Bragg peaks are also reported as an indication of the strength and width of the photonic band gap.

4.3.1 Previous Studies by Summers' Photonic Crystals Group

Initial infiltration studies with ALD parameters similar to those used in the deposition of thin films resulted in large voids in the opal grains as shown in Figure 4.26, which shows a cross section of an opal infiltrated by a 2s, 2s, 2s, 2s pulse/purge sequence before the addition of the N_2 flange. A large void is revealed in the inverted opal where the titania did not fully infiltrate the SiO_2 opal. Attempts to cross section the opals by performing a masked ion mill were ineffective for determining penetration depth because the ion mill destroyed the sidewall so that distinct opal layers could not be identified or counted. Since we do not have access to a FIB and ion milling was ineffective, we developed an optical method for determining the presence of a void in the opal where the infiltrated material has not fully penetrated.

As reported in Section 4.1.1, a 2 s purge was insufficient to achieve self-limited ALD thin film growth. Therefore, longer pulse and purge times were used in subsequent studies in order to eliminate the appearance of the opal void.

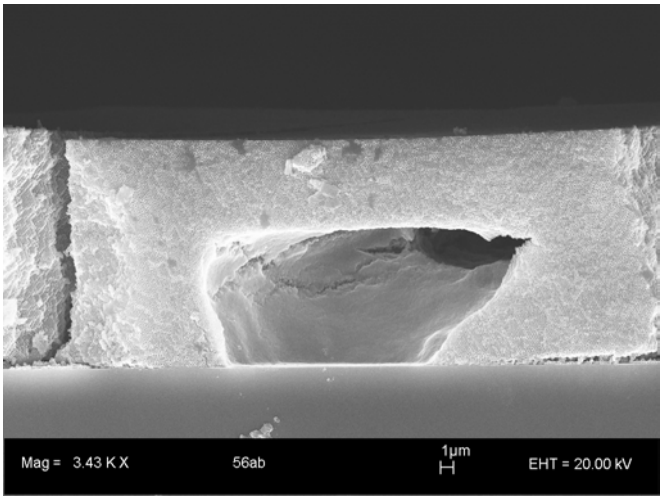

Figure 4.26. SEM image of a SiO_2 opal infiltrated with TiO_2 grown at 100°C with a 2s,2s,2s,2s pulse/purge sequence before the addition of the extra N_2 purge. Image courtesy of J. King.

In a study by King *et al.* a SiO_2 opal was infiltrated in 2 nm increments by 20 cycles.[69] The H_2O and $TiCl_4$ pulse lengths were both 4 seconds, while the purge length was 10 seconds. In addition to the longer purge time, the continuous purge from the N_2 flange insured the self-limited growth of ALD TiO_2. The infiltration was repeated for 19 iterations. The iterative ALD infiltration of the opal revealed two different regions of growth as shown in Figure 4.27. For the first 60 cycles, the growth rate was faster than for the remainder of the cycles. The maximum thickness allowed by the opal sphere size was calculated at ~20.9 nm using Equation 3.2. Therefore, assuming a growth rate of 0.98nm/cycle, the maximum filling fraction for TiO_2 should have been reached after 11 iterations. However, the opal was not completely filled until 19 iterations. Therefore, the growth rate in the opal is less than that on a planar substrate. The filling fraction after 220 cycles, as calculated from transmission measurements, was 0.625. Other groups that have fabricated inverse titania opals have reported a TiO_2 volume percentage of less than 12% out of a maximum possible volume of 26% for the FCC structure,[39] which

corresponds to a filling fraction of 0.462. The goal of the research presented in this thesis was to improve upon the filling fraction achieved by King *et al.* by optimizing the pulse and purge lengths.

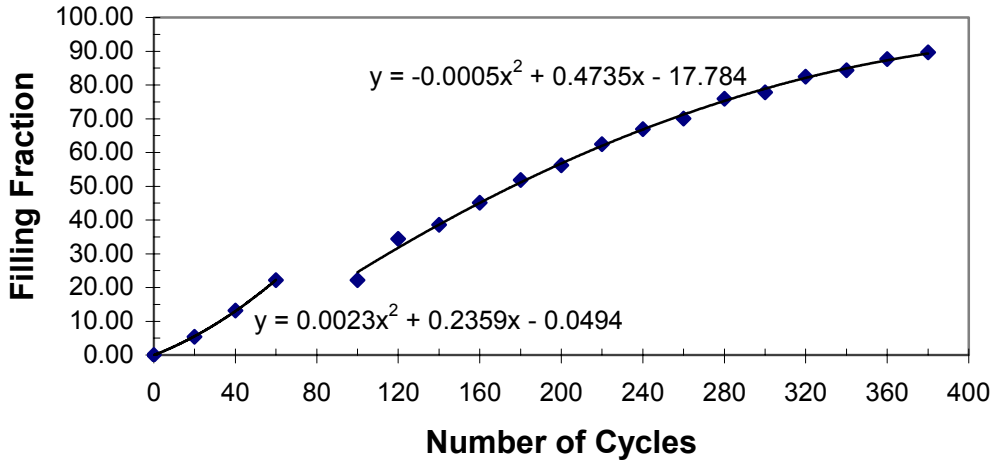

Figure 4.27. Filling fraction versus number of ALD cycles for a stepwise infiltration of 2 nm per 20 cycles. Infiltration was done with a 4s pulse and a 10s purge.[69]

4.3.2 Growth Mechanisms

The growth parameters for opal infiltration were discussed previously in Section 3.3.2. Recall that infiltration was done at 100°C in order to have highly conformal, smooth films. Longer pulses and purges are required to fully infiltrate the high surface area opal structure. The pulse and purge lengths were varied in an attempt to eliminate the two-layer structure observed in samples with insufficient pulse/purge conditions and to improve upon the filling fraction reported by King *et al.*

Effect of Pulse and Purge Length:

The filling fraction versus pulse and purge length was studied by infiltrating opal samples for 220 cycles, which corresponds to the maximum theoretical thickness of

infiltrated TiO_2 for a sphere diameter of 260 nm, with varying pulse and purge times. The pulse length study investigated the filling fraction for two different pulse conditions. The first set of conditions were those determined from the thin film study reported previously, where the H_2O pulse is equal to half the length of the $TiCl_4$ pulse. However, the iterative ALD infiltration study by King *et al.* used H_2O pulse lengths that were equal to the $TiCl_4$ pulse length, thus these conditions were also used in order to compare the data. All opal infiltration runs were done using a quartz substrate so that both transmission and reflectivity data could be taken. The transmission and reflectivity data yielded very similar results for the calculation of the filling fraction.

As shown in Figure 4.28 the filling fraction of TiO_2, as calculated from the transmission data, for both sets of conditions increased with an increase in the $TiCl_4$ pulse length. However, the filling fraction was slightly less when the H_2O and $TiCl_4$ pulses were of equal length. A few runs were done with conditions that should have resulted in clogging as seen in Figure 4.26, but the samples had relatively high filling fractions. Either the addition of the N_2 flange was sufficient to eliminate the clogging problem or filling fraction alone is not a good indication of the uniformity of opal infiltration. Hence, a side study, which will be discussed shortly, was conducted to determine if there would be a difference in the transmission of reflectivity spectrums when a sample consists of a partially infiltrated, two-layer opal structure.

Deviation in the fill fraction arises from the variable peak positions of the opal measured before and after infiltration. The peak positions varied up to 2 nm for each measurement. The error bars are based on the maximum deviation from the reported value calculated for all samples.

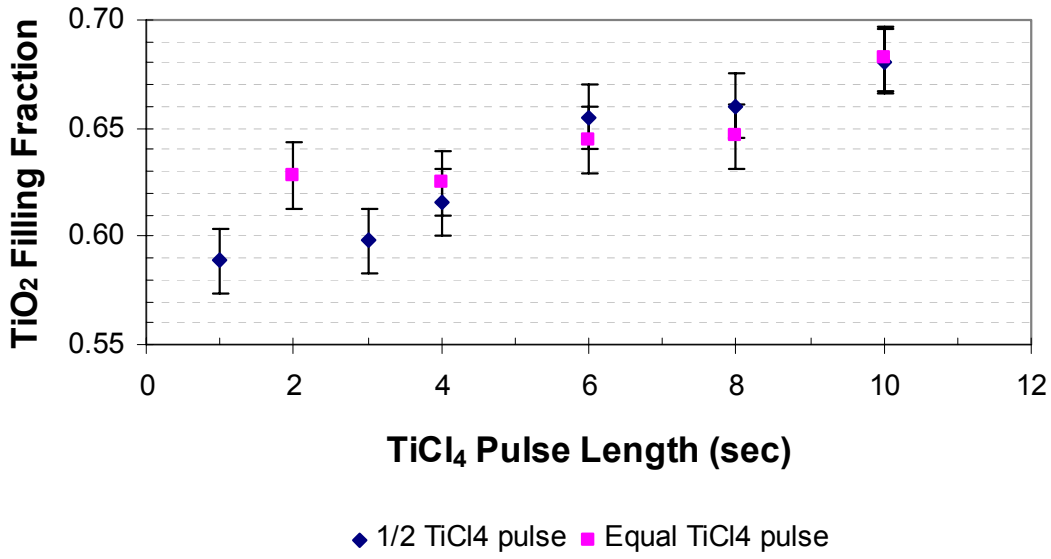

Figure 4.28. TiO_2 filling fraction as a function of $TiCl_4$ pulse length. Samples were deposited at 100°C for 220 cycles with a purge length of 10 sec for pulse lengths up to 8 sec, where the purge length was set to double the pulse length. Runs at 0.5 and 2 had equal pulse and purge lengths for both precursors.

The filling fraction decreased with an increase in the purge length as shown in Figure 4.29. The fill fraction decreases at purge lengths up to 24 seconds, then appears to stabilize. This decrease could be because the growth rate was not saturated until the pulse length was 3 times the length of the $TiCl_4$ pulse length. Unfortunately, there is no thin film data to corroborate this theory.

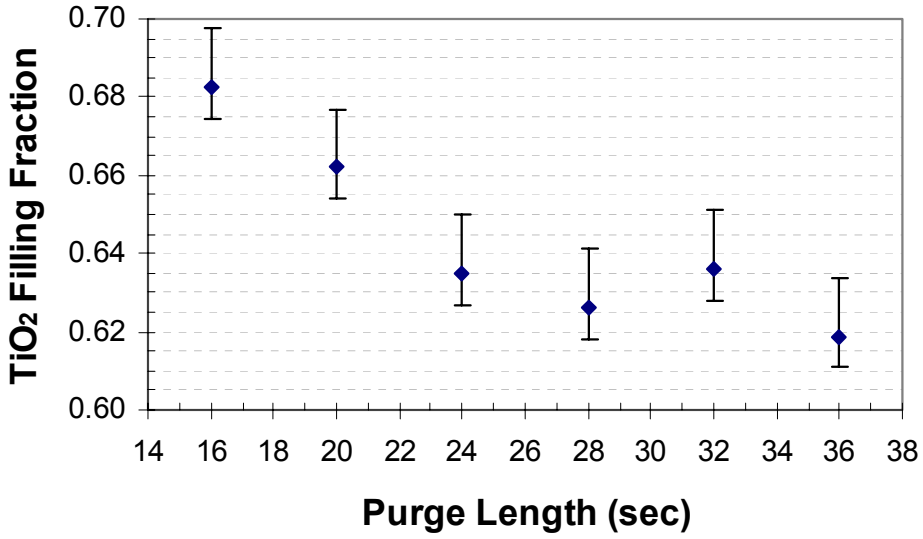

Figure 4.29. TiO_2 filling fraction versus purge length. Samples were deposited at 100°C for 220 cycles with H_2O and $TiCl_4$ pulse lengths of 4 sec and 8 sec, respectively.

Determination of Two-Layer Opal Structure:

Since the filling fraction of the short pulse and purge samples did not indicate any abnormalities in the infiltrated opals, an experiment was developed to determine if the optical data was sensitive enough to detect a partially infiltrated or two-layer opal structure like that shown in Figure 4.26. In the experiment, a non-infiltrated opal and an infiltrated opal were sandwiched back-to-back using double-sided tape. The transmission and reflectivity was measured from both the non-infiltrated and infiltrated opal side and compared with the data measured for the individual samples. The measured spectrums for the opal-infiltrated opal stack are shown in Figure 4.30.

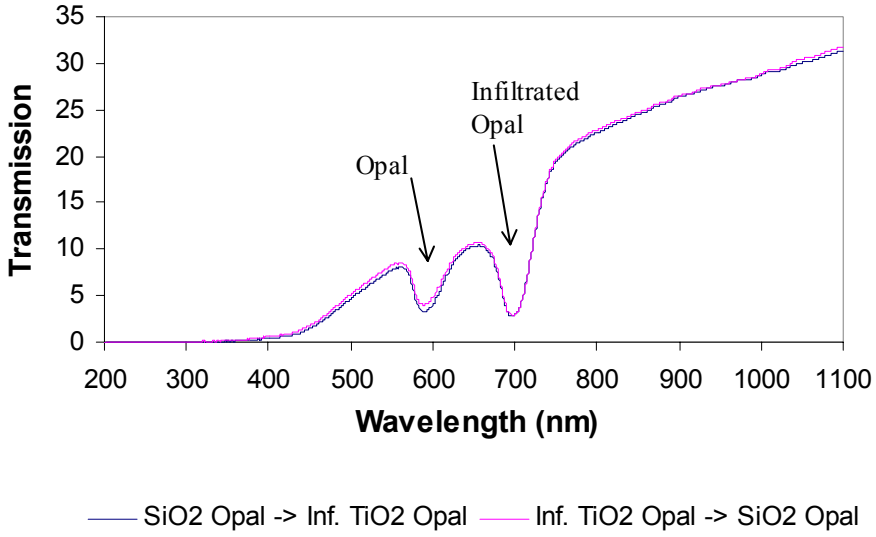

(a)

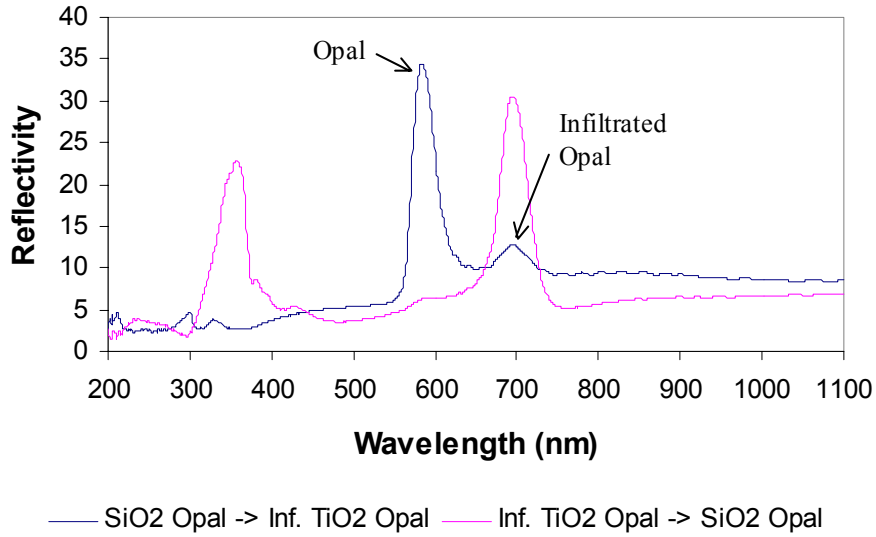

(b)

Figure 4.30. (a) Transmission and (b) reflectivity measurements of an opal-infiltrated opal stack. The infiltrated opal was infiltrated for 220 cycles with H_2O and $TiCl_4$ pulse lengths of 5 sec and 10 sec, respectively. The purge length was 20 sec.

The transmission spectrum shows two distinct peaks at 590 and 701nm that correspond to the peak positions of the bare opal and the infiltrated opal, respectively. The peaks are present in the transmission spectrum regardless of which direction the incident light comes from. The reflectivity spectrum for the opal to infiltrated opal incidence showed a strong peak corresponding with the opal peak position and a weaker peak corresponding to the infiltrated opal peak position. However, only a small shoulder corresponding to the peak position of the bare opal is seen in the spectrum when the incident light hits the infiltrated opal first. This result makes sense because the effective index of the infiltrated opal is greater than that of the bare opal, thus there will be less light transmitted to the bare opal to yield a reflection peak from the bare opal surface.

Only single peaks were observed in the transmission and reflectivity measurements described in Figure 4.28. Therefore, the infiltration is either uniform or the thickness gradient is too gradual to be detected by the optical measurements. The 2sec, 2sec, 2sec, 2sec sample should have produced significant clogging within the first few layers of the opal, but no second peak corresponding to that of a bare opal was observed. The clogging effect was observed in an opal deposited before the continuous N_2 purge flange was added to the ALD system, hence the clogging problem could have been corrected by the additional purge.

An infiltration run was done with conditions of 0.5 sec, 0.5 sec, 0.5 sec, 0.5 sec, to determine if there was a double peak observed in the transmission spectrum. In fact, a weak peak was observed in the transmission spectrum at 654 nm, which corresponds to a fill fraction of 34.9%. The usual peak corresponding to a higher filling fraction of 64.5%

was also observed. The transmission and reflectivity spectrums are plotted in Figure 4.31.

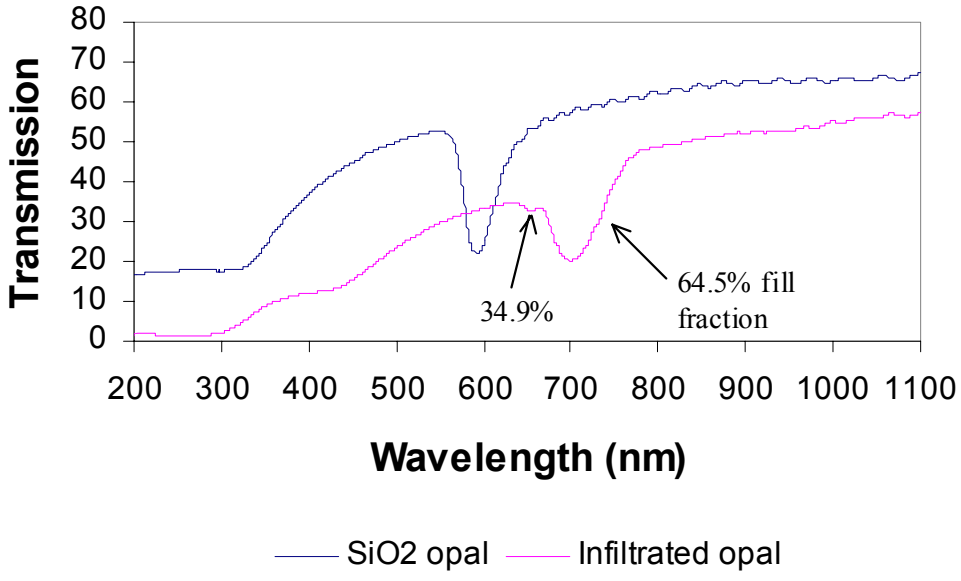

(a)

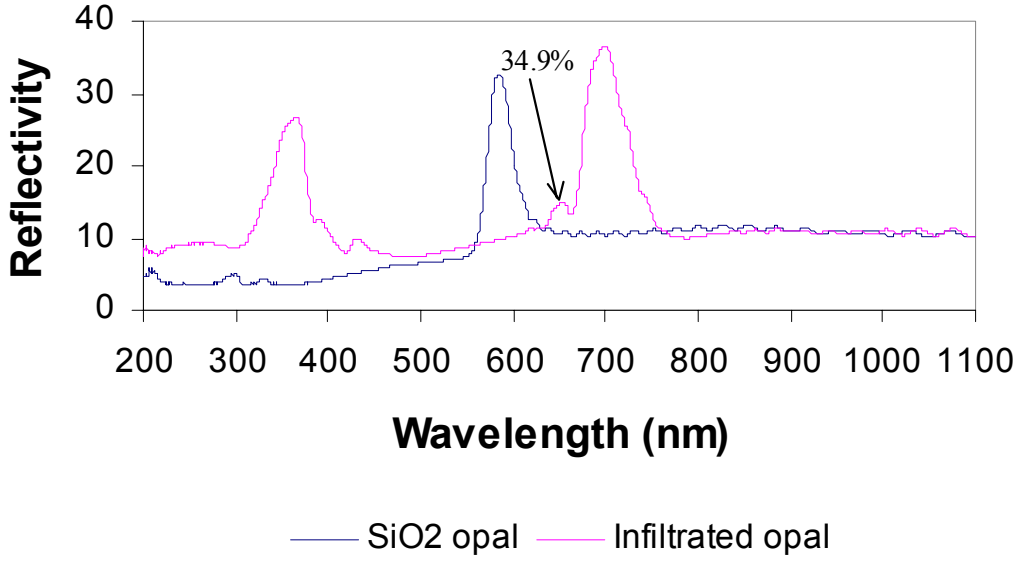

(b)

Figure 4.31. (a) Transmission and (b) reflectivity measurements of a potentially clogged sample. The opal was infiltrated for 220 cycles with equal H_2O and $TiCl_4$ pulse and purge lengths of 0.5 sec.

4.3.3 Heat Treatment

Titania was chosen as an ideal opal infiltration material because of the high index of the rutile polymorph. However, the conformality requirements of the growth limit the ALD deposition temperature to 100°C, which results in deposition of amorphous TiO_2 films. Therefore, heat treatment of the infiltrated opal was investigated in order to convert the amorphous phase to the rutile phase. The opal is inverted before heat treatment because the SiO_2 spheres will melt if subjected to the temperatures required for the rutile phase transformation. The infiltrated material was annealed at 400°C for 2 hours in order to convert it into the anatase phase before the inversion etching process because the HF used in the inversion process will etch amorphous titania, but not crystalline titania. Recall from section 4.2.1 that the amorphous thin film heat-treated at 900°C had not converted to rutile even after 30 hours of annealing. However, the heat treatment studies were performed on thin films with a thickness of approximately 100 nm, which is more than 3 times the thickness of the infiltrated film. Therefore, heat treatment of an anatase phase inverted opal was attempted at temperatures of 900 and 1000°C.

As shown in Figure 4.32 XRD of the inverse opal after 4 hours of annealing at 900°C showed in increase in the A(101) peak intensity, but no appearance of the rutile phase. The opal was then annealed at 1000°C for 4 hours, after which the sample was 77 wt.% rutile.

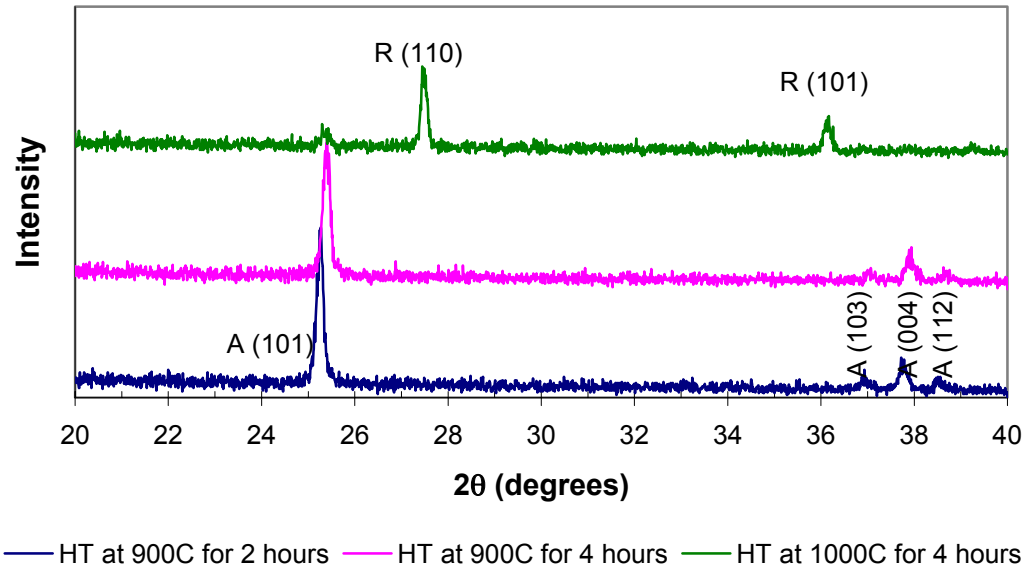

Figure 4.32. XRD patterns of the inverse opal before and after heat treatment at 900°C for 2 hours and 4 hours and also after heat treatment at 1000°C for 4 hours.

SEM imaging of the inverse opal showed a loss of the long-range order of the photonic crystal upon heat treatment as shown in Figure 4.33. The SEM micrograph of the inverse anatase opal before annealing at high temperature is shown in Figure 4.33a. The TiO_2 shell begins to break up after heat treatment at 900°C for 4 hours as shown in Figure 4.33b. The anatase-rutile mixed opal showed regions of order (Figure 4.33c), which most likely correspond to the anatase phase part of the opal, whereas the rutile parts probably correspond to the regions with no order (Figure 4.33d). A similar loss of long-range order was reported for rutile opals fabricated through precipitation of titania into a polystyrene opal template.[39] Successful fabrication of a rutile inverse opal has been demonstrated by Imhof and Pine, however they used an emulsion templating method that resulted in very porous films.[70]

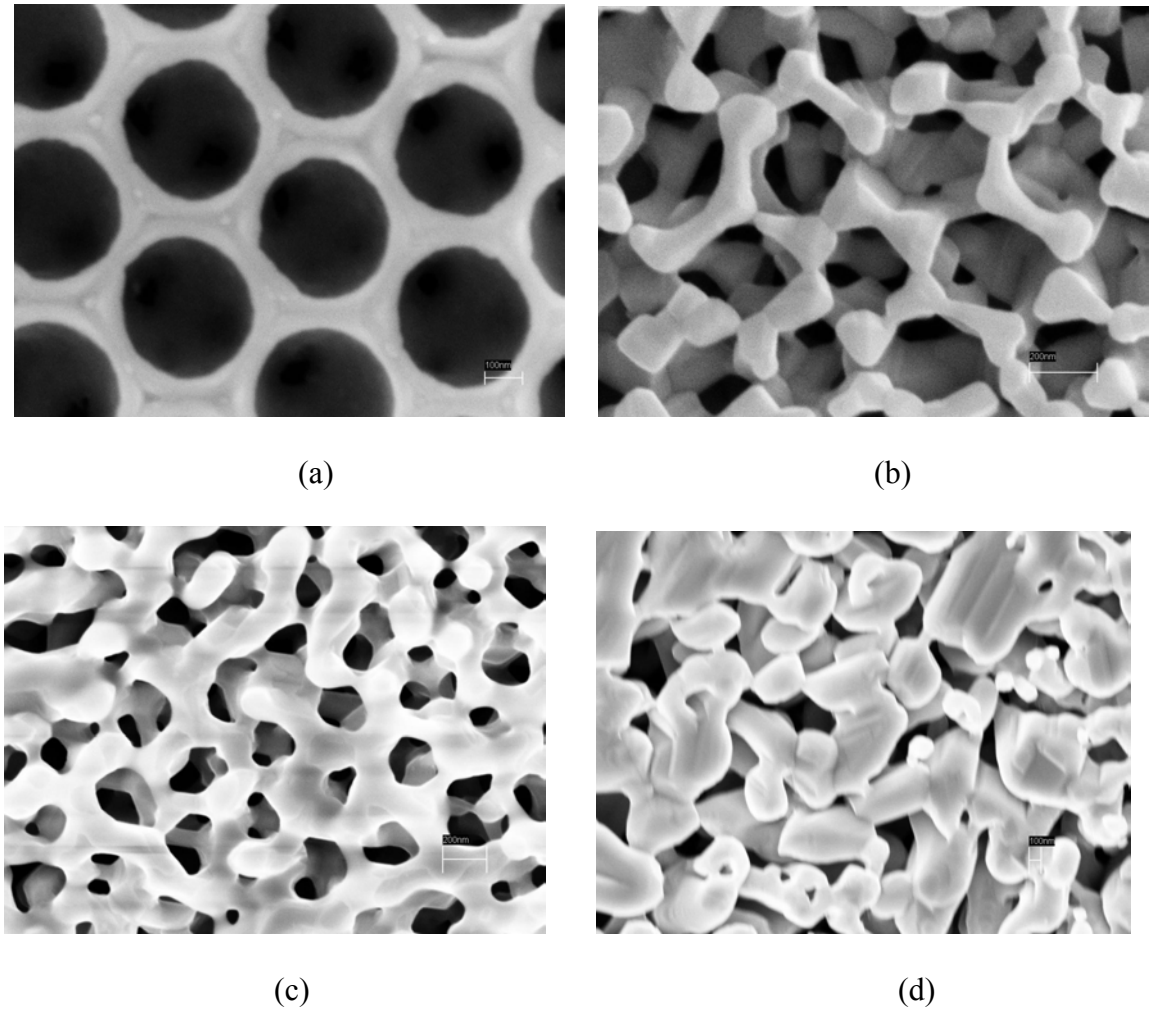

Figure 4.33. SEM micrograph of an inverted TiO_2 opal (a) before annealing, (b) after annealing at 900°C for 4 hours, and (c,d) after annealing for 1000°C for 4 hours. Crystal structure was still anatase after annealing at 900°C for 4 hours, but converted to 77 wt.% rutile after annealing at 1000°C for 4 hours. Scale bar for SEM picture a, b, and c is 100 nm, 200 nm, and 200 nm, respectively.

As shown in Figure 4.34 the loss of order after heat treatment is confirmed by the reflectivity data for the inverse opal before and after heat treatment at 900°C. The reflectance peak corresponding to the pseudo PBG almost completely disappears after heat treatment at 900°C for 4 hours.

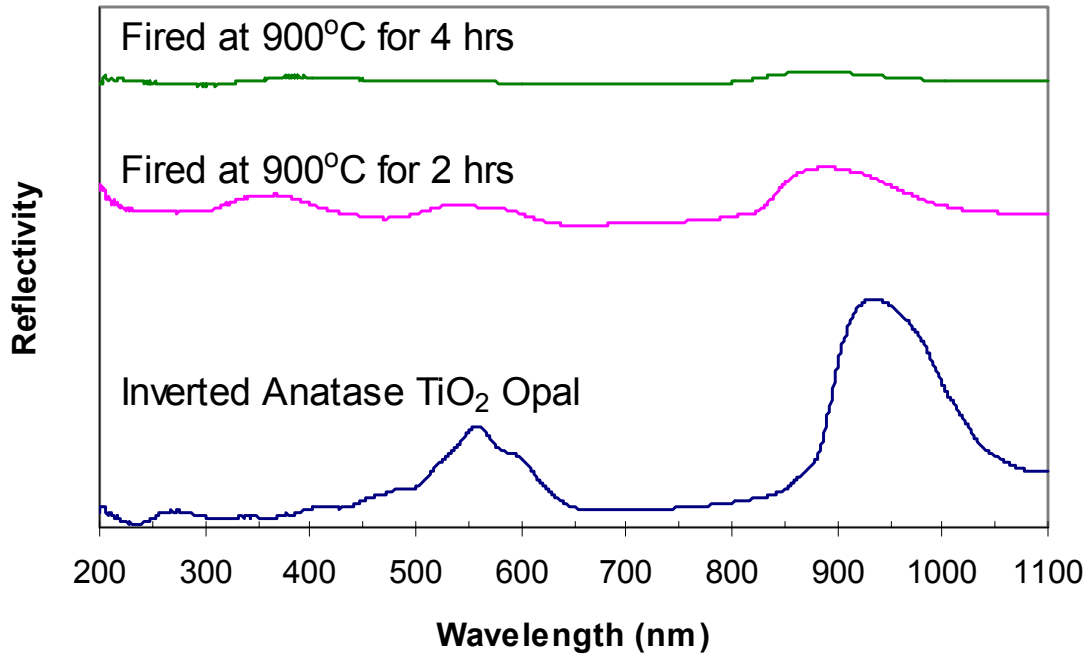

Figure 4.34. Reflectivity of the inverse opal before and after heat treatment at 900°C for 2 hours and 4 hours.

Therefore, although we can successfully infiltrate opals at 100°C, the subsequent heat treatment required for sufficient refractive index contrast destroys the long-range order of the inverse photonic crystal.

CHAPTER 5

CONCLUSION

The growth mechanisms for our custom-built ALD reactor have been described for the thin film deposition of titania, however further investigation into the infiltration of opal templates is needed before the process can be considered optimized. Inconsistencies in the thin film growth rate, especially at lower temperatures, may be improved if the temperature of the precursors was controlled. Optimization of the deposition conditions for opal infiltration was limited by the lack of a method to determine the actual penetration depth of the infiltrated titania. Optical methods demonstrated that longer $TiCl_4$ pulse times resulted in a greater filling fraction of TiO_2. The effect of the purge time on opal penetration is unclear. A change of the system configuration into a fill-hold-purge sequence may improve the infiltration depth of the TiO_2 by giving the precursors more time to diffuse and react before they are purged out of the process chamber. The fill-hold-purge method could be implemented on our system by adding a throttle valve so the N_2 is not always flowing.

Heat treatment of the amorphous phase TiO_2 resulted in destruction of the long-range order of the inverse opal. Therefore, another method for fabricating rutile inverse opals must be determined. A possible fabrication route for the growth of rutile TiO_2 opals is to deposit a thin rutile seed layer before infiltrating the opal at 100^oC. The seed layer may allow the rutile phase conversion of the infiltrated film to proceed at lower temperatures for shorter anneal times. Heat treatment of the infiltrated opal before the

inversion process may also prevent the loss of order during the rutile phase transformation.

The optical properties of the TiO_2 films were measured using various techniques, however the accuracy of index values for heat treated films is uncertain. Index values were not obtained for rutile films due to limitations of the characterization equipment for absorbing films.

CHAPTER 6

FUTURE RECOMMENDATIONS

6.1 ALD of Higher Index Materials

Other high refractive index materials of interest for inverse opal infiltration include SnS_2 and GaP. Although there have been claims of ALD synthesis of SnS_2, the method is more of a chemical precipitation reaction than a pulsing and purging of reactants.[12] Due to the difficulty of retaining opal order during heat treatment, the direct deposition of a high refractive index film would be desirable.

6.2 Photonic Band Gap Tuning through Liquid Crystal Infiltration

The practicality of photonic crystal applications would be improved if the band structure of the photonic crystal could be tuned. In recent years research has begun on using liquid crystal to tune the PBG. Liquid crystals (LCs) exhibit large optical anisotropy due to its molecular shape and alignment. The refractive index of a liquid crystal can be changed by varying the temperature and/or by applying an electric field.

In August 1999, Busch and John proposed a fully tunable 3-D band gap through liquid crystal infiltration of an inverse opal. An inverse opal is more desirable for infiltration due to the greater amount of air space. An inverse opal made of silicon can be partially infiltrated with low index nematic liquid crystal. The band gap can be opened or closed by applying an external electric field, thus changing the orientation of the nematic

director. The temperature induced nematic to isotropic liquid phase transition can result in further tunability of the band gap.[71]

In the same month, Yoshino *et al.* reported the first infiltration of a PC with liquid crystal. The band gap reportedly shifts with a change in temperature, however no investigation into the electric field effect was reported. Yoshino *et al.* infiltrated a self assembled silica opal made by sedimentation of a suspension of 300 nm monodispersed silica spheres. They investigated the band gap shift of opals infiltrated with both nematic and smetic liquid crystal. The nematic LC used was ZLI1132 (Merck) and the smetic LC was (R)- 4'- (1- methoxycarbonyl - ethoxy) phenyl – 4 - [4-(n-octyloxy)phenyl] benzoate (1MC1EPOPB). Infiltration was achieved by immersing the sintered opal in LC solution. The opal infiltrated with nematic LC showed a red shift in the band gap by about 70 nm. The stop band was also shown to shift with a change in temperature. This was due to the decrease in refractive index as the LC underwent the nematic to isotropic liquid phase transition. A red shift was also seen in the PC infiltrated with smetic LC.[72]

Leonard *et al.* reported the realization of Busch and John's proposed tunable PC in 2000. While the proposal was for a 3-D tunable band gap, only a 2-D tunable band gap was achieved. A two-dimensional PC was fabricated in macroporous silicon. Macroporous silicon was formed on n-type silicon wafers when anodized in an aqueous hydrofluoric acid solution. The pores had a pitch of 1.59 μm and a height of 100 μm. The PC was infiltrated with liquid crystal, which was in the nematic phase at room temperature and undergoes a phase transition to the isotopic phase at 59^{o}C. The infiltration was achieved by submerging the PC into a small amount of LC heated into the isotropic phase. The nematic liquid crystal used was E7 purchased from EM Industries

Inc. The ordinary and extraordinary refractive indices at a temperature of 35°C and at a wavelength of 10.6 μm were 1.49 and 1.69, respectively. The transmission spectrum of the PC showed a wide stop band from 3.3-5.7 μm. The infiltrated PC showed a dramatic shift in the stop band to 4.4-6.0 μm. The stop band was also reported to shift 70 nm upon the liquid phase change from nematic to isotropic. This redshift occurred as the liquid crystal was heated from 35 to 65°C.[73]

In a May 2001 paper, Meng *et al.* reported the first tunable band gap by application of an external electric field. A silica opal was fabricated between two indium tin oxide (ITO) plates using a self-assembly technique. The silica spheres used to make the opal were 300 nm in diameter. The opal was then infiltrated with nematic liquid crystal into the sandwich cell. The nematic liquid crystal used was 4-pentyl-4'-cyanobiphenyl (5CB, Merck). The evaluated refractive index of the LC was 1.695 at a wavelength of 726.5 nm. A potentiostat/galvanostat and a regular dc power supply were used to supply the external electric field. The photonic band gap shifted to a longer wavelength by about 90 nm after infiltration. The PBG shifted to shorter wavelengths by about 2 nm upon application of an external electric field.[74]

Shimoda *et al.* also demonstrated tuning of the stop band upon application of an electric field in a November 2001 paper. This was a continuation of the work reported by Yoshino *et al.* in 1999. A silica opal composed of 300 nm spheres sandwiched between ITO plates was infiltrated with nematic liquid crystal. The nematic liquid crystal used was Merck's 5CB, same as in the work reported by Meng *et al.* The refractive indices of 5CB for ordinary and extraordinary light 720 nm in wavelength were 1.522 and 1.706, respectively. The averaged refractive index was 1.584. The electric field effects were

determined by applying a rectangular voltage (f=1 kHz). The reflection peaks of the infiltrated opal showed a blue shift with an increase in voltage. This shift was caused by the change in refractive index due to molecular reorientation along the applied electric field. The maximum wavelength shift recorded was 5.5 nm at 160 V. The wavelength started to shift at applied voltages above 10 V. The infiltrated opal exhibited an optical memory effect. Once the reflection peak shifted to a shorter wavelength it did not revert back to its original position unless it was heated into the isotropic phase.[75]

The first 3-D inverted opal was infiltrated with LC by Mertens *et al.* in 2002. They demonstrated a shift in the band gap by changing the temperature of the LC. The liquid crystal used was Merck's nematic E7 which consisted of 4-n-alkyl-4'-cyano-biphenyles and respective terphenyles. E7 had an average refractive index of 1.612. A PC composed of 200 nm PMMA spheres was infiltrated with nematic liquid crystal. The infiltration resulted in a redshift of the (1,1,1) reflection peak. A small blueshift of 2 nm resulted when the temperature was increased from 23 to 70^{o}C. This blueshift was due to the decreasing average refractive index of the liquid crystal with increasing temperature. A SnS_2 inverted PC was also infiltrated with LC. PMMA spheres of diameter 281 nm were used as a template for the inverse opal. The volume fraction of SnS_2 was less than 10%. The maximum volume fraction for an inverse opal is 26%. The reflection peak of the inverse opal also showed a redshift after LC infiltration. Changing the temperature from 23 to 70^{o}C resulted in a blueshift of 14 nm, which was much larger than the shift seen in the PMMA opal. The larger shift was due to the large volume fraction of liquid crystal in the inverted structure.[76] Work is currently being done on the effect of an applied electric field on the band gap.

The theory of LC infiltration of PCs was further explored in a paper by Takeda and Yoshino in late 2002.[77]

Theory and preliminary results indicate the reality of a fully tunable photonic band gap using liquid crystal infiltrated opals. Many groups have shown that the band gap shifts with a change in temperature. Only two groups have shown a similar shift with the application of an electronic field. Theory shows that inverse opals offer better tunability due to the increased amount of air space. However, only one group has published work on the infiltration of an inverse opal. Research has recently begun on the infiltration of a titania inverse opal, however it has not been successful.[78] This is an area where some original work could be done.

6.3 Sulfidation of Titania

The conversion of TiO_2 into TiS_2 by thermal treatment in an H_2S atmosphere, a process known as sulfidation, has been the topic of considerable research because of its applications in fuel cell membranes and hydrodesulfurization (HDS) processes.[79,80,81] Other materials that have been successfully converted from an oxide to a sulfide include ZnO[82] and Y_2O_3. However, we have found no report of the sulfidation of TiO_2 thin films in a H_2S atmosphere. No optical data for the TiS_2 conversions exists in the literature. It would be interesting to investigate the change in structure and index of refraction associated with the sulfidation of TiO_2. It is already known that TiS_2 has lower band gap energy than TiO_2.

Guo *et al.* reported the sulfidation of titania pellets by a sulfur vapor.[79] The TiO_2 pellets were sealed with sulfur in a quartz tube. The temperature of the pellets was controlled at 900 or 1000°C. The sulfur was kept at a cold temperature of 500°C. The sulfur pressure in the tube was approximately 202 kPa. The reaction time was either 10 hours or 3 days. Although the XRD results did not show the presence of TiS_2, the absorption spectrum showed a decrease in the energy gap. The group assumed that the sulfidized compound either had the same structure as the TiO_2 or the amount of the 2nd phase was too small to be detected. Substitution of sulfur for oxygen was found to greatly improve the photoresponse of the material.

Amorphous alkoxy-sulfide precursors were heat treated in H_2S to form crystalline TiS_2 particles by Sriram *et al.* in 1995.[80] The precursor powders were amorphous. The powders developed the crystalline (anatase and rutile) TiO_2 and TiS_2 phases after heat treatment at 600°C for 6 hours in an H_2S environment. The TiS_2 is hexagonal phase. The XRD patterns show single phase TiS_2 at 700°C for 6 or 10 hours, depending on the composition of the precursor powder. The reaction of the oxide groups with H_2S caused the release of H_2O as shown by the following reaction:

$$TiO_2 + xH_2S \rightarrow TiO_{2-x}S_x + xH_2O \qquad (6.1)$$

The rate of water release was dependent on the rate of the sulfidization reaction.

ZnO films prepared by dip-coating were sulfidized to synthesize ZnS films.[82] ZnO was deposited on glass slides and silicon wafers. The ZnO films were annealed at 700°C after the desired coating thickness was achieved. The ZnO films were then heated

by infrared radiation in an atmosphere of 9:1:10 $N_2/H_2/H_2S$ in order to convert the films to ZnS. The films were heated at temperatures of up to 560^oC at a gas pressure of 930 Pa. XRD of the as deposited ZnO films indicated that they were amorphous. The ZnO films became crystalline with the hexagonal structure after the 700^oC anneal. The thermodynamically stable state for ZnO is the cubic, zinc blende structure. The XRD results showed the beginnings of the ZnS conversion after a 75 minute anneal in a sulfidizing environment. The almost total conversion to ZnS took place over longer annealing times.

Rodriguez *et al.* showed that sulfur replaces oxygen atoms at 300^oC by adsorbing at the position of the bridging oxygen rows.[81] The anatase TiO_2 surface was exposed to sulfur vapor.

The sulfidation system needed to convert TiO_2 to TiS_2 is already set up and available for use. It consists of a quartz reaction chamber housed in a furnace with a gas control system for introducing N_2 and H_2S gases separately into the furnace tube through quartz feedthroughs.

APPENDIX A

CONFINEMENT CELL PROCESS TRAVELER

Slide Cleaning:

1. Cut microscope slide into 2x2 in. square using scribe tool (work with a maximum of 6 slides at a time, evaporator cannot hold >6 slides)
2. Rinse with acetone, scrub with cleanroom q-tip
3. Warm DI water rinse
4. Rinse with methanol, scrub with cleanroom q-tip
5. Warm DI water rinse
6. Rinse with Microclean, scrub with cleanroom q-tip
7. Warm DI water rinse, dry with N_2
8. Soak in hot sulfuric acid for 5 minutes (set hotplate to 2)
9. Rinse in warm DI water bath
10. Rinse in water, scrub with cleanroom q-tip
11. Dry with N_2
12. Bake at 110^{o}C for 5 minutes
13. Dispose of waste in Solvent Waste container
14. Refill DIW container by turning black knob over sink to the left
15. Dispose of sulfuric acid by slowly pouring acid into an overflowing container of water

Positive Photoresist (Shipley S1813):

1. Remove slides from oven, allow to cool
2. Set up spinner – turn on light, blower, and press power button, check that vacuum is working, cover bowl with lint free wipes for easier cleanup, pour positive photoresist into clean beaker (~25 mL per 6 slides), set acceleration to maximum, spin speed to 5000 rpm, spin time to 25 sec
3. Blow off slide with N_2 gun
4. Place slide over center vacuum hole, turn on vacuum, check that slide doesn't wiggle
5. Pipette PR onto slide so that slide is completely covered
6. Spin PR at 5000 rpm for 25 sec
7. Hit reset, vacuum button
8. Remove slide from chuck
9. Soft bake in convection oven at 95^{o}C for 30 min
10. Clean spinner with acetone while waiting for slide to bake
11. Allow slide to cool
12. Blow off mask with N_2 before using. Check that mask is clean. If not then refer to mask cleaning procedure on page 5.

13. Align mask with sample slide, make sure UV lamp reaches max power of 10 mW before exposing first slide – to turn on mask aligner flip four switches in order from right to left (N_2, power source, aligner, lamp control), wait for lamp to say "rdy", then hit Start button, wait until display reads 274/275 W before exposing slide
14. Expose for 6 sec
15. Turn off mask aligner by flipping four switches in order from left to right (opposite of when you turned it on), push Reset button on N_2 box
16. Soak in chlorobenzene for 10 min
17. N_2 dry (do not rinse off with DI water)
18. PEB at 95^{o}C for 10 min
19. Allow to cool
20. Develop in AZ351 developer for 1 min, 3.5:1 – 70 ml DI water:20 ml AZ351, agitate slide using three prong tool
21. Thorough DI water rinse
22. N_2 dry
23. Check for residual resist (slide will look streaky if there is residual resist)
24. Dispose of solvent waste in Waste container, 351 developer can be poured down the sink drain

NOTE: Optional ammonium hydroxide etch to remove residual resist

Aluminum Evaporation:

To load slides

1. Chamber will be under high vacuum (HV Valve button will be lit)
2. Push HV Valve (yellow) button to turn off
3. Turn black knob on N_2 pressure gauge counterclockwise, push Vent Valve (red) button to vent chamber, wait for chamber to vent
4. Jiggle lid to see if it moves
5. Lift lid with Up switch
6. Turn off Vent Valve, turn black knob on N_2 pressure gauge clockwise
7. Lift out round metal specimen holder (be careful, it is heavy)
8. Load slides on specimen holder (you can fit up to six slides)
9. Replace specimen holder so that shadow of mirror is in back, be careful not to hit Inficon sensor
10. Swing round protective barrier out of the way
11. Lift crucible out of chamber with tweezers (may be hot) and check for cracks
12. Refill with aluminum pellets if necessary (2-3 pellets should be sufficient), first rinse pellets with trichloroethylene
13. Lower lid with Down switch
14. Line up marks on chamber lid and base
15. Push Roughing Valve (white) button to begin pumping down the chamber

16. Check pressure with auxillary gauge, turn on vacuum monitor, press AUX GAUGE button twice, wait until pressure reaches mid-10^{-3} scale (~5 x 10^{-3} Torr), turn off vacuum monitor
17. Turn off Roughing Valve
18. Turn on HV Valve
19. Wait for chamber to pump down to ~5 x 10^{-7} Torr, this will take about an hour

Deposition

1. Check vacuum using Ion gauge, turn on vacuum monitor, press ION GAUGE button once, press FIL. ON/OFF button, pressure should be ~5 x 10^{-7} Torr, press FIL. ON/OFF button again, turn off vacuum monitor
2. Check that cooling water is on (turn green handle slightly to the left), you should see water flowing into drain behind Veeco
3. Turn on power supply (3 attached black switches)
4. Turn key to Local, all lights should be green
5. Turn on Inficon
6. Display data screen, press Disp. Button, then the number 8 button, a screen should appear with Deposition Rate, Percentage, and Deposition Thickness
7. Choose which film you want to deposit, press Film # button, then the number 1 button for aluminum
8. Switch Inficon to manual mode by pressing MAN button
9. Turn high voltage on by pressing High V button on power supply
10. Use toggle controller to increase percentage to 3-4%
11. Move shutter (slide lever forward under chamber) when Al starts to melt and deposition thickness starts to go up
12. Zero the thickness by pressing ZERO THK Button
13. Deposit Al at rate of ~4 Å/sec by toggling Percentage between 4 and 5%, target thickness is 1.3 kÅ
14. Close shutter when target thickness is reached
15. Decrease Percentage, and press Stop on toggle controller (push button down)
16. Turn off Inficon
17. Turn High V off, key to Lock, and power supply off
18. Let chamber cool before venting (~3-4 min)

To unload slides

1. Follow procedure for loading slides

NOTE: If slides have a milky white appearance after Al deposition then there was probably some residual positive resist on the slide, make sure you fully develop and rinse slides

Aluminum Lift-off:

1. Fill petri dish with acetone
2. Put slide in petri dish and cover – DO NOT LET ACETONE DRY OUT
3. Soak until aluminum begins to bubble and lift off on its own
4. Remove slide with tweezers, rinse with acetone until most Al is rinsed off
5. Place in clean acetone bath (optional – you can just put it back in the original bath if there is not too much Al floating around)
6. Use q-tip to gently scrub in direction of Al lines, also scrub rest of slide to get rid of any residual Al debris
7. Remove slide with tweezers
8. Rinse with acetone
9. Rinse with methanol, use cleanroom q-tip to wipe across surface of slide in one direction
10. Water rinse
11. Gently scrub with microclean and cleanroom q-tip
12. Water rinse
13. Dry and place slide in 110^{o}C oven
14. Dispose of waste in Solvent Waste container

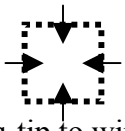

* Alternative liftoff procedure: Place beaker filled with acetone in the ultrasonic cleaner to remove Al – this reduces the amount of scrubbing needed and results in better defined lines

Negative Photoresist (Microchem Corp SU-8 2010):

1. Remove slides from oven, allow to cool
2. Set up spinner – turn on light, blower, and power, check that vacuum is working, cover bowl with lint free wipes for easier cleanup, pour negative photoresist into clean beaker (~25 mL per 3 slides), set spin speed to ~3250 rpm, acceleration to 1500 rpm in 15 sec (almost completely off), and spin time to 60 sec
3. Blow off slide with N_2 gun
4. Place slide over center vacuum hole, turn on vacuum, check that slide doesn't wiggle
5. Pour PR onto slide, remove any air bubbles by sucking off fluid with a pipette
6. Spin PR at ~3250 rpm for 60 sec
7. Hit reset, vacuum button
8. Remove slide from chuck with tweezers
9. Soft bake on hotplate at 60^{o}C for 2 min, ramp to 95^{o}C and continue bake for 2 min – in order to ramp hotplate: press Up arrow and Enter at the same time, scroll through options by pressing Index button until you see Prog9, select Prog9 by pushing Up arrow until it says ON and then hit Enter, scroll through options using Index button until you see SETPT, change set point to 95^{o}C using Up arrow, hit Enter
10. Turn off ramp program, reset hotplate temperature to 60^{o}C
11. Allow slide to cool

12. Expose for 2 min
13. PEB on hotplate at 60°C for 1 min, ramp to 95°C and continue bake for 2 min
14. Allow to cool
15. Develop in SU-8 developer for 4-5 min (although product literature specifies 2 –3 min), agitate slide with three prong tool
16. Scrub gently with lint free q-tip along direction of wall 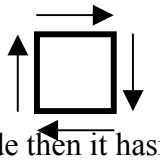
17. 2-Propanol rinse
18. Acetone rinse
19. DI water rinse, if there is a white milky film on the slide then it hasn't been fully developed
20. N_2 dry (lower gun pressure)
21. Measure wall height with profilometer – align area of interest to center hole, engage side lever, adjust x/y to find area of interest, adjust up until needle comes in contact with sample, fine adjust until measuring in "green."
22. Clean spinner with acetone
23. Dispose of waste in Solvent Waste container

NOTE: When using SU-8 10, spin on at ~2900 rpm for 60 sec, SB at 60°C for 2 min, 95°C for 5 min, expose for 1.75 min, PEB and develop is the same as for SU-8 2010

Aluminum Etch:

1. Place sample in AZ 351 bath
2. Allow sample to soak until all aluminum is gone and cell wall floats to top of solution

Mounting Cell:

1. Clean a new slide for mounting and transporting the finished confinement cell, acetone scrub, methanol scrub, water rinse, microclean scrub, water rinse
2. Place clean slide in clean petri dish filled with water
3. Remove cell from Al etch (351 photoresist developer – sodium hydroxide), cell will be floating in etch, grasp slide with tweezers and lift up under cell, guide cell into center of slide using pipette
4. Rinse cell with water using the pipette, squirt along four edges of cell, be careful not to lose cell (rinse can be done over Al etch cover)
5. Transfer cell into petri dish with clean water by squirting water on cell until it floats off into dish
6. Mount cell onto transfer slide, grasp slide with tweezers and lift up under cell, guide cell into center of slide using pipette
7. Dry cell with low pressure, turn pressure down to ~20, dry center of cell first, start with gun about 8 inches above cell, then move it closer, dry along cell walls, dry slide edges
8. Turn air pressure back up to ~40

Cleaning for Aluminum Reuse:

1. Rinse with TCE
2. Rinse with acetone
3. Place acetone bath in ultrasonic cleaner, hold slide in bath with three prong tool
4. Rinse with acetone, scrub
5. Rinse with methanol, scrub
6. DIW rinse
7. Rinse with microclean, scrub
8. DIW rinse
9. N_2 dry
10. Bake in 110^{o}C oven
11. Follow negative photoresist procedure

Mask Cleaning:

1. Blow off mask with N_2
2. Rinse with acetone, scrub
3. DIW rinse
4. Rinse with methanol, scrub
5. DIW rinse
6. N_2 dry

APPENDIX B

ALD PROCESS TRAVELER

System Start Up:

1. Fill pump with Fomblin oil to minimum level.
2. Plug pump into front panel of ALD system. Solenoid valves should also be plugged in here.
3. Turn scrubber inlet diverting valve to bypass the scrubber.
4. Turn front panel toggle switch ON. The green light indicates that the solenoids are on.

Run Set Up (with pump already on):

System Check

1. Check oil level and pressure. Oil level should be halfway minimum and maximum. Add Fomblin oil if level is below minimum. Oil pressure is typically between 10 and 15 psi. Make a note in logbook if pressure reading is anomalous.
2. Check N_2 supply. If liquid N_2 level is reading near empty, set up a new tank before run.
3. Set N_2 flow meters to vacuum pump to 5 scfh. These go to the nitrogen bubbler and the gas ballast.
4. Check pH of scrubber solution on a weekly basis. Make a note of pH in logbook.

Load Sample

1. Close vacuum ball valve.
2. Increase N_2 flow to maximum (~999 sccm).
3. Unscrew QF25 clamp at process tube inlet.
4. Wait for channel 1 vacuum reading to come to atmospheric pressure (~750 Torr). QF flange should fall off. If not, twist until it comes off.
5. Scrape out debris, if any.
6. Load clean sample into process tube with Teflon coated (brown) rod. Optimum sample position is 15" from gas inlets. Make sure sample is flat (horizontally). It's okay if it leans vertically (toward the gas inlet). Adjust thermocouple position so it is directly beneath the sample in the tube. Record sample position in logbook.
7. Reclamp QF25 flange to process tube inlet. Decrease N_2 flow to 200 sccm. Flip N_2 flow toggle switch to OFF.
8. Turn the scrubber inlet diverting valve to bypass (arrow pointing up).

9. Slowly open vacuum ball valve. Watch vacuum pressure slowly decrease from atmospheric pressure to vacuum pressure of ~0 Torr.
10. Turn scrubber inlet diverting valve so gas flows into scrubber (arrow pointing down).
11. Flip N_2 flow toggle switch to ON. Set flow to 200 sccm if it isn't already set.

Run Start up (if using programmed temperature run)

1. Close furnace top.
2. Set temperature program:
    a. Edit existing program by using the following steps: Press and hold P (program) button until *Pnr 1* appears. Press P button to scroll through program parameters. View current parameter value by pressing up arrow once. Change parameter value by pressing up/down arrow until desired value is reached.
    b. *PR1* should already be set to **step**. This will make the program ramp to the setpoint temperature as quickly as possible.
    c. Set *PL1* to the desired temperature in degrees Celsius.
    d. Set *PD1* to the desired dwell time in minutes. Dwell time should be 45 minutes plus the ALD run time.
    e. Parameters for *PR2*, *PL2*, and *PD2* are already set to cool the furnace down to room temperature as quickly as possible and end the program.
3. Turn Thermolyne Heat button ON.
4. Run temperature program: Press P button until *Pnr1* appears. Press Run/Hold button once. Program will start.
5. Use LabVIEW program **V5 – use this one.vi** to set up ALD run parameters.
    a. Press Run button (white arrow in upper left corner).
    b. Input values for *H_2O Pulse/Purge Time and $TiCl_4$ Pulse/Purge Time*. Time should be in milliseconds.
    c. Input value for *Total Loops* (number of cycles).
    d. Set *Initial Delay Time* to 35 minutes.
    e. Click check mark in upper left corner to finalize parameters.
    f. Press *ALD Process Start* (OK) button.
    g. Record H_2O pulse/purge times, $TiCl_4$ pulse/purge times, and number of cycles in logbook.
6. Open Test Panel. Click on Digital I/O tab. Change Line Number 5 (H_2O) and 6 ($TiCl_4$) from Input to Output. Do this by clicking on Output checkbox once.
7. Record N_2 pressure values with N_2 flow off and on. Record readings for both Channel 1 (pump) and 2 (process chamber).
8. Pump on H_2O line: Open vacuum toggle valve on H_2O line. Wait for line pressure to reach chamber pressure. Close vacuum toggle valve.
9. Pump on $TiCl_4$ line by repeating procedure from step 8 for the $TiCl_4$ line.
10. Pump on H_2O bottle: Open source bottle valve. Open H_2O vacuum toggle valve. Allow vacuum to pump on source bottle for a few seconds. Close vacuum toggle valve. Close source bottle.

11. Pump on $TiCl_4$ bottle by repeating procedure from step 10 for the $TiCl_4$ source.
12. Test H_2O solenoid valve. Open H_2O source bottle valve. In Test Panel, turn Line Number 5 ON by clicking on Logic checkbox. Watch for pressure change on Channel 2. Turn Line Number 5 OFF.
13. Wait a few seconds before testing $TiCl_4$ solenoid valve. Open $TiCl_4$ source. Turn ON Line Number 6 in Test Panel and watch for pressure change. Turn OFF Line Number 6. Close Test Panel.
14. Make sure scrubber inlet diverting valve is set for gas flow into the scrubber (arrow pointing down). Flip scrubber power switch to ON. Pressure should be ~25 psi. Make a note in the logbook if pressure reading is anomalous.
15. Record Channel 2 pressure readings for H_2O and $TiCl_4$ pulses once the ALD run has started.
16. Record thermocouple temperature.

ALD Run Shutdown

1. When temperature program has ended, prop open furnace top to speed up cooling time.
2. Close both source bottle valves.
3. Allow scrubber and N_2 flow into the vacuum pump to remain on for an hour after the run has ended.
4. When furnace chamber has cooled to ~50^oC, the sample can be removed by following the sample load procedure above.

System Shut Down (for school breaks and major equipment maintenance):

Process Chamber

1. Turn the furnace heat and power off.
2. Close source bottle valves.
3. Close ball valve to vacuum pump.
4. Increase N_2 flow to ~999 sccm to bring process tube Channel 1 pressure to ~750 Torr.
5. At 750 Torr, flip N_2 flow toggle switch to OFF.
6. Close main (process chamber) N_2 valve.

Vacuum Pump

1. Loosen the QF25 clamp just above the pump inlet.
2. Turn the pump off using the front panel toggle switch. This also deenergizes the solenoid valves and the green lamp will turn off.
3. Lift the QF25 tee to vent the inlet of the pump.
4. Close both N_2 MFCs to the pump.
5. Re-clamp the QF25 tee.

6. Close the toggle valve to the ALD N_2 line at the LN_2 dewar, but leave the dewar open so that N_2 flows to the chemical dry box.

Scrubber

1. Flip the scrubber power switch OFF.
2. Turn the scrubber inlet diverting valve to point down – gas flow into the scrubber.

APPENDIX C

CALCULATION OF OPAL SURFACE AREA

The volume of the confinement cell, V_{cell}, as shown in Figure A.C.1 is given by:

$$V_{cell} = 2\,\text{cm} \times 2\,\text{cm} \times 10\,\mu\text{m} = 4 \times 10^{-3}\,\text{cm}^3. \quad \text{(C.1)}$$

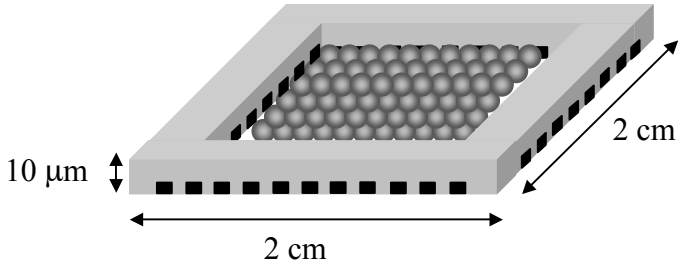

Figure C.1. Schematic of confinement cell with one layer of SiO_2 spheres assembled.

Since the opal forms a close-packed FCC structure, the SiO_2 spheres occupy 74% of the cell volume. Therefore, the opal volume, V_{opal}, can be written as:

$$V_{opal} = 0.74 \cdot Vcell = 0.74(4 \times 10^{-3}\,\text{cm}^3) = 2.96 \times 10^{-3}\,\text{cm}^3. \quad \text{(C.2)}$$

The number of spheres, n, in the opal can be calculated by dividing the opal volume by the volume of a silica sphere (V_{sphere}).

$$n = \frac{V_{opal}}{V_{sphere}} = \frac{2.96 \times 10^{-3}\,\text{cm}^3}{4/3\,\pi r_{sphere}^3} = \frac{2.22 \times 10^{-3}\,\text{cm}^3}{\pi r_{sphere}^3}, \quad \text{(C.3)}$$

where r_{sphere} is the radius of the SiO_2 sphere in cm. Therefore, the surface area of the opal equals the number of spheres multiplied by the surface area of one silica sphere.

$$S = n \cdot 4\pi r_{sphere}^2 = \frac{2.22 \times 10^{-3}\,\mathrm{cm}^3}{\pi r_{sphere}^3} \cdot 4\pi r_{sphere}^2 = \frac{8.88 \times 10^{-3}\,\mathrm{cm}^2}{r_{sphere}}. \qquad \text{(C.4)}$$

But, the radius is one-half of the sphere diameter, $d_{sphere,}$ thus the surface area is equivalent to:

$$S = \frac{4.44 \times 10^{-3}\,\mathrm{cm}^2}{d_{sphere}}. \qquad \text{(C.5)}$$

The size of the SiO_2 spheres used in the fabrication of photonic crystals is on the scale of hundreds of nanometers, therefore the surface area can be rewritten as:

$$S = \frac{4.44 \times 10^{4}\,\mathrm{cm}^2}{d_{sphere}}, \qquad \text{(C.6)}$$

where the unit of d_{sphere} is now in nm.

APPENDIX D

CALCULATION OF MAXIMUM COATING THICKNESS

The maximum coating thickness, t, is the thickness at which the TiO_2 films begin to touch within the octahedral void between the SiO_2 spheres.

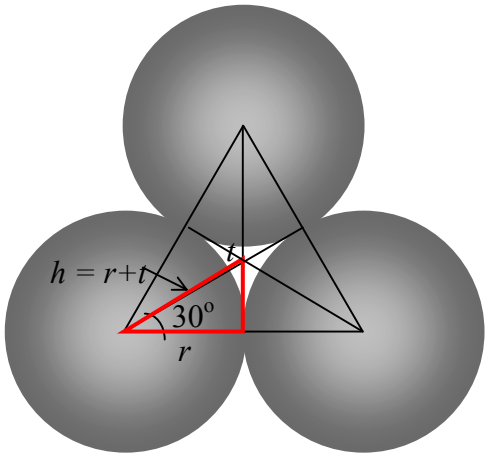

Figure D.1. Schematic of octahedral void between SiO_2 spheres in the (111) plane.

The cosine of the angle indicated in the small red triangle in Figure D.1 can be written as:

$$\cos 30° = \frac{r}{h} = \frac{r}{r+t}, \tag{D.1}$$

where r is the sphere radius and h is the hypotenuse of the right triangle. Solving for the thickness, t, yields the following equation:

$$t = \frac{r}{\cos 30°} - r. \tag{D.2}$$

Therefore, t =15.5% of r, or 7.75% of d since the diameter is double the length of the radius.

APPENDIX E

SUMMARY OF ALD RUNS

Table E.1. Summary of ALD TiO_2 Thin Film and Opal Infiltration Runs

Run	H_2O Pulse Length	H_2O Purge Length	$TiCl_4$ Pulse Length	$TiCl_4$ Purge Length	Flow Rate (sources)	Flow Rate (N_2 purge)	Growth Temp	Number of Cycles	Growth Rate	Thickness
	(ms)	(ms)	(ms)	(ms)	(sccm)	(sccm)	(^oC)		(nm/cycle)	(nm)
0	2000	2000	2000	2000	100		100	1000	0.136	136.3
1	2000	2000	4000	2000	100		100	2000	0.076	151.3
2	2000	2000	4000	2000	100		100	2000	0.075	149.5
									0.087	174.3
3	2000	4000	4000	2000	200		100	2000	0.113	225.2
4	2000	2000	4000	2000	200		200	30	n/a	n/a
									n/a	n/a
5	500	2000	1000	2000	500		200	2000		
6	500	2000	1000	2000	200		200	2000		can't fit
7	500	4000	1000	4000	200		300	2000	0.178	356.6
8	500	4000	1000	4000	200		400	1155	0.042	48.1
9	500	4000	1000	4000	200		400	2000		can't fit
10	500	4000	1000	4000	200		500	2000	0.049	98.4
									0.048	95.88
11	1000	4000	2000	4000	200		500	2000	n/a	n/a
12	1000	4000	2000	4000	500		500	2000	n/a	n/a
13	2000	4000	4000	4000	200		500	2000		
										can't fit
									n/a	n/a
14	2000	2000	4000	2000	100		100	1000		
15	2000	2000	4000	2000	100		200	1000	0.157	156.5

Run	H_2O Pulse Length	H_2O Purge Length	$TiCl_4$ Pulse Length	$TiCl_4$ Purge Length	Flow Rate (sources)	Flow Rate (N_2 purge)	Growth Temp	Number of Cycles	Growth Rate	Thickness
	(ms)	(ms)	(ms)	(ms)	(sccm)	(sccm)	(^oC)		(nm/cycle)	(nm)
16	2000	4000	4000	4000	100		300	2000		can't fit
17	2000	2000	4000	2000	100		100	1000	0.446	445.5
18	2000	4000	4000	4000	50		300	2000	n/a	n/a
	2000	4000	4000	4000	50		300	2000		can't fit
19	1000	4000	2000	4000	100		400	2000	0.059	117.2
20	500	2000	1000	2000	200		200	1250		can't fit
21	500	2000	1000	2000	100		200	2000		can't fit
										can't fit
22	500	4000	1000	4000	200		500	2000	n/a	n/a
									n/a	n/a
23	500	2000	1000	2000	200		200	1000		can't fit
										can't fit
24	500	2000	1000	2000	200		500	2000		can't fit
25	500	4000	1000	4000	200		100	2000		
26	500	2000	1000	2000	200		100	2000	0.392	784.2

Run	H_2O Pulse Length	H_2O Purge Length	$TiCl_4$ Pulse Length	$TiCl_4$ Purge Length	Flow Rate (sources)	Flow Rate (N_2 purge)	Growth Temp	Number of Cycles	Growth Rate	Thickness
	(ms)	(ms)	(ms)	(ms)	(sccm)	(sccm)	(^oC)		(nm/cycle)	(nm)
									0.339	677.7
27	500	2000	1000	2000	200		300	2000	0.109	218
									0.089	178.3
									0.070	139.2
28	500	2000	1000	2000	200		400	2000	0.048	95.8
29	500	2000	1000	2000	200		500	100	n/a	n/a
									n/a	n/a
30	500	4000	1000	4000	200		100	2000	0.154	308.1
									0.130	259.4
31	500	4000	1000	4000	200		200	2000		can't fit
32	500	4000	1000	4000	200		300	1000	0.057	56.93
33	500	4000	1000	4000	200		400	1000	0.052	51.99
34	500	4000	1000	4000	200		500	1000	0.043	42.52
35	500	4000	1000	4000	200		200	1000	0.059	58.97
36	500	4000	1000	4000	200		200	1000	0.575	574.6
37	250	4000	500	4000	200		200	1000		can't fit
38	500	4000	1000	4000	200		200	1000	0.043	43.37
39	500	8000	1000	8000	200		300	2000	n/a	n/a
									n/a	n/a
									n/a	n/a
40	500	8000	1000	8000	200		300	2000		can't fit
										can't fit
									0.067	134.4
41	500	6000	1000	6000	200		300	2000	0.025	50.1
42	500	4000	1000	4000	200		300	2000	0.026	51.95
43	500	2000	1000	2000	200		300	2000	n/a	n/a
44	500	10000	1000	10000	200		300	2000	0.053	105.1
									0.052	104.2

Run	H_2O Pulse Length	H_2O Purge Length	$TiCl_4$ Pulse Length	$TiCl_4$ Purge Length	Flow Rate (sources)	Flow Rate (N_2 purge)	Growth Temp	Number of Cycles	Growth Rate	Thickness
	(ms)	(ms)	(ms)	(ms)	(sccm)	(sccm)	(^oC)		(nm/cycle)	(nm)
45	1000	6000	2000	6000	200		300	2000	0.058	115.2
46	500	4000	1000	4000	200		100	1000	0.147	147.3
47	500	7000	1000	7000	200		300	2000	0.053	106.0
48	1500	6000	3000	6000	200		300	2000	0.062	123.4
49	2000	6000	4000	6000	200		300	2000	0.067	133.7
50	250	6000	500	6000	200		300	2000	0.055	109.7
51	1000	4000	2000	4000	200		300	2000	0.059	117.5
52	1000	2000	2000	2000	200		300	2000	0.058	115.6
53	500	6000	1000	6000	200		300	2000	0.054	107.6
54	125	6000	250	6000	200		300	2000	0.055	109.1
55	100	6000	200	6000	200		300	2000	0.056	111.7
56	75	6000	150	6000	200		300	2000	0.056	112.2
57	100	2000	200	2000	200		500	4000	0.043	172.7
58	100	2000	200	2000	200		600	4000	0.043	173.7
59	100	2000	200	2000	200		400	4000	0.050	200.1
60	500	4000	1000	4000	200		300	2000	0.054	107.7
61	100	2000	200	2000	200		700	4000		can't fit
62	250	4000	500	4000	200		600	2000		can't fit
									0.000	
										can't fit
63	250	2000	500	2000	200		500	2000	0.048	96.79
									0.000	
64	250	2000	500	2000	200		400	2000	0.051	102.3
									0.000	
65	500	4000	1000	4000	200		150	1000	0.111	110.7
66	500	4000	1000	4000	200		600	1000	n/a	n/a
66B	500	4000	1000	4000	200		600	2000	0.021	41.01
								1000	n/a	n/a

Run	H_2O Pulse Length	H_2O Purge Length	$TiCl_4$ Pulse Length	$TiCl_4$ Purge Length	Flow Rate (sources)	Flow Rate (N_2 purge)	Growth Temp	Number of Cycles	Growth Rate	Thickness
	(ms)	(ms)	(ms)	(ms)	(sccm)	(sccm)	(^oC)		(nm/cycle)	(nm)
67	2000	2000	2000	2000	200		100	286	0.197	56.3
68	100	2000	200	2000	200		600	3000	0.043	128.1
69	500	8000	1000	8000	200		300	2000	0.056	112.3
70	200	2000	400	2000	200		600	3000	0.042	126.5
71	1000	8000	2000	8000	200		300	2000	0.058	116.0
72	150	2000	300	2000	200		600	3000	0.042	125.7
73	500	2000	1000	2000	200		300	2000	0.057	113.5
74	500	8000	1000	8000	200		300	2000	0.057	113.4
75	400	2000	800	2000	200		600	3000	0.000	
76	300	2000	600	2000	200		600	3000	0.000	
77	100	2000	200	2000	200		700	3000	n/a	n/a
									0.000	
78	100	2000	200	2000	200		200	1000	0.180	179.9
79	100	2000	200	2000	200		350	2000	0.051	102.2
80	100	2000	200	2000	200		500	2000	0.039	78.76
									0.000	
81	250	2000	500	2000	200		600	3000	0.042	126.9
82	250	2000	500	2000	200		300	2000	0.049	97.03
									0.043	85.0
83	250	2000	500	2000	200		600	2000	0.033	66.43
									0.030	59.08

Run	H_2O Pulse Length	H_2O Purge Length	$TiCl_4$ Pulse Length	$TiCl_4$ Purge Length	Flow Rate (sources)	Flow Rate (N_2 purge)	Growth Temp	Number of Cycles	Growth Rate	Thickness
	(ms)	(ms)	(ms)	(ms)	(sccm)	(sccm)	(^oC)		(nm/cycle)	(nm)
84	250	2000	500	2000	200		200	2000	0.033	65.97
									0.027	54.5
85	250	2000	500	2000	200		700	2000	0.022	43.89
									0.000	
86	250	2000	500	2000	200		100	2000	0.083	165.0
									0.000	
87	250	2000	500	2000	200		200	2000	0.124	248.3
									0.000	
88	250	2000	500	2000	200		150	2000	0.067	133.7
									0.000	
89	250	2000	500	2000	200		175	2000	0.048	96.34
90	250	2000	500	2000	200		225	2000	0.096	192.6
91	400	2000	800	2000	200		600	3000	0.045	134.7
92	250	2000	500	2000	200		150	2000	0.091	182.0
									0.000	
93	250	2000	500	2000	200		150	2000	0.096	191.2
94	500	2000	1000	2000	200		600	3000	0.042	124.8
95	500	4000	1000	4000	200		150	1000	0.076	75.72
96	1000	2000	2000	2000	200		600	3000	0.041	122.4

Run	H_2O Pulse Length	H_2O Purge Length	$TiCl_4$ Pulse Length	$TiCl_4$ Purge Length	Flow Rate (sources)	Flow Rate (N_2 purge)	Growth Temp	Number of Cycles	Growth Rate	Thickness
	(ms)	(ms)	(ms)	(ms)	(sccm)	(sccm)	(^oC)		(nm/cycle)	(nm)
97	1500	4000	3000	4000	200		100	1000	0.305	305.1
98	2000	4000	4000	4000	200		100	1000	0.379	378.6
99	1500	2000	3000	2000	200		600	109	n/a	n/a
100	2000	8000	4000	8000	200		100	500	0.184	91.86
101	1500	8000	3000	8000	200		100	500	0.122	61.21
102	500	2000	1000	2000	200	25	300	2000	0.053	105.9
103	250	2000	500	2000	200	25	100	2000	0.141	282.0
104	250	2000	500	2000	200	25	100	2000	0.124	247.4
105	250	2000	500	2000	200	25	100	2000	0.099	198.6
106	250	2000	500	2000	200	10	100	2000	0.100	199.5
107	250	2000	500	2000	200	10	100	2000	0.095	189.3
108	250	2000	500	2000	200	25	100	2000	0.084	167.9
109	250	2000	500	2000	200	25	100	2000	0.088	175.3
110	2000	10000	4000	10000	200	25	100	1000	0.095	95.12
111	1500	10000	3000	10000	200	25	100	1000	0.093	92.86
112	3000	10000	6000	10000	200	25	100	1000	0.094	94.45
113	500	10000	1000	10000	200	25	100	1000	0.072	72.16
114	4000	10000	8000	10000	200	25	100	1000	0.112	111.7
115	3500	10000	7000	10000	200	25	100	1000	0.104	104.4
116	1000	10000	2000	10000	200	25	100	1000	0.098	98.02
117	2000	8000	4000	8000	200	25	100	1000	0.112	111.6
118	2000	4000	4000	4000	200	25	100	1000	0.118	118.4
119	2000	6000	4000	6000	200	25	100	1000	0.080	79.67
120	2000	10000	4000	10000	200	0	100	1000	0.074	73.77

Run	H_2O Pulse Length	H_2O Purge Length	$TiCl_4$ Pulse Length	$TiCl_4$ Purge Length	Flow Rate (sources)	Flow Rate (N_2 purge)	Growth Temp	Number of Cycles	Growth Rate	Thickness
	(ms)	(ms)	(ms)	(ms)	(sccm)	(sccm)	(^oC)		(nm/cycle)	(nm)
121	2000	6000	4000	6000	200	0	100	1000	0.078	78.44
122	1000	10000	2000	10000	200	25	100	1000	0.076	76.09
123	250	10000	500	10000	200	25	100	1000	0.059	58.85
124	250	2000	500	2000	200	25	600	3000	0.042	126.1
O1	1500	10000	3000	10000	200	25	100	107	0.000	
O2	3000	10000	6000	10000	200	25	100	107	0.000	
O3	4000	16000	8000	16000	200	25	100	107	0.000	
O4	500	10000	1000	10000	200	25	94	220	0.000	
O5	2000	10000	4000	10000	200	25	94	220	0.000	
O6	3000	10000	6000	10000	200	25	94	220	0.000	
O7	4000	16000	8000	16000	200	25	94	220	0.000	
O8	1500	10000	3000	10000	200	25	94	220	0.000	
O9	5000	20000	10000	20000	200	25	94	220	0.000	
O10	2000	2000	2000	2000	200	25	94	220	0.000	
O11	6000	10000	6000	10000	200	25	94	220	0.000	
O12	8000	16000	8000	16000	200	25	94	220	0.000	
O13	10000	20000	10000	20000	200	25	94	220	0.000	
125	500	2000	1000	2000	200	25	300	6000	0.000	
O14	4000	20000	8000	20000	200	25	94	220	0.000	
O15	4000	24000	8000	24000	200	25	94	220	0.000	
O16	4000	28000	8000	28000	200	25	94	220	0.000	
O17	4000	32000	8000	32000	200	25	94	220	0.000	
O18	500	500	500	500	200	25	94	220	0.000	
O19	4000	36000	8000	36000	200	25	94	220	0.000	
O20	2000	2000	2000	2000	200	0	94	220	0.000	
O21	500	10000	1000	10000	200	25	300	368	0.000	

REFERENCES

1. J.D. Joannopoulos, R.D. Meade, and J.N. Winn. Photonic crystals: Molding the flow of light. Princeton University Press (1995).

2. J.D. Joannopoulos, P. R. Villeneuve, and S. Fan. Photonic crystals: putting a new twist on light. *Nature* **386**, 143-149 (1997).

3. E. Yablonovitch. Inhibited spontaneous emission in solid-state physics and electronics. *Phys. Rev. Lett.* **58,** 20, 2059-2062 (1987).

4. S. John. Strong localization of photons in certain disordered dielectric superlattices. *Phys. Rev. Lett.* **58**, 23, 2486-2489 (1987).

5. C. M. Soukoulis. Photonic crystals and light localization in the 21st century. Kluwer Academic Publishers (2001).

6. M. Fox. Optical properties of solids. Oxford University Press (2001).

7. K. M. Ho, C. T. Chan, and C. M. Soukoulis. Existence of a photonic band gap in periodic dielectric structures. *Phys. Rev. Lett.* **65**, 25, 3152- (1990).

8. E. Yablonovitch and T. J. Gmitter. Photonic band structure: the face-centered-cubic case. *Phys. Rev. Lett.* **63**, 18, 1950-1953 (1989).

9. H. S. Sozuer, J. W. Haus, and R. Inguva. Photonic bands: convergence problems with the plane-wave method. *Phys. Rev. B* **45**, 24, 13962-13972 (1992).

10. S. John and K. Busch. Photonic bandgap formation and tunability in certain self-organizing systems. *J. Lightwave Tech.* **17**, 11, 1931-1943 (1999).

11. S. Adachi. Optical dispersion relations for GaP, GaAs, GaSb, InP, InAs, InSb, $Al_xGa_{1-x}As$, and $In_{1-x}Ga_xAs_yP_{1-y}$. *J. Appl. Phys.* **66**, 12, 6030-6040 (1989).

12. M. Mueller, R. Zentel, T. Maka, S. G. Romanov, and C. M. S. Torres. Photonic crystal films with high refractive index contrast. *Adv. Mater.* **12**, 20, 1499-1503 (2000).

13. S. Tanemura, L. Miao, P. Jin, K. Kaneko, A. Terai, and N. Nabatova-Gabain. Optical properties of polycrystalline and epitaxial anatase and rutile TiO2 thin films by rf magnetron sputtering. *Appl. Surf. Sci.* **212-213**, 654-660 (2003).

14. E. D. Palik. Handbook of optical constants. Academic Press (1998).

15. J. M. Bennett, E. Pelletier, G. Albrand, J. P. Borgogno, B. Lazarides, C. K. Carniglia, R. A. Schmell, T. H. Allen, T. Tuttle-Hart, K. H. Guenther, and A. Saxer. Comparison of the properties of titanium dioxide films prepared by various techniques. *Appl. Optics* **28**, 15, 3303-3317(1989).

16. http://ruby.colorado.edu/~smyth/min/tio2.html

17. C. J. Howard, T. M. Sabine, and F. Dickson. *Acta Cryst.* **B47**, 462-468 (1991).

18. E. P. Meagher and A. L. George. *Canad. Mineral.* **17**, 77-85 (1979).

19. J. D. DeLoach, G. Scarel, and C. R. Aita. Correlation between titania film structure and near ultraviolet optical absorption. *J. Appl. Phys.* **85**, 4, 2377-2384 (1999).

20. E. Yablonovitch, T. J. Gmitter, and K. M. Leung. Photonic band structure: the face-centered-cubic case employing nonspherical atoms. *Phys. Rev. Lett.* **67**, 17, 2295-2298 (1991).

21. E. Yablonovitch. Photonic crystals: semiconductors of light. *Sci. Amer.* December 2001, 47-55 (2001).

22. A. Chelnokov, K. Wang, S. Rowson, P. Garoche, and J. –M. Lourtioz. Near-infrared Yablonovite-like photonic crystals by focused ion beam etching of macroporous silicon. *Appl. Phys. Lett.* **77**, 19, 2943-2945 (2000).

23. R. Hillebrand, St. Senz, W. Hergert, and U. Gosele. Macroporous-silicon-based three-dimensional photonic crystal with a large complete band gap. *J. Appl. Phys.* **94**, 4, 2758-2760 (2003).

24. C. Cuisin, Y. Chen, D. Decanini, F. Carcenac, A. Madouri, J. M. Lourtioz, and H. Launois. Fabrication of three-dimensional microstructures by high resolution x-ray lithography. *J. Vac. Sci. Technol. B* **17**, 6, 3444-3448 (1999).

25. C. Cuisin, A. Chelnokov, J. M. Lourtioz, D. Decanini, and Y. Chen. Submicrometer resolution Yablonovite templates fabricated by x-ray lithography. *Appl. Phys. Lett.* **77**, 6, 770-772 (2000).

26. M. Campbell, D. N. Sharp, M. T. Harrison, R. G. Denning, and A. J. Turberfield. Fabrication of photonic crystals for the visible spectrum by holographic lithography. *Nature* **404**, 53-56 (2000).

27. E. Ozbay, E. Michel, G. Tuttle, R. Biswas, M. Sigalas, and K. M. Ho. Micormachined millimeter-wave photonic band-gap crystals. *Appl. Phys. Lett.* **64**, 16, 2059-2061 (1994).

28. S. Y. Lin, J. G. Fleming, D. L. Hetherington, B. K. Smith, R. Biswas, K.M. Ho, M. M. Sigalas, W. Zubrzycki, S. R. Kurtz, and J. Bur. A three-dimensional optical photonic crystal operating at infrared wavelengths. *Nature* **394**, 251-253 (1998).

29. S. Y. Lin and J. G. Fleming. A three-dimensional optical photonic crystal. *J. Lightwave Tech.* **17**, 11, 1944-1947 (1999).

30. S. Fan, P. R. Villeneuve, R. D. Meade, and J. D. Joannopoulos. Design of three-dimensional photonic crystals at submicron lengthscales. *Appl. Phys. Lett.* **65**, 11, 1466-1468 (1994).

31. S. H. Park and Y. Xia. Assembly of mesoscale particles over large areas and its application in fabricating tunable optical filters. *Langmuir* **15**, 266-273 (1999).

32. Y. Xia, B. Gates, Y. Yin, and Y. Lu. Monodispersed colloidal spheres: old materials with new applications. *Adv. Mater.* **12**, 10, 693-713 (2000).

33. H. S. Sozuer and J. P. Dowling. Photonic band calculations for woodpile structures. *J. Mod. Opt.* **41**, 231-239 (1994).

34. J. G. Fleming, S. Y. Lin, I. El-Kady, R. Biswas, and K.M. Ho. A three-dimensional optical photonic crystal operating at infrared wavelengths. *Nature* **417**, 52-55 (2002).

35. A. Blanco, E. Chomski, S. Grabtchak, M. Ibisate, S. John, S. W. Leonard, C. Lopez, F. Meseguer, H. Miguez, J. P. Mondia, G. A. Ozin, O. Toader, and H. M. van Driel. Large-scale synthesis of a silicon photonic crystal with a complete three-dimensional bandgap near 1.5 micrometres. *Nature* **405**, 437-440 (2000).

36. Y. A. Vlasov, X.-Z. Bo, J. C. Sturm, and D. J. Norris. On-chip natural assembly of silicon photonic bandgap crystals. *Nature* **414**, 289-293 (2001).

37. J. Wijnhoven and W. L. Vos. Prepartion of photonic crystals made of air spheres in titania. *Science* **281**, 802-804 (1998).

38. W. L. Vos and H. M. van Driel. Higher order Bragg diffraction by strongly photonic fcc crystals: onset of a photonic bandgap. *Phys. Lett. A* **272**, 101-106 (2000).

39. J. E. G. J. Wijnhoven, L. Bechger, and W. L. Vos. Fabrication and characterization of large macroporous photonic crystals in titania. *Chem. Mater.* **13**, 4486-4499 (2001).

40. A. Richel, N. P. Johnson, and D. W. McComb. Observation of Bragg reflection in photonic crystals synthesized from air spheres in a titania matrix. *Appl. Phys. Lett.* **76**, 14, 1816-1818 (2000).

41. W. Dong, H. J. Bongard, and F. Marlow. New type of inverse opals: titania with skeleton structure. *Chem. Mater.* **15**, 568-574 (2003).

42. W. Dong and F. Marlow. Photonic crystals with skeleton structure. *Phys. E* **17**, 431-432 (2003).

43. R. C. Schroden, M. Al-Daous, C. F. Blanford, and A. Stein. Optical properties of inverse opal photonic crystals. *Chem. Mater.* **14**, 3305-3315 (2002).

44. J. S. King, C. W. Neff, C. J. Summers, W. Park, S. Blomquist, E. Forsythe, and D. Morton. High-filling-fraction inverted ZnS opals fabricated by atomic layer deposition. *Appl. Phys. Lett.* **83**, 13, 2566-2568 (2003).

45. G. Subramania, K. Constant, R. Biswas, M. M. Sigalas, and K. M. Ho. Optical photonic crystals fabricated from colloidal systems. *Appl. Phys. Lett.* **74**, 26, 3933-3935 (1999).

46. G. Subramania, R. Biswas, K. Constant, M. M. Sigalas, and K. M. Ho. Structural characterization of thin film photonic crystals. *Phys. Rev. B* **63**, 2351111-235117 (2001).

47. G. Subramanian, V. N. Manoharan, J. D. Thorne, and D. J. Pine. Ordered macroporous materials by colloidal assembly: a possible route to photonic bandgap materials. *Adv. Mater.* **11**, 15, 1261-1265 (1999).

48. T. Suntola and M. Simpson. Atomic layer epitaxy. Chapman and Hall (1990).

49. M. Ritala and M. Leskela in: H.S. Nalwa (Ed.). Handbook of thin film materials, vol. 1. Academic Press (2002).

50. M. Leskela and M. Ritala. Review, Atomic layer deposition (ALD): from precursors to thin film structures. *Thin Solid Films* **409**, 138-146 (2002).

51. M. Ritala, M. Leskela, E. Nykanen, P. Soininen, and L. Niinisto. Growth of titanium dioxide thin films by atomic layer epitaxy. *Thin Solid Films* **225**, 288-295 (1993).

52. J. Aarik, A. Aidla, T. Uustare, and V. Sammelselg. Morphology and structure of TiO_2 thin films grown by atomic layer deposition. *J. Crystal Growth* **148**, 268 (1995).

53. J. Aarik, A. Aidla, A.-A. Kiisler, T. Uustare, and V. Sammelselg. Effect of crystal structure on optical properties of TiO_2 films grown by atomic layer deposition. *Thin Solid Films* **305**, 270-273 (1997).

54. J. Aarik, A. Aidla, H. Mandar, and T. Uustare. Atomic layer deposition of titanium dioxide from $TiCl_4$ and H_2O: investigation of growth mechanism. *Appl. Surf. Sci.* **172**, 148-158 (2001).

55. J. Aarik, A. Aidla, V. Sammelselg, H. Siimon, and T. Uustare. Control of thin film structure by reactant pressure in atomic layer deposition of TiO_2. *J. Crystal Growth* **169**, 496-502 (1996).

56. J. Aarik, A. Aidla, V. Sammelselg, and T. Uustare. Effect of growth conditions on formation of TiO_2-II thin films in atomic layer deposition process. *J. Crystal Growth* **181**, 259-264 (1997).

57. M. H. Suhail, G. M. Rao, and S. Mohan. DC reactive magnetron sputtering of titanium - structural and optical characterization of TiO_2 films. *J. Appl. Phys.* **71**, 3, 1421-1427 (1992).

58. N. Martin, C. Rousselot, D. Rondot, F. Plamino, and R. Mercier. Microstructure modification of amorphous titanium oxide thin films during annealing treatment. *Thin Solid Films* **300**, 113-121 (1997).

59. D. Mardare and G.I. Rusu. The influence of heat treatment on the optical properties of titanium oxide thin films. *Materials Letters* **56**, 210-214, (2002).

60. V. Mikhelashvili and G. Eisenstein. Effect of annealing conditions on optical and electrical characteristics of titanium dioxide films deposited by electron beam evaporation. *J. Appl. Phys.* **89**, 6, 3256-3269 (2001).

61. X. H. Xu, M. Wang, Y. Hou, S. R. Zhao, H. Wang, D. Wang, and S. X. Shang. Effect of thermal annealing on structural properties, morphologies and electrical properties of TiO_2 thin films grown by MOCVD. *Cryst. Res. Technol.* **37**, 5, 431-439 (2002).

62. M. M. Rahman, G. Yu, T. Soga, T. Jimbo, H. Ebisu, and M. Umeno. Refractive index and degree of inhomogeneity of nanocrystalline TiO_2 thin films: effects of substrate and annealing temperature. *J. Appl. Phys.* **88**, 8, 4634-4641 (2000).

63. R. A. Spurr and H. Myers. Quantitative analysis of anatase-rutile mixtures with an x-ray diffractometer. *Analyt. Chem.* **29**, 760-762 (1957).

64. W. Stober, A. Fink, and E. Bohn. Controlled growth of monodispersed silica spheres in the micron size range. *J. Coll. Interface Sci.* **26**, 62-69 (1968).

65. D. Poelman and P. Smet. Methods for the determination of the optical constants of thin films from single transmission measurements: a critical review. *J. Phys. D: Appl. Phys.* **36**, 1850-1857 (2003).

66. R. Swanepoel. Determination of the thickness and optical constants of amorphous silicon. *J. Phys. E: Sci. Instrum.* **16**, 1214-1222 (1983).

67. M. Allard, E. H. Sargent, E. Kumacheva, and O. Kalinina. Characterization of internal order of colloidal crystals by optical diffraction. *Optical and Quantum Electronics* **34**, 27-36 (2002).

68. NIST XPS database: http://srdata.nist.gov/xps/

69. J. King *et al.* To be published.

70. A. Imhof and D. J. Pine. Ordered macroporous materials by emulsion templating. *Nature* **389**, 948-951 (1997).

71. K. Busch and S. John. Liquid-crystal photonic-band-gap materials: the tunable electromagnetic vacuum. *Phys. Rev. Lett*. **83**, 5, 967-970 (1999).

72. K. Yoshino, Y. Shimoda, Y. Kawagishi, K. Nakayama, and M. Ozaki. Temperature tuning of the stop band in transmission spectra of liquid-crystal infiltrated synthetic opal as tunable photonic crystal. *Appl. Phys. Lett.* **75**, 7, 932-934 (1999).

73. S.W. Leonard, J.P. Mondia, H.M. van Driel, O. Toader, S. John, K. Busch, A. Birner, U. Gosele, and V. Lehmann. Tunable two-dimensional photonic crystals using liquid-crystal infiltration. *Phys. Rev. B* **61**, 4, R2389-R2392 (2000).

74. Q.B. Meng, C.H. Fu, S. Hayami, Z.Z. Gu, O. Sato, and A. Fujishima. Effects of external electric field upon the photonic band structure in synthetic opal infiltrated with liquid crystal. *J. Appl. Phys.* **89**, 10, 5794-5796 (2001).

75. Y. Shimoda, M. Ozaki, and K. Yoshino. Electric field tuning of a stop band in reflection spectrum of synthetic opal infiltrated with nematic liquid crystal. *Appl. Phys. Lett.* **79**, 22, 3627-3629 (2001).

76. G. Mertens, T. Roder, R. Schweins, K. Huber, and H. Kitzerow. Shift of the photonic band gap in two photonic crystal/liquid crystal composites. *Appl. Phys. Lett.* **80**, 11, 1885-1887 (2002).

77. H. Takeda and K. Yoshino. Tunable photonic band schemes of opals and inverse opals infiltrated with liquid crystals. *J. Appl. Phys.* **92**, 10, 5658-5662 (2002).

78. S. Gottardo, D. S. Wiersma, and W. L. Vos. Liquid crystal infiltration of complex dielectrics. *Physica B* **338**, 143-148 (2003).

79. R.J. Guo, M.H. Wang, T.L. Tso, and T.P. Perng. Photoelectrochemical properties of sulfidized TiO_2 electrodes. *Int. J. Hydrogen Energy* **20**, 7, 561-566 (1995).

80. M.A. Sriram and P.N. Kumta. New molecular routes for synthesizing titanium disulfide. *Mat. Sci. Eng.* **B33**, 140-147 (1995).

81. J. Rodriguez, J. Hrbek, J. Dvorak, T. Jirsak, and A. Maiti. Interaction of sulfur with TiO_2 (110): photoemission and density- functional studies. *Chem. Phys. Lett.* **336**, 377-384 (2001).

82. Y. Kavanagh and D.C. Cameron. Zinc sulfide thin films produced by sulfidation of sol-gel deposited zinc oxide. *Thin Solid Films* **398-399**, 24-28 (2001).